Investigation of Portland Cement Concrete Hydration Behavior at Its Early Age Using Embedded Fiber Optic Temperature Sensors

BY

ALICE CHAO
Bachelor of Science, University of Massachusetts Lowell

SUBMITTED IN PARTIAL FULFILLMENT OF THE REQUIREMENTS
FOR THE DEGREE OF MASTER OF SCIENCE
DEPARTMENT OF CIVIL AND ENVIRONMENTAL ENGINEERING
UNIVERSITY OF MASSACHUSETTS LOWELL

Signature of the Author .....
Department of Civil and Environmental Engineering
(November 16), 2011

Signature of Thesis Supervisor .....
Professor Tzu-Yang Yu
Department of Civil and Environmental Engineering

Committee Member Signature .....
Professor Donald Leitch
Department of Civil and Environmental Engineering

Committee Member Signature .....
Professor Susan Faraji
Department of Civil and Environmental Engineering

Committee Member Signature .....
Professor Xingwei Wang
Department of Electrical and Computer Engineering

Investigation of Portland Cement Concrete Hydration Behavior at Its Early Age Using Embedded Fiber Optic Temperature Sensors

BY

ALICE CHAO
Bachelor of Science, University of Massachusetts Lowell

ABSTRACT OF A THESIS SUBMITTED TO THE FACULTY OF THE
DEPARTMENT OF CIVIL AND ENVIRONMENTAL ENGINEERING
IN PARTIAL FULFILLMENT OF THE REQUIREMENTS
FOR THE DEGREE OF
MASTER OF SCIENCE
UNIVERSITY OF MASSACHUSETTS LOWELL
2011

Thesis Supervisor: Professor Tzu-Yang Yu
Title: Department of Civil and Environmental Engineering

Abstract

Concrete is known as a heterogeneous material made of complex chemical compositions. The development of concrete temperature during early age is crucial on its long term durability. Cracking can occur, if the concrete temperature rise too high or if there is large temperature difference between interior and exterior of concrete during early hydration stages. This premature failure can lead to undesired results which may associate with quality concern, time consuming and extra cost. In this research, the effect of ambient temperature and adiabatic temperature are considered during the temperature measurement within concrete cylinders at early age; the first 45 hours and the first 70 hours. Concrete specimens were manufactured under various water-to-cement ratios (w/c) (0.40, 0.45, 0.50, 0.55 and 0.60). A Fabry-Perot (FP) fiber optic temperature sensor and type K thermocouple sensor were embedded into concrete cylinders to monitor the temperature development during early-age hydration in the first experiment. Two FP sensors were inserted in the second experiment. Each concrete cylinder was insulated in styrofoam chamber. A sampling rate of 20 second was used in all experiments. From the experimental result, it is found that FP fiber optic temperature sensors are reliable. Temperature profiles are used for calculating the apparent activation energy (E_a) and the heat of hydration (H(t)) of concrete, which can help us to better understand cement hydration.

Acknowledgements

I would like to express my most sincere thanks and appreciation to my Master's thesis research advisor Dr. Tzu-Yang Yu. Dr. Yu provided me an invaluable opportunity to conduct this thesis research. He has always been my most supportive person in overcoming difficulties during the course of my study.

I would like to offer special thanks to Prof. Donald Leitch for his guidance in the concrete mix design. I also would like to offer my appreciation toward my thesis committee members Dr. Susan Faraji, Prof. Donald Leitch and Dr. Xingwei Wang for their valuable comments and inputs.

Many thanks to Prof. Xingwei Wang from Electrical and Computer Engineering Department in offering me the opportunity to collaborate with her PhD student, Xiaotian Zou, and offering me the facility for performing my experiments. Xiaotian has always been a very helpful partner. Xiaotian designed and fabricated fiber optic sensors used in my concrete experimental study.

Finally, I would like to thanks my family members and friends who always support and encourage me until the completion of my Master's thesis.

Contents

List of Figures

List of Tables

Chapter 1

Introduction

1.1 Background of Concrete Temperature Development

During the course of concrete hydration, the distribution of temperature in concrete is usually non-uniform, due to different boundary conditions in concrete structures. Core temperature tends to be higher than surface temperature. If there is excessive heat generated within concrete structure, significant temperature difference can lead to cracking (such as plastic or shrinkage cracking), resulting in the premature failure of concrete. In addition, concrete will not be able to achieve its maximum strength, as it should. Development of plastic shrinkage and thermal cracking are briefly explained as follows:

- Plastic Shrinkage cracking [2]: (a) When ambient temperature increases, water starts evaporating, then the concrete surface starts drying if the evaporation rate is higher than the bleeding rate. As a result, drying shrinkage will occur; (b) Concrete in plastic stage cannot confront with the development of shrinkage stresses,

cracks start propagating ”until the shrinkage stresses are relieved.”

- Thermal cracking [2, 19, 16]: (a) Temperature within concrete structure rises when hydration heat occurs. As a result, concrete will experience thermal expansion and contraction during day time and night time, respectively; (b) Large thermal gradient or temperature difference within concrete specimen can cause cracking.

Generally, the heat within thin concrete members can easily be dissipated into environment. On the other hand, massive concrete structures such as dams, floor slabs, bridge decks, columns and footings are highly vulnerable due to rapid heat development within the structures and slow rate of heat dissipation. Key factors that contribute to the temperature rising rate, peak temperature and temperature gradients include: (a) the rate of hydration heat, (b) the total amount of heat generated, (c) cement content, chemical compositions, cement fineness, mix design, (d) element dimensions, (e) surrounding conditions (wind, radiation, humidity, temperature), (f) concrete placement temperature and (g) types of aggregates [19, 10].

In civil engineering, early age concrete temperature plays a crucial role in determining the long-term performance of concrete structures. The knowledge of the maximum temperature and temperature difference in concrete structures during early age is very important. Usually, allowable maximum temperature and temperature difference are specified to ensure the quality of concrete prior to and after concrete placement. For example, the concrete temperature at delivery shall be limited to a range between 5^oC to $35\ ^oC$ [2]. The maximum temperature within a concrete specimen should not exceed

70^oC during concreting to prevent the delay of ettringite formation. Also, concrete cooling rate should be limited to $3^oC/hr$ during early age (the first 24 hours after concrete placement) [17]. In addition, the temperature difference between the core and surface of concrete should not greater than 20 ^oC in order to avoid thermal cracking [19].

To understand concrete temperature development, numerous researchers performed isothermal, adiabatic and semi-adiabatic tests on concrete. Isothermal tests are widely adopted in measuring heat generation in cement pastes under a constant ambient temperature. Adiabatic calorimetry tests are used for measuring temperature progress of concrete specimens without having any heat dissipation to or absorption from the environment. Semi-adiabatic calorimetry methods allow limited heat exchange with external environment [10].

Some researchers adopted numerical simulation techniques to predict temperature development and heat generation in concrete hydration. The widely used simulation programs are CEMHYD3D, HYMOSTRUC, HIPERPAV and Concrete Works. However, certain assumptions are required (e.g., boundary conditions).

1.2 Background of Fiber Optic Sensors

Civil infrastructure has been considered as a great asset to any country, particularly in Europe and North America. For example, it contributes approximately 1/3 of the U.S economy. In addition, many bridges, highways, and/or railways that are in service have been built years ago. Aging, environmental challenges, daily usage with increasing

number of population can result in structural deterioration [8]. Structural deficiencies can cause many unforeseen public security risks such as the I-35W bridge collapse in Minneapolis which killed 13 people in 2007 [8]. Currently, the repair cost has been mainly invested on rehabilitation, maintenance, and life extension but a few in existing structure replacement and new constructions [7]. Structural health monitoring systems using fiber optic sensors technologies can be considered as a powerful civil infrastructure management tool [7].

Fiber optic sensors technologies are attractive to both academia and industry. They are widely known due to their significant advantages. Compared to conventional sensors, they are electromagnetic immune, low cost, better quality and reliability, high accuracy, multiplexing simplicity and well-suited with embedding in a range of structural materials [30, 3]. However, fiber optic sensors are fragile and can be easily damaged if not protected properly [22].

Fiber optics are made of polymer, glass or ceramic materials, which typically consist of core (which dimension is based on design wavelength) and cladding (which consists of an outer diameter over 100 microns) regions [14]. The core index is usually a little larger than the cladding index. Fiber optic sensors can be classified as follows:

- ”Transduction mechanism: intensity, interferometric, polarimetric, spectrometric” [22],
- Applications: strain, temperature, displacement, acceleration, force, velocity, pH, gas analysis, humidity, Bio-medical and etc [30],
- Extrinsically and intrinsically mounted to sensing regions [22],

- Sensing method: regional, distributed, and multiplexed [22].

Interferometric fiber optic sensors are most applicable for temperature, pressure, strain and vibration measurements. The basic principal of interferometer optical fibers is the same for all types of fiber optic sensors [14]. It should be noticed that the cavity of intrinsic interferometric sensors is a segment along the fiber, while it is an air gap for extrinsic interferometeric sensors [14].

Phase modulation fiber optic sensors evaluate the variations of phase angle of light that travel through sensing fiber and a reference fiber (in an interferometer) [4].

Intensity modulation fiber optic sensors are one of the simplest type of fiber optic sensors. Light is transmitted into the first optical fiber, then it exits and travels into the second fiber; where both fibers are separated at a small distance x. As the distance x changes, the intensity variation of light is detected. The interferometer type sensors provide high accuracy for measuring temperature. Typical interferometers are Mach-Zender, Michelson, Sagnac and Fabry-Perot interferometers. The idea of interferometer is that when temperature varies, the light that travels along the sensing and reference fibers will induce phase shift which causes the optical fiber to expand or contract [4].

Four main types of fiber optic sensors used in civil engineering applications are characterized as follows [9]: (a) Point sensors consist of a single measurement point at the end of the fiber optic line. (b) Multiplexed sensors permit multi-points measurement along a single fiber cable. (c) Long-base sensors allow the measurement over a certain sensing length. (d) Distributed sensors provide the capability of sensing at any point along a single fiber line.

1.3 Research Objectives

The objectives of this research are described in the following:

- To investigate early-age concrete hydration heat using Fabry-Perot (FP) fiber optic temperature sensors in order to obtain temperature development within concrete structures.
- To validate the performance of a new FP sensor used in this thesis work.

1.4 Research Approach

Two sets of experiments were conducted to collect temperature profiles of concrete cylinders with various water-to-cement (w/c) ratios (ranging from 0.4 to 0.6) in a styrofoam chamber. The first set of experiment used one FP fiber optic sensor and a thermocouple sensor. The second set of experiment used two FP sensors.

First set of experiment. 4"×8" specimens were cast with three w/c ratios, 0.4, 0.5 and 0.6. Each specimen was put into a styrofoam chamber to achieve thermal insulation. Temperature profile of each specimen was collected by a Fabry-Perot (FP) fiber optic temperature sensor and a type K thermocouple sensor for 70 hours counting immediately after concrete placement.

Second set of experiment. 3"×6" specimens were cast with five w/c ratios, 0.4, 0.45, 0.5, 0.55 and 0.6. Each specimen was inserted into a styrofoam chamber, where the styrofoam chamber was stored in a temperature-controlled glass chamber at a fixed temperature of 25^oC. Temperature profile of each specimen was recorded by two FP

fiber optic temperature sensors for approximately 45 hours counting immediately after concrete placement.

Based on the measured data, the amount of hydration heat release, apparent activation energy were calculated using theoretical models.

1.5 Organization of the Thesis

The organization of this thesis is as outlined below.

Chapter 2 reviews (a) experimental studies of concrete temperature and heat of hydration behavior; (b) studies of: (i) concrete temperature prediction methods, (ii) apparent activation energy; and (c) fiber optic temperature sensors in the experimental studies of concrete and in practical applications.

Chapter 3 describes the experimental program

Chapter 4 explains Fabry-Perot fiber optic temperature sensors used in this study.

Chapter 5 provides experimental results and discussion.

Chapter 6 presents theoretical models, results and discussion of heat of hydration and apparent activation energy in hardening concrete.

Chapter 7 concludes the finding obtained from this thesis research.

Chapter 2

Literature Review

2.1 Concrete Hydration

2.1.1 Hydration Heat

Cement hydration begins when cement is in contact with water. Hydration reactions are all exothermic which liberate heat and raise concrete temperature [15, 19]. Concrete at early age produces the greatest rate of heat liberation within the first 24 hours. A large amount of heat is developed within the first 3 days of hydration [19].

Rate of heat generation can be represented by a calorimetric curve as shown in Figure 2-1. According to Figure 2-1, cement hydration consists of five stages [15]:

1. Initial dissolution of solids: Heat rapidly evolves at this stage.

2. Induction period: Concrete is in plastic state for several hours, then initial set happens in 2 to 4 hours at the end of this period.

3. Acceleration period: In this stage, the greatest rate of heat evolution which leads to concrete final set occurs. Initial hydration products are formed.

4. Deceleration period: Hydration products continue to grow and concrete starts gaining its early strength.

5. Steady state period: Hydration products are forming at a slower rate.

Four major chemical compounds that account for the hydrated cement are ordered from fastest to slowest rates of reaction with water as follow [15, 10]: C_3S (Tricalcium Silicate) > C_2S (Dicalcium Silicate) > C_3A (Tricalcium Aluminate) > C_4AF (Tetracalcium Aluminoferrite).

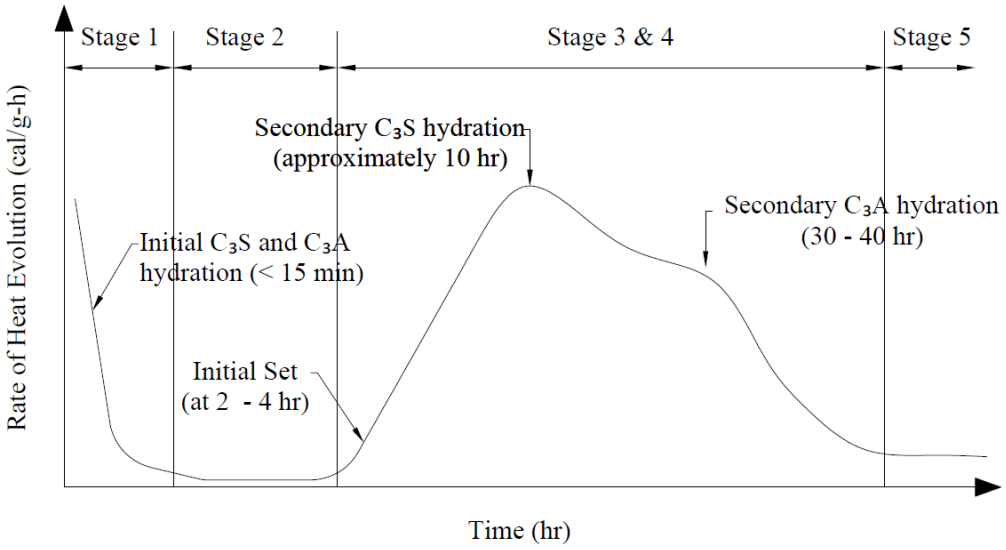

Figure 2-1: Rate of heat generation during hydration of Portland cement

The rate of heat evolution and total heat liberation are mainly related to: (a) cement composition, (b) cement fineness (blaine value), (c) cement content, (d) casting temperature, and (e) water to cementitious ratio (w/cm) [15, 19]. The typical chemical composition of ASTM Types I to V of Portland cement is presented in Table 2.1.

Table 2.1: Typical Chemical Composition of Portland Cements, ASTM Types I to V [15]

Compound	I	II	III	IV	V
C_3S	55	55	55	42	55
C_2S	18	19	17	32	22
C_3A	10	6	10	4	4
C_4AF	8	11	8	15	12

Influence of the water-cement ratio. Higher water to cement (w/c) ratios increase the rate of hydration during stage 3, but it has less impact during early stage of hydration. Theoretically, 100% of hydration can be achieved when the w/c ratio is at or above 0.4.

Influence of cement fineness. Ultimate degree of hydration (α_u) is increased when cement fineness increases. However, cement fineness has less effect on α_u when the w/c ratio is low [1]. Generally, higher cement fineness provides more surface area for water to react with cement which can enhance the rate of hydration and increase the potential degree of hydration (DOH).

Influence of the curing temperature. Reaction rate increases when the curing temperature increases. However, the rate of permeability decreases at higher temperature which prevent the contact between water and hydration products. As a result, α_u is lower at later stage of hydration [33].

2.1.2 Thermal Properties

Thermal properties of concrete include (a) thermal expansion (CTE): materials's expansion or contraction with temperature; (b) thermal conductivity (k): is the ratio of heat flux to differential of temperature or in another word, thermal conductivity is the rate of heat transmitted through a material when there is temperature difference between two faces; and (c) specific heat (C_p): is the ratio of the amount of heat required to raise a unit weight of a material by 1 ^oC. Specific heat strongly depends on porosity, w/c ratio and temperature [15]. The thermal properties of concrete obtained from literatures are presented in Table 2.2.

2.1.3 Experimental Studies of Concrete Temperature and Hydration Behavior

Many researchers adopted calorimetry tests to obtain hydration parameters in order to gain a better understand the behavior of concrete hydration heat. In this section, a detailed description of concrete experimental studies performed by many researchers are presented.

Xu *et. al.* [40] conducted calorimetries tests on cement mortar and concrete specimens to determine cement hydration properties and predicted early age temperature profiles of Portland cement concrete pavement (PCCP). Class C fly ashes (FA) and water reducers were applied on all specimens. Starting from initial temperature until peak temperature, the heat of hydration is the primary contribution. After 12 hours of casting, the PCCP temperature varied according to air temperature.

Table 2.2: Thermal Properties of Concrete Constituents

	k		C_p		CTE	
	$W/m{\cdot}\mathrm{K}$	$Btu/ft{\cdot}\mathrm{h}{\cdot}^oF$	$J/kg\cdot{}^oC$	$Btu/lb\cdot{}^oF$	$10^{-6}/{}^oC$	$10^{-6}/{}^oF$
Aggregate						
Granite	3.1	1.8	800	0.19	7-9	4-5
Basalt	1.4	0.8	840	0.2	6-8	3.3-4.4
Limestone	3.1	1.8	-	-	6	3.3
Dolomite	3.6	2.1	-	-	7-10	4-5.5
Sandstone	3.9	2.3	-	-	11-12	6.1-6.7
Quartzite	4.3	2.5	-	-	11-13	6.1-7.2
Marble	2.7	1.6	-	-	4-7	2.2-4
Cement paste[a]						
$w/c = 0.4$	1.3	0.75	-	-	18-20	10-11
$w/c = 0.5$	1.2	0.7	-	-	18-20	10-11
$w/c = 0.6$	1.0	0.6	1600	0.38	18-20	10-11
Concrete	1.5-3.5	0.9-2	840-1170	0.2-0.28	7.4-13	4.1-7.3
Water	0.5	0.3	4180	1	-	-

[a]Saturated condition.

Kuder *et. al.* [12] studied the concrete temperature development by taking size effect, addition of Class F fly ash and insulation into consideration. Wall thickness of 101.6 mm, 203.2 mm and 304.8 mm were investigated. In order to evaluate the effect of insulation, a 203.2mm thick wall was insulated by a 50.8mm insulator. Semi-adiabatic test method was used to determine hydration process with the presence of fly ash. In addition, regular concrete with different wall thickness specimens had achieved higher peak temperature than those with 40% fly ash. ”Normal concrete” temperature increases as its thickness increases. Concrete walls (both with and without fly ash) of

203.2mm thick (which was insulated) experienced a higher peak temperature than the ones exposed to the ambient environment.

Schindler *et. al.* [29] studied the impacts of high temperature on concrete pavement behavior during construction in order to predict the long-term performance of concrete pavement. In this study, the data obtained from the ”Texas Rigid Pavement” was used for concrete pavement analysis. It should be noticed that the development of concrete temperaturevaries according to air temperature. Air temperature plays a critical role in predicting the long term behavior of concrete pavement. As the air temperature during concrete placement increases, the chance of concrete construction failure increases.

Xiong *et. al.* [39] performed isothermal calorimetry test on Portland cement (”CEM I 52.5R”) and ”blast furnace slag cement (BFSC)” to study the effects of three adiabatic temperatures (20, 30 and 40 ^oC) on concrete hydration heat.Water to cement ratios (w/c) of 0.4 and 0.6 were used. Before the experimental measurement started, the calorimeter was stored in a room with temperature of 20 ^oC and relative humidity of 75%; both water and cement were placed in the oven for 24 hours to meet the preferred mixing temperature. According to their experimental results, Portland cement generated two peaks of thermal power and it achieved higher peak thermal power value than BFSC for all adiabatic temperature conditions. It was noticed that at adiabatic temperature of 20 ^oC, Portland cement with w/c of 0.6 generated higher peak thermal power than the specimen with w/c equals 0.4. In contrast, when the adiabatic temperature was raised to 30 ^oC and 40 ^oC, Portland cement with w/c of 0.6 reached a lower peak thermal power value than specimen with w/c of 0.4. The possible reasons could due to concrete with higher w/c that was cured at higher temperature did not have sufficient time for

available water to react with cement.

Schindler [25] performed experimental study on various concrete mixtures in laboratory and in the field to determine initial and final setting time of concrete. In this study, initial and final set times of concrete were considered as a function of the degree of hydration. Data of 7 concrete pavement projects located at various locations (in different seasons) in Texas were collected. The mixtures for the 7 projects consisted of varying w/c of 0.39 , 0.44, 0.46 , 0.41 , 0.54, 0.50and 0.41 were tested under semi-adiabatic condition to determine the degree of hydration. The values of equivalent age at initial and final setting time were determined from concrete cylinder temperature data.

Graham *et. al.* [5] studied the effectiveness of various cement fineness to reduce concrete peak temperature during early age development. Two clinkers (A & B) from distinct manufacturers were used for producing five different cement fineness; where cements from Clinker A have fineness ranging from 2640 cm^2/g to 4980 cm^2/g, and cements from Clinker B have fineness ranging from 2660 cm^2/g to 4943 cm^2/g. 10 concrete samples were casted by using the cements that produced by Clinker A and B. All samples were tested in an adiabatic calorimetry where water was used as a temperature controller within the chamber. According to experimental results, when cement fineness increases, the total amount of heat liberated increases by 17% for cements from Clinker A and 32% for cements from Clinker B. The total amount of heat generated from both clinkers were different due to the availability of C_3S and C_2S.

Guo *et. al.* [6] performed experiments under adiabatic conditions to study the temperature distribution within ”high slag blast furnace cement (HSPBFC)” concrete.

Ssang Yong commercially available ordinary Portland cement (OPC) and HSPBFC (with various percentage of GGBS) cements were selected for this study. The experimental results showed that temperature rising rate is significant during early age of cement hydration process.

Schindler *et. al.* [27] performed semi-adiabatic calorimetry tests on thirteen different mixtures to study hydration heat development of cementitious materials. Specimen with a diameter of 6 inches and a height of 12 inches was used as a standard size for this experimental study. Various amounts of ASTM Type I cement with supplemental cemtitious materials (SCMs) were used. According to experimental results, Class C fly ash showed a delay during early acceleration stage, and it produced little effect on the total amount of heat of hydration generated. When the amount of Class F fly ash was increased, both rate of hydration and total heat generation were greatly decreased. With the present of GGBF, the rate of hydration was reduced during accelerating period, however, it did not affect the amount of heat that was generated. CaO content in fly ash is a main source in generating different value of heat of hydration for various fly ash types.

2.1.4 Concrete Temperature Prediction Methods

Many researchers proposed different methods in predicting concrete temperature. A variety of methods are discussed in the following paragraphs.

Riding *et. al.* [23] applied three different calculation methods to predict real temperatures of the following concrete bridge members: (a) two columns, two footings,

(b) one pedestal, one dolphin, (c) one rectangular bent cap, and one T-shaped bent cap. The three calculation methods are Portland cement Association's (PCA) method, ACI 207.2R graphical method, and the Schmidt Method [23]. According to actual temperatures and predicted temperatures, PCA method showed a good correlation with the actual peak temperature of Column 1, Column 2, rectangular bent cap, Footing 2, and the T-shaped bent cap. However, this method did not give a good prediction for other concrete members, since it under-estimated the maximum temperature compared to actual measurement. "Graphical method of ACI 207.2R" is not reliable because it under-estimated peak temperatures for all concrete elements in their study. The Schmidt method mainly relies on heat transfer and heat generation elements. The Schmidt method takes surface conditions which can be affected by "convection and solar radiation". Heat transfer strategy assumes constant thermal diffusivity of concrete. This type of strategy takes the increase of adiabatic temperature and the amount of heat loss within the mass concrete core into consideration. Heat generation strategy can be utilized by isothermal calorimetry results. The actual temperature curve consists of a lower trend, while the calculated maximum temperature vs. time is greater than the actual value. The difference caused by the heat loss is due to the surrounding environment and deceleration of heat generated between 24 to 72 hours.

Riding *et. al.* [24] proposed a mass concrete temperature prediction model by considering convection, radiation and shading effects. A semi-adiabatic calorimetry test was conducted to obtain hydration parameters including ultimate degree of hydration (α_u), hydration curve parameter (β), hydration time parameter (τ), activation energy (E_a) and potential heat (H_u). According to their semi-adiabatic calorimetry test, the

minimum and maximum values of activation energy were 29,400 J/mol and 41,300 J/mol, respectively. A total number of 137 temperature sensors with a sampling rate of 15-minute per data point were embedded into concrete members.The temperature data collected from each sensor was used in comparison with the predicted temperature which was based on the finite difference heat transfer model. The results showed that the ”average absolute error” for all members has a range from 0.5 to 4.6 ^oC.

Additionally, according to [40], temperature rise under adiabatic condition can be determined as an integral of the ratio between incremental heat of hydration and concrete specific heat as follow:

$$T(t) = \int_t^{t_o} \frac{\Delta H(t)}{C_p} \tag{2.1}$$

2.1.5 Apparent Activation Energy

Some researchers performed extensive study in determining methods for the calculation of activation energy. Activation energy is known as the energy required to overcome the hydration reaction between water and cement particle. Activation energy can also be considered as the most common method in the prediction of temperature sensitivity for hydrated products [20]. Following paragraphs will introduce these methods for the estimation of activation energy.

Schindler [26] conducted a literature review on activation energy of cementitious materials.Values of activation energy proposed in Schindler’s literature review are discussed as following:

- Freiesleben Hansen and Pedersen (FHP) (1977) stated that the activation energy

is independent of type of cement or mineral admixtures, but it depends on concrete temperature as expressed in Eq. 2.2.

$$for T_c \geq 20^oC (68^oF) : E(T_c) = 33,500 J/mol$$

$$for T_c \leq 20^oC (68^oF) : E(T_c) = 33,500 + 1470(20 - T_c) J/mol \quad (2.2)$$

- According to Carino (1991), activation energy is a function of cement content, cement fineness, and mineral admixtures that are used in a mixture [26]. Carino added that the values of activation energy range from 41,000 to 67,000 J/mol and are independent of concrete temperature.

- Based on ASTM C 1074, when strength is taken into consideration, activation energy has a range of 40,000 to 45,000 J/mol when 100 % of Type I cement is used.

- Kjellsen and Detwiler (1992) reported that an activation energy depends on temperature that causes by heat of hydration and the progress of strength within concrete structure.

- Jonasson *et. al.* (1995) proposed that the activation energy depends on concrete temperature (T_c).

Ma *et. al.* [13] performed isothermal calorimetry tests at adiabatic conditions from 10 to 55 ^oC with a 5 ^oC increment. By applying the Arrhenius theory (independent of concrete temperature), the values of activation energy (E_a) of the following were found:

- E_a equals to 39,000 J/mol for Type I cement
- E_a equals to 26,700 J/mol for Type I cement + 17% Class F fly ash
- E_a equals to 49,300 J/mol for Type I cement + 65% GGBFS.

According to the results shown above, activation energy varies with the type of cementitious materials used. In short, activation energy was reduced by 32% when 17% of fly ash was added to cementitious materials. In contrast, activation energy was increased by 26% when 65% of GGBFS was used.

2.1.6 Summary

Many researchers implemented different methods in order to investigate concrete hydration heat. Direct method is either conducted under adiabatic condition (in a laboratory) or field condition. Indirect method performs analytical analysis with the aid of hydration parameters which can obtain from calorimetry test. Each method has its own advantages and limitations. Some researchers reported similar or dissimilar results and had different or similar perspectives on the relationship between apparent activation energy and concrete material properties. As a result, further research is needed in order to gain a better understanding of concrete hydration behavior.

2.2 Fiber Optic Sensors

2.2.1 Fiber Optic Sensors in Concrete Experiments

Many researchers used fiber optic sensors in many experimental studies including biomedical, pressure, stresses, chemical, petroleum and pH etc... The use of fiber optic sensors in civil engineering applications is relatively in its early stage due to issues with sensor instrumentation. For instance, few researchers used fiber optic sensors in determining concrete temperature development. Some studies associated with the embedment of fiber optic sensors are presented in the following paragraphs.

Zeng *et. al.* [41] used Brillouin-scattering-based distributed FOS for both temperature and strain measurements along a 1.65m reinforced concrete beam. The sensor had an accuracy of $\pm 5\ \mu\varepsilon$. Wu *et al.* [38] applied distributed FOS on to full-scale prestressed concrete girder to study the structure performance. The FOSs showed good results compared to conventional strain gage for tensile strain measurement.

Rao *et. al.* [21] measured strain, temperature and vibration simultaneously by using a quasi-distributed fiber bragg grating (FBG)/fiber-fabry-perot interferometric (FFPI) sensor system. FFPI was formed by writing two FBGs with the same central wavelength, using low coherence interferometry to obtain high sensitivity. The broadband light source used was 20 mW with bandwidth of 40nm (wavelength: 1530-1570 nm) In addition, Mach-Zeh-Interferometer type was used to process interferometer for the FFPIs. Experimental results of strain and temperature measurands showed a very good linear relationship between strains vs. wavelength, and temperature vs. wavelength.

Tjin *et. al.* [32] embedded FBG temperature sensor arrays into concrete beam and

concrete slab to measure structure temperature distribution. FBG for temperature measurements packaged in 3.5 cm long metal tubing to protect FBG from external stress and pressure and to increase temperature sensing range and sensitivity. FBG wavelength has a linear relationship with temperature changes at sensitivity of 25 pm/^oC, resolution of 1pm (or 0.04 ^oC) and accuracy of 5pm (0.2 ^oC). The resultsdemonstrated that proper installation of FBG sensors increases FBG's survival in harsh conditions and provide an accurate reading of temperature measurements.

Wang *et. al.* [35] measured temperature variation within concrete structures at different depths using embedded fiber Brag grating (FBG) sensors and thermocouple sensors. Six concrete cubes with overall dimension of 350 x 250 x 400 mm but with different bituminous layer thickness of 0, 50, 75, 100, 125 and 150 mm were cured and exposed to solar heat for 24 hours. Experimental results showed FBGs provided a better temperature analysis then thermocouple.

Yun *et. al.* [37] embedded fiber Brag grating sensors (FBG) into higher performance concrete (HPC) columns to evaluate early age autogenous shrinkage (AS). The experiment was carried out for 33 hours to monitor AS for long term durability prediction purpose. Three groups of specimens were cast: (1) G1: 40x40x100 cm^3 (with rebar and without rebar), (2) G2: 32x32x50 cm^3 (with rebar and without rebar), (3) G3: 32x32x50 cm^3 (with rebar and without rebar and insulated with 15 cm thick sponge slab). In the experimental study, their results showed that size effect and hydration temperature have low impact on the very early age AS. Later, hydration temperature leads to higher AS. In addition, specimens that were thermally insulated reached the highest temperature.

2.2.2 Fiber Optic Sensors in Civil Engineering Applications

Ou and Zhou [18] studied FBG's performance in more than 10 bridges in China. The installed sensors were used to measure strain, stress and temperature of bridges. For example, Yonghe Bridge in Tianjin City, China, was successfully equipped with 40 FBG strain sensors, 10 FBG temperature sensors, and 96 FBG cable sensors. During the loading test, main beam strain, and stress of the prestressed rebars and the cables of the bridge were evaluated. The results indicated that FBG can be used as structural health monitoring system for bridges over other conventional electrical sensors.

According to [8], I-35W bridge in Minneapolis collapsed which brought great attention to public safety. To restore public confidence of bridge safety, structural health monitoring system was implemented into the new I35W Bridge. The main target of this monitoring system was to ensure bridge security, to monitor structural behavior during and after construction. The system consisted of 323 sensors, where they spreaded out in all spans. The installed sensors were vibration wire strain gages, thermistors, linear potentiometers, accelerometers, concrete carrion and humidity sensors, and SOFO long-guage fiber optic deformation sensors. The pictures of sensors are shown in Figure 2-2.

2.2.3 Summary

According to the literature review on previous research, the structural health of civil infrastructures can be improved using structural health monitoring systems which incorporated non-destructive sensing technologies. For instance, fiber optic sensors play

(a) Long-gauge SOFO fiber optic sensor

(b) Vibrating Wire Strain Gauge

(c) Concrete corrosion and Humidity sensors

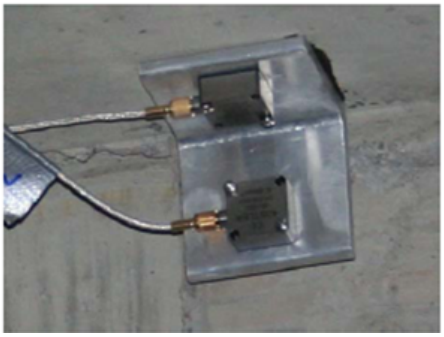

(d) Accelerometer

(e) SOFO Fiber Optic Sensor Datalogger

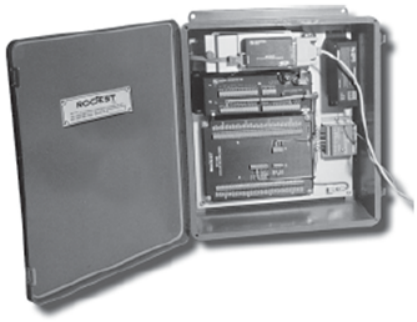

(f) Vibrating wire and temperature sensors datalogger

Figure 2-2: Overview of sensors and data acquisitions systems installed in the I35W Bridge [8]

a main role in providing civil engineering with structural conditions in the construction phase to verify design, and in the post construction phase to ensure structures are risk free in service. However, the implementation of fiber optic sensors in civil infrastructures is still not widely seen, and reported.

Chapter 3

Experimental Program

In this chapter, experimental program of the research is described. A summary of the experimental program of this research is presented in Figure 3-1.

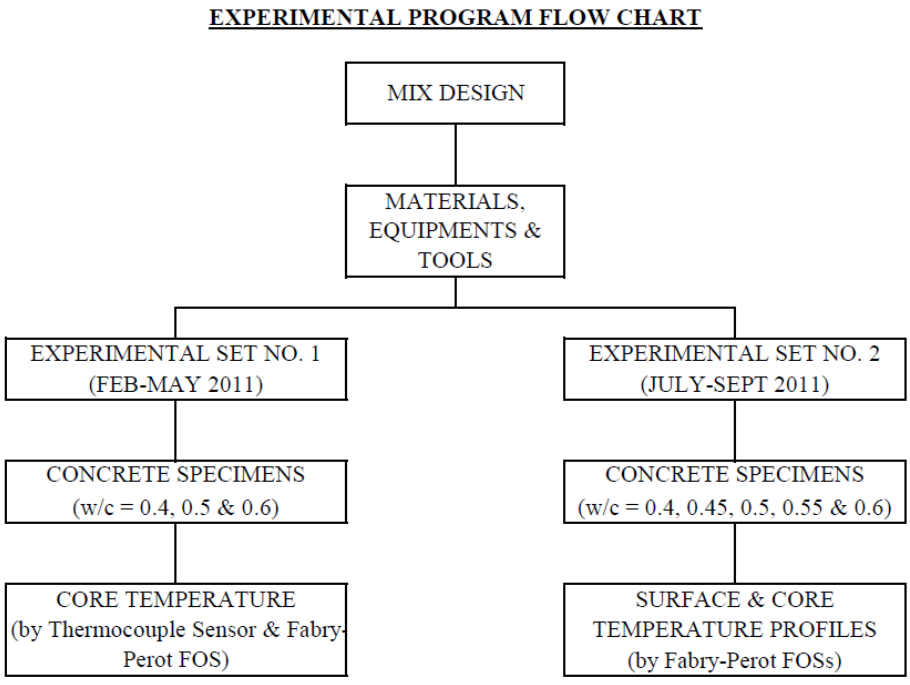

Figure 3-1: Experimental program flow chart

3.1 Concrete Mix Design

In this study, ASTM (American Society for Testing and Materials) Type I/II Portland cement and 3/8” gravels were used. The amount of cement, sand and gravel was kept at 1.51 lb, 2.562 lb and 3.719 lb, respectively for cylinder specimens with dimensions of diameter D = 4” and height H = 8”. Amount of cement, sand and gravel was fixed at 0.637 lb, 1.081 lb, and 1.569 lb, respectively for cylinder specimens with dimension of D = 3” and H = 6”. The percentage of water absorption for surface-dry sand was considered to be 0.5% (by weight) and for surface-dry gravel 1% (by weight). The amount of mixing water was adjusted in order to compensate the loss of water absorbed by surface-dry sand and surface-dry gravel.

Concrete mix design for specimens with cylinder dimensions of 4”×8” and 3”×6” are calculated based on the PCA volume method. Detailed calculation procedure of a concrete cylinder specimen with a diameter of 4”, a height of 8”, and the water-to-cement ratio of 0.5 is presented in Appendix A. A summary of mix design for 4”×8” and 3”×6” concrete cylinders with w/c ratios ranging from 0.4 to 0.6 are presented in Table 3.1 and Table 3.2, respectively.

Portland cement is composed of several chemical components. The four major compounds are tricalcium silicate (C_3S), dicalcium silicate (C_2S), tricalcium aluminate (C_3A), and tetracalcium aluminoferrite (C_4AF). Table 3.3 lists the chemical compositions of Type I and Type II cement. Only the chemical composition of Type I cement will be used for calculation in this thesis).

Table 3.1: Mix design for 4” x 8” concrete cylinders

	w/c		
Component (lb)	0.4	0.5	0.6
Cement	1.510	1.510	1.510
Sand	2.562	2.562	2.562
Gravel	3.719	3.719	3.719
Water	0.648	0.799	0.950
Total	8.439	8.590	8.741

Table 3.2: Mix design for 3” x 6” concrete cylinders

	w/c				
Component (lb)	0.4	0.45	0.5	0.55	0.6
Cement	0.637	0.637	0.637	0.637	0.637
Sand	1.081	1.081	1.081	1.081	1.081
Gravel	1.569	1.569	1.569	1.569	1.569
Water	0.273	0.305	0.337	0.369	0.401
Total	3.560	3.592	3.624	3.656	3.688

3.1.1 Concrete Specimen Preparation

Cylinders specimens with a diameter of 4-in and a height of 8-in were used. An example using 0.4 water-to-cement ratio in developing the procedure which is described in the following and presented in Figure 3-2.

- Step 1: Mix all the dry materials (cement, sand and gravel) thoroughly, then make a concave up profile in the center of the mixed materials.

- Step 2: Carefully pour water for approximately 20% at a time to the hole created in Step 1, then thoroughly mix.

Table 3.3: Chemical and Phase Composition of ASTM C150/AASHTO M 85 Portland Cements in 2004, % by mass

Chemical Composition	Type I Cement	Type II Cement
SiO_2	20.17	20.85
Al_2O_3	5.07	4.62
Fe_2O_3	2.66	3.32
CaO	63.23	63.66
MgO	2.51	1.98
SO_3	3.26	2.91
Na_2O	0.7	0.56
C_3S	56.9	56.5
C_2S	14.8	17.1
C_3A	8.9	6.7
C_4AF	8.2	10.1
Loss on ignition	1.52	1.39
Insoluble residue	0.29	0.29
Blaine (m^2/kg)	384	377

*Source:*Bhatty, Javed I., Tennis,Paul D., Portland Cement, U.S and Canadian Cement Charateristics: 2004, PCA

- Step 3: Repeat Step 2 until there is no more water left in the container.
- Step 4: Pour one scoop of concrete into a cylinder form, then thoroughly compact the layer approximately 50 times (25 - 30 times for the concrete with a w/c ratio higher than 0.45) with a steel rod.
- Step 5: Repeat Step 4 until all materials are completely mixed.
- Step 6: Use the steel rod to tap along both sides of cylinder in order to reduce

Figure 3-2: Casting concrete procedure

void that may exist between each compacted layer.

3.2 Wireless Temperature Sensor

Variation of ambient temperature is crucial in the study of early age concrete hydration heat. Therefore, a wireless temperature sensor was used for ambient temperature measurement. In the following, the calibration and validation of the wireless sensor are presented.

3.2.1 Sensor Calibration Method and Result

1. Install EasyLog USB software onto the computer used for the wireless temperature sensor.

2. Plug the wireless temperature sensor into a USB port of the computer.

3. Start EasyLog software

    - Select the first button in green
    - Select the desired sample rate and temperature unit (^oC or ^oF)

4. Remove the wireless temperature sensor from the USB port and place it a at desired location.

5. Plug the device back into USB port of the computer after the measurement is completed.

6. Open EasyLog software to stop recording, review and save the recorded data.

Two calibration tests were performed to determine the accuracy of the wireless temperature sensor. In each test, the wireless temperature sensor was kept in a temperature-controlled glass chamber for 24 hours, where the temperature was set at 25 ^oC. Sampling rate was set to 1 data point per minute in each test. Both calibration results indicate that the sensor has an accuracy of $\pm 0.5^oC$.

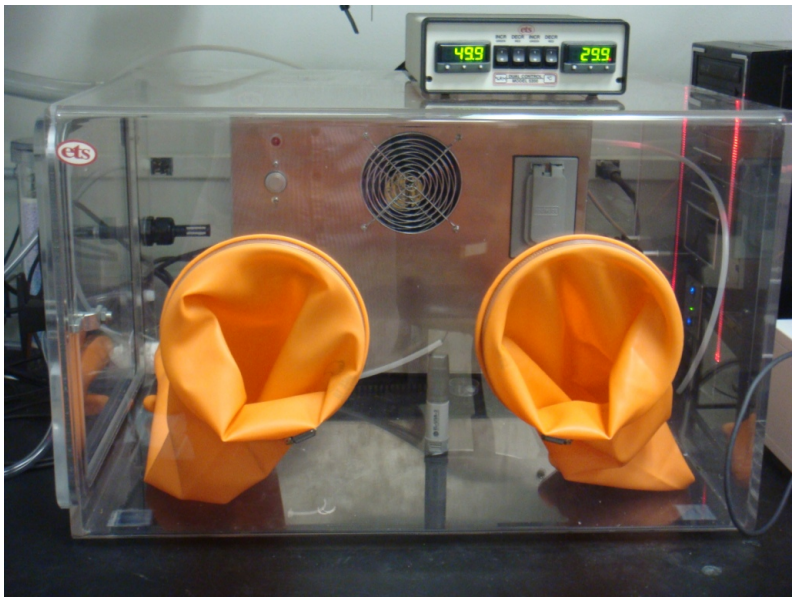

Figure 3-3: Wireless temperature at the center of the glass chamber

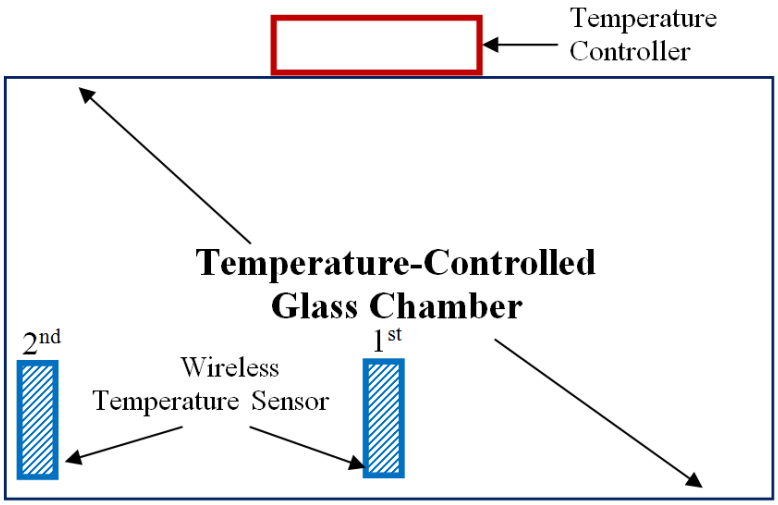

Figure 3-4: Schematic of wireless temperature sensor at the center and the corner of the glass chamber

3.3 Experimental Setup

3.3.1 Experimental Setup for 4inch-by-8inch Concrete Cylinders

The experiment was conducted to study the temperature variation during the first 70 hours at a sampling rate of 20 seconds per reading. The concrete cylinder specimen was

stored in a $1 \times 1 \times 1 ft^3$ styrofoam chamber to simulate a thermal insulated condition. The test setup is illustrated in Figure 3-5.

Equipments: computer (recorded experimental data), Optical Sensing Analyzer si720 (generated light source) and Styrofoam chamber (($1 \times 1 \times 1 ft^3$), used for insulating concrete specimens).

Sensing tools and applications: FP fiber optic temperature sensor and type K thermo-couple sensor measuring core concrete temperature.

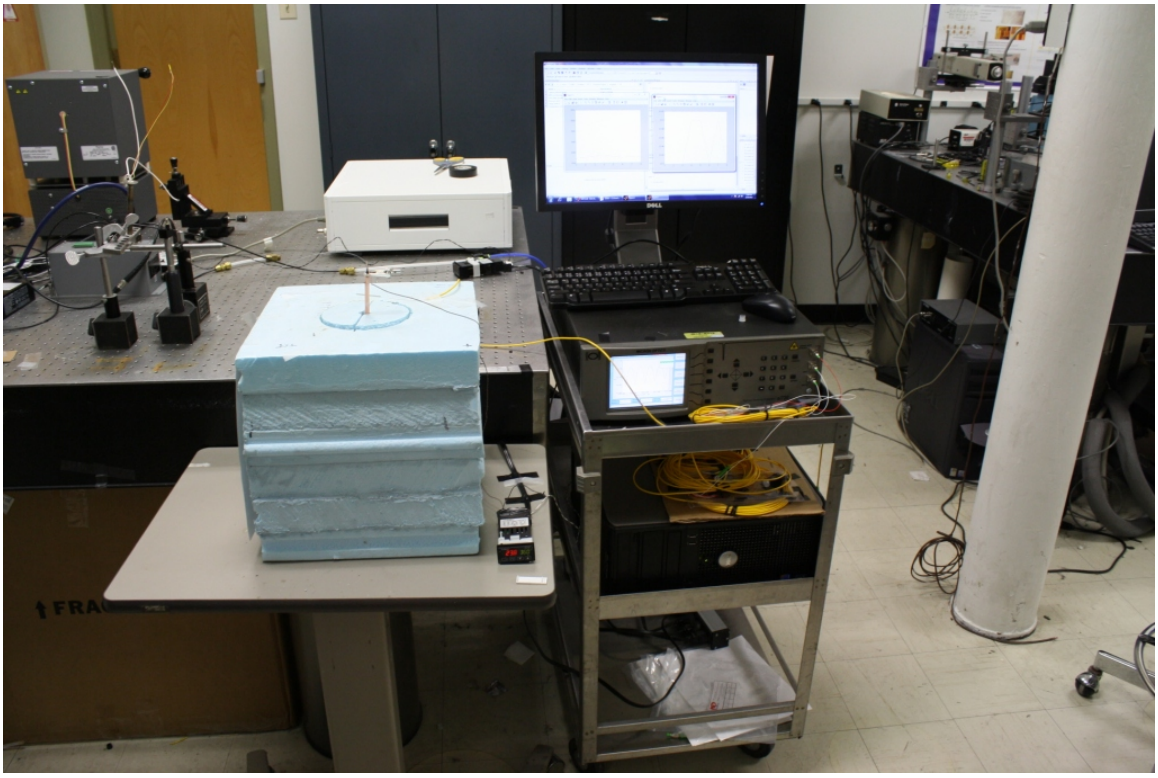

Figure 3-5: Experimental Setup (4"×8" Concrete Cylinder)

3.3.2 Experimental Setup for 3inch-by-6inch Concrete Cylinders

Prior to testing, all concrete mixtures were kept inside the temperature-controlled glass chamber at a fix temperature of 25 ^oC for approximately 45 hours. After concrete

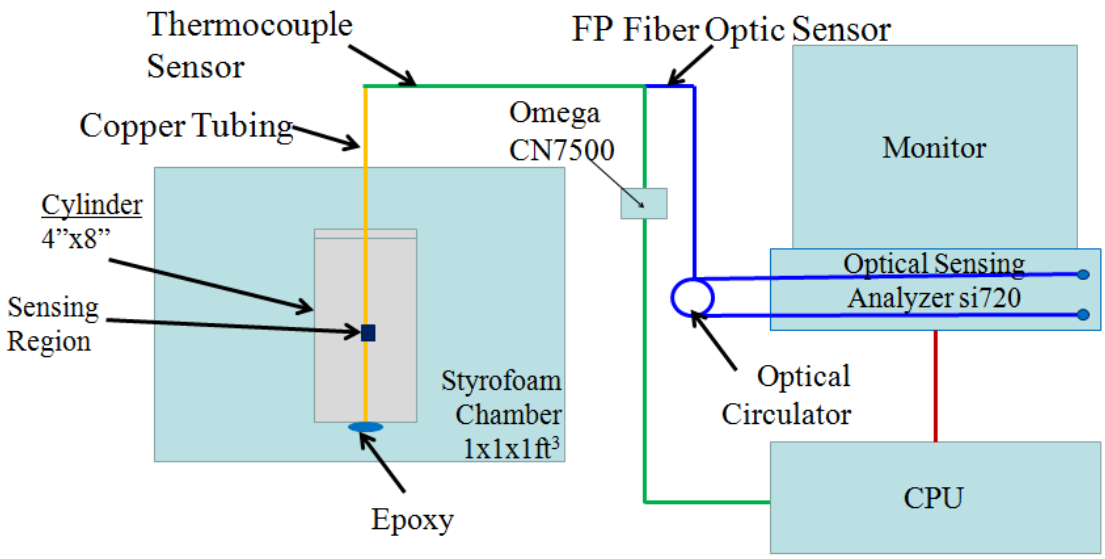

Figure 3-6: Schematic of Experimental Setup (4"×8" Concrete Cylinder)

mixing and casting, the specimen was put into a styrofoam chamber, where the chamber was kept inside the glass chamber at a constant temperature of 25 ^{o}C (see Figure 3-7). Concrete temperature was measured and recorded simultaneously for approximately 45 hours at 20 seconds per data point. In addition, a wireless ambient temperature sensor was placed at the top of the Styrofoam chamber to record temperature, relative humidity and dew point inside the glass chamber.

Equipments: Two computers, Optical Sensing Analyzer si720, temperature-controlled glass chamber, and Styrofoam chamber.

Sensing tools and applications

- Wireless ambient temperature sensor: records temperature, relative humidity and dew point in glass chamber.
- Humidity Alert II: provides temperature and relative humidity at concrete mixing and placement.

- Two Fabry-perot fiber optic temperature sensors: one measures temperature at the core of concrete cylinder specimen and the other one measured temperature at concrete's surface.

Figure 3-7: Experimental Setup (3"×6" Concrete Cylinder)

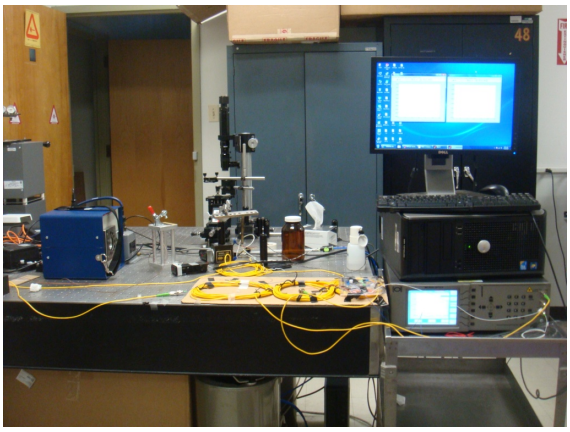

(a)

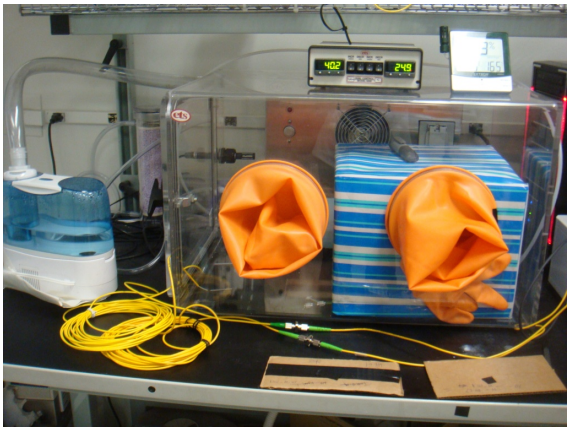

(b)

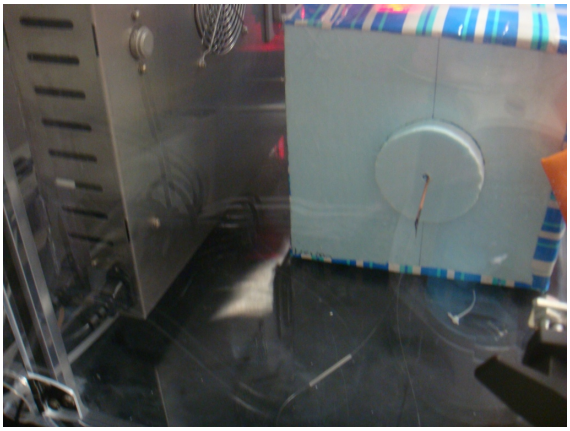

(c)

Figure 3-8: Detailed photos of experimental setup (3”×6” Concrete Cylinder)

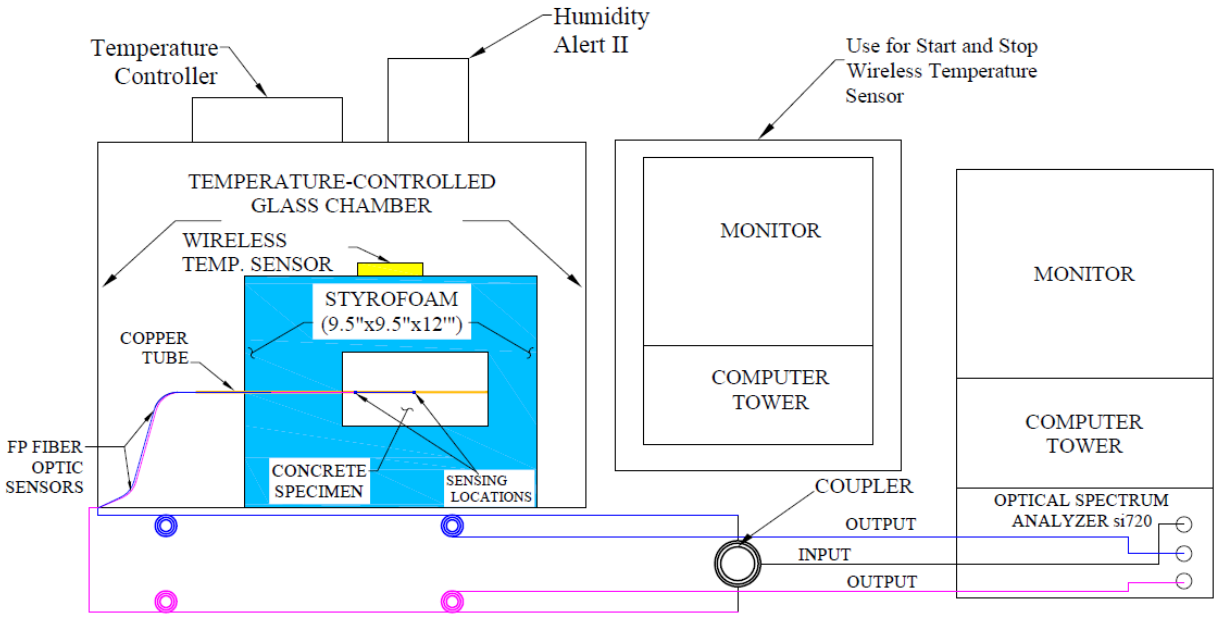

Figure 3-9: Schematic of Experimental Setup (3”×6” Concrete Cylinder)

Chapter 4

Fabry-Perot Fiber Optic Temperature Sensors

Fabry-Perot fiber optic temperature (FP) sensors are an outstanding candidate in measuring the temperature distribution within concrete specimen in this thesis research. Three FP fiber optic sensors consist of the same structure and material property were designed and manufactured by Xiaotian Zou from the Center for Electromagnetic Materials & Optical Systems at the University of Massachusetts Lowell. Three FP sensors consist of a very similar sensitivity which is approximately at 0.01 nm/^oC. In this chapter, a thorough description of the FP sensors used is presented in the following sections with the information provided by Xiaotian Zou.

4.1 Fabrication of Fabry-Perot Fiber Optic Temperature Sensors

Chemical etching has been widely used in the fabrication of fiber optic sensors. Microchannel [31], microgap [42], and microcavity [34] can be achieved with wet etching techniques. Moreover, a cavity cone structure can be fabricated in a fiber by a differential etching rate between the pure silica of the fiber cladding and the germanium-doped silica of fiber core. By following [11], the cavity cone angle of the etched fiber optic tip is inversely proportional to the volume ratio of ammonium fluoride buffered hydrogen fluoride. The cone angles can be adjusted by controlling the volume ratios of ammonium fluoride (NH4F). In this paper, the etching solution was composed of hydrofluoric acid (HF 49% in weight concentration), ammonium fluoride (NH4F 40% in weight concentration), and deionized water with a volume ratio NH4F : HF : H2O = 0.5 : 1 : 1. With this volume ratio, the etching rate of the fiber core could be faster than that of the fiber cladding.

A single-mode fiber (SMF) (Corning SMF-28) with core/cladding diameters of 8/125 μm was used in the fabrication of the fiber optic temperature sensor. The fiber was first cleaved using a cleaver (Fujikura CT-30B), with the cleaved angle of fiber endface controlled about an accuracy of 0.5 degrees as measured by a fusion splicer (Fitel S177A). The reflection intensity of the cleaved fiber was examined by an optical sensing analyzer (Micron Optics SI720 Component Testing System, CTS) to guarantee the quality of the endface. The protective coating was removed with a 6 mm long section after the fiber tip was cleaved. After that, the fiber was vertically dipped into a buffered

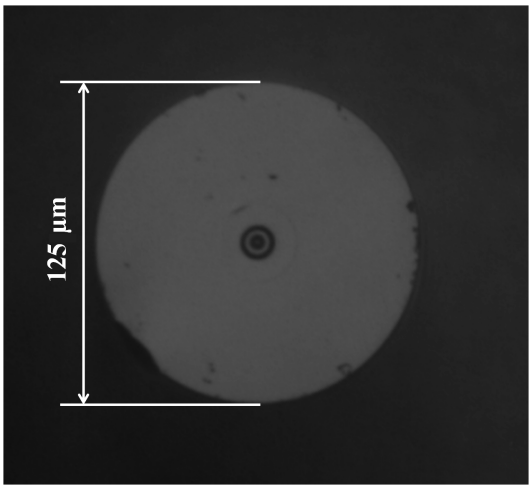

Figure 4-1: SMF endface after 15 min etching in buffered hydrogen fluoride [Courtesy of Xiaotian Zou]

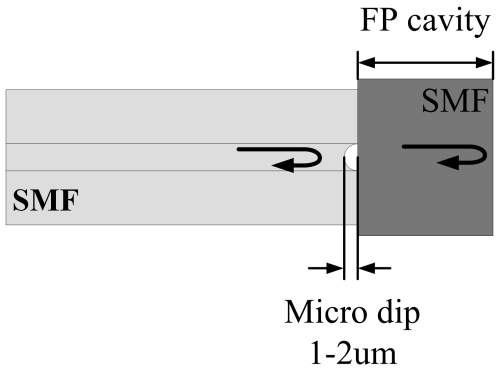

Figure 4-2: The design of Fabry-Perot fiber optic temperature sensor [Courtesy of Xiaotian Zou]

hydrofluoric solution for 15 minutes. After being rinsed in deionized water and drying, the endface of the fiber tip was examined under a microscope (Olympus IM). A typical etched fiber endface is shown in Figure 4-1. A micro dip was formed since the etching rate of the core was higher than that of the cladding.

Figure 4-2 shows the structural schematic of the FP fiber optic sensor. After the micro dip was formed, the etched fiber was spliced with another single mode fiber

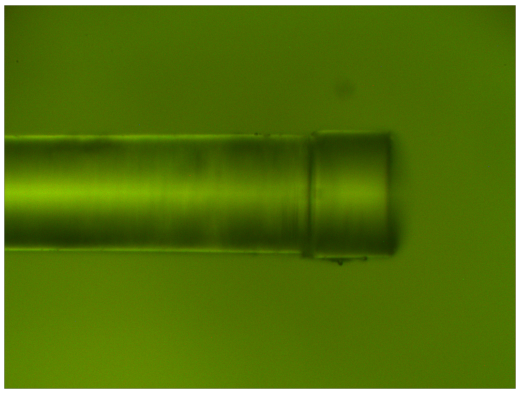

Figure 4-3: Photomicrograph of the microcavity Fabry-Perot fiber optic temperature sensor [Courtesy of Xiaotian Zou]

using the fusion splicer (Fitel S177A). Due to the small curvature of the micro dip, the air in the micro dip is very thin, so the reflection strength does not vary much over the optical range. Therefore, the micro dip behaves like one reflector of the FP cavity. By cleaving another single mode fiber 90 μm far from the dip, another reflector of the FP cavity was formed by the endface. The two fibers were then joined together to form an FP interferometer. The photomicrograph of the FP sensor is shown in Figure 4-3.

The FP fiber optic sensor can work as a temperature sensor in civil engineering applications by monitoring the changes in the reflection spectrum caused by the thermal expansion of the attached SMF section. The theoretical investigation will be provided in the next section.

4.2 Interrogation of the Optical-Fiber Temperature Sensors

4.2.1 Optical Characteristics of Sensors

As discussed in the previous section, the attached SMF section can serve as a temperature sensing element. In particular, when the sensor is exposed to environment, the attached SMF section will deform due to its thermal expansion properties, subsequently will cause a change of the FP cavity length. The low finesse FP device can thus be modelled using the two-beam optical interference equation [36]:

$$I = I_1 + I_2 + 2\sqrt{I_1 I_2}cos(\frac{4\pi z}{\lambda} + \phi)\,, \tag{4.1}$$

where I is the intensity of the interference signal, I_1 and I_2 are the reflections at the cavity endfaces, respectively, ϕ is the initial phase of the interference. λ is the optical wavelength in vacuum, z is the path difference. For intensity demodulation, optical intensity is recorded under one specific wavelength.

From the Equation 4.1, the path difference z equals to the refractive index of the cavity n times cavity length L. When the phase of the cosine term becomes an odd number of π, the interference signal reaches its minimum I_{min} will be expressed in the following

$$I = I_{min} \quad when \quad \frac{4\pi z}{\lambda_v} + \phi = (2m+1)\pi\,, \tag{4.2}$$

where m is an integer and λ_v is the center wavelength of the specific interference valley. Substitute the optical path difference (OPD) Δz, according to Equation 4.2 we will obtain the shift of the specific interference valley $\Delta\lambda_v$ correspondingly.

$$\Delta\lambda_v = \frac{4\pi\Delta z}{(2m+1)\pi - \phi} \approx \frac{2\Delta z}{m}\,. \tag{4.3}$$

The OPD z of the FP cavity is highly dependent on the environment temperature related to the SMF material's thermo-optic coefficient (TOC) and coefficient of thermal expansion (CTE). The change in refractive index n and cavity length with temperature can be expressed as:

$$\begin{aligned}
(\Delta\lambda_v)_t &= \frac{2n}{m}(\Delta L)_t + \frac{2L}{m}(\Delta n)_t\,,\\
(\Delta L)_t &= \alpha L\,,\\
(\Delta n)_t &= \beta n\,,\\
\Delta\lambda_v &= \frac{2nL}{m}(\alpha+\beta)\Delta T\,,
\end{aligned} \tag{4.4}$$

where α and β are the coefficient of thermal expansion (CTE) and hermo-optic coefficient (TOC) of the silica respectively and ΔT is the temperature change.

It can be seen from Equation 4.4 that the wavelength shift is proportional to the temperature variation, and the temperature sensitivity is determined by the thermal properties of the silica material. For an FP cavity with $L = 90\mu m$ and $n = 1.517$, if the wavelength of valleys $\lambda_v \in [1520 \quad 1570]$, thus $m \in [174 \quad 179]$. For silica fibers, the coefficients can be chosen as $\alpha = 0.5 \times 10^{-6}$ and $\beta = 6.9 \times 10^{-6}$. When we choose

$m = 174$ the temperature sensitivity of FP sensor is equal to $0.01\,nm/°C$.

4.2.2 Interrogation System and Sensor Calibration

The spectrum reflection test setup is illustrated in Figure 4-4. An optical sensing analyzer (Micron Optics SI720 Component Testing System, CTS) launched the laser signal (scan wavelength 1520 nm to 1570 nm at 2.5 pm resolution) into the FP fiber optic sensor, while the spectrum response of the reflected light was collected and monitored through a data acquisition system. The FP fiber optic temperature sensor was put alongside with a commercially available thermocouple (Omega, 5TC-GG-J-30-36) as a reference sensor in a controllable furnace. The output of the Omega thermocouple was assumed to be the true temperature value applied to the FP fiber optic sensor.

The reflection spectrum of the FP fiber optic sensor with a cavity length 90 μm was illustrated in Figure 4-5. The furnace was set up to increase the temperature from 10 °C to 75 °C. The spectrum data and the output of the thermocouple were continuously collected while the furnace temperature changed. Finally, the calibrated temperatures and the square errors between the FP sensor and thermocouple are shown in Figure 4-6. Sensitivity of the FP fiber optic sensor was 0.01 nm/°C. The linearity was good with a correlation coefficient of 0.99.

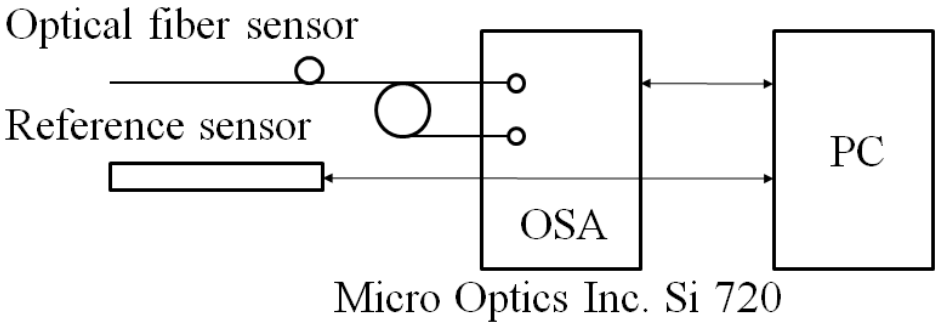

Figure 4-4: The interrogation scheme [Courtesy of Xiaotian Zou]

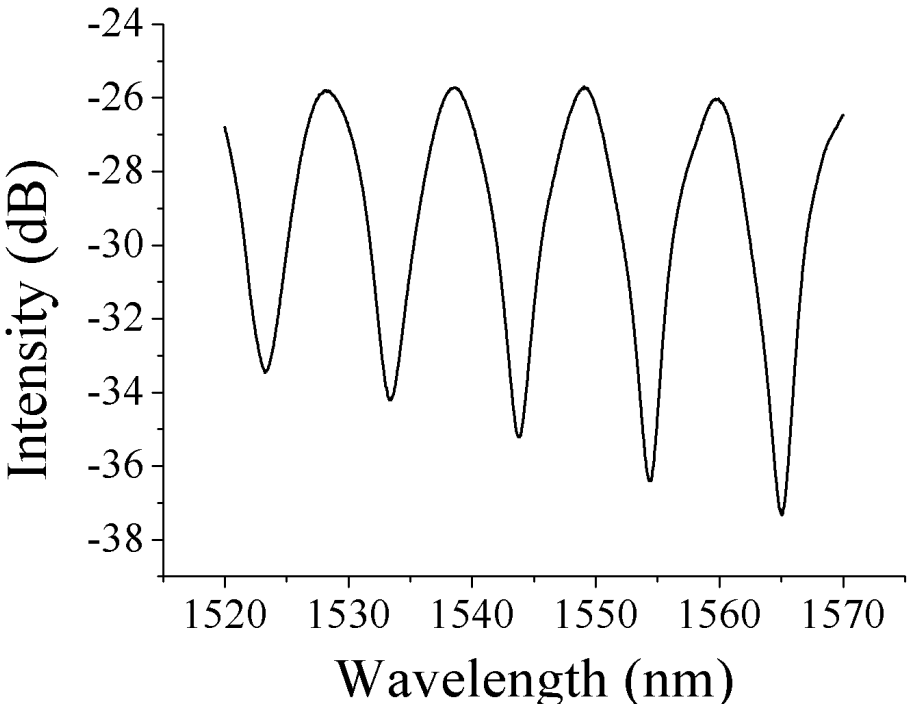

Figure 4-5: The reflection spectrum of the FP sensor [Courtesy of Xiaotian Zou]

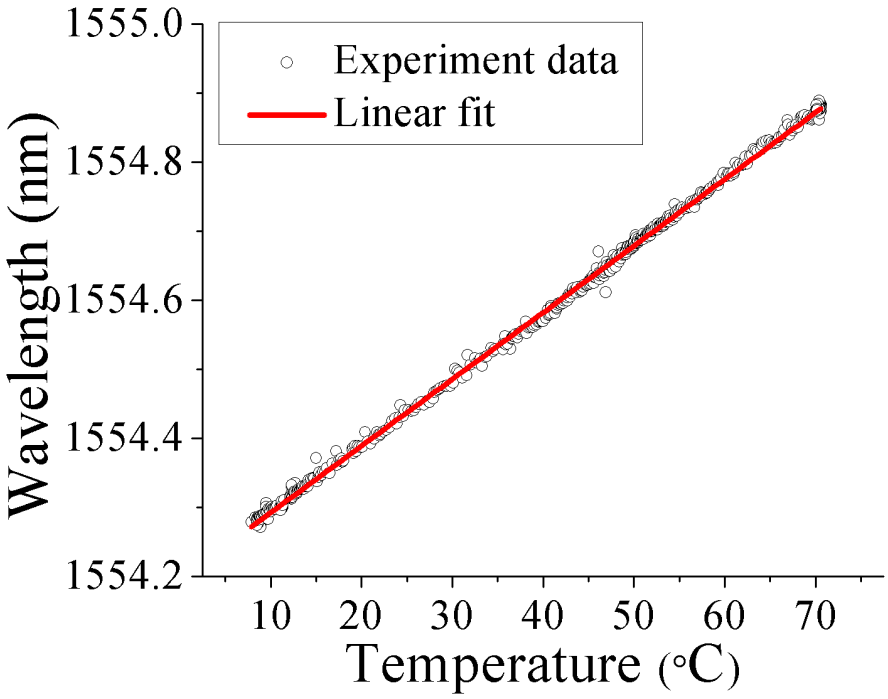

Fit.png

Figure 4-6: Linearity and sensitivity of the sensors [Courtesy of Xiaotian Zou]

Chapter 5

Experimental Results and Discussion

5.1 First Experimental Set

In this section, the temperature variation of 4”×8” concrete specimens during early-age hydration is presented and analyzed. A summary of peak temperature vs. time of concrete specimens with water-to-cement (w/c) ratios of 0.4, 0.5 and 0.6 is presented in Table 5.1. The measured concrete temperature will be used for other purposes such as concrete hydration heat; which will help us to develop a better understanding of cement hydration behavior (refer to Chapter 6).

Table 5.1: Peak temperature of 4”×8” concrete specimens

	FP		**Thermocouple**	
w/c	^oC	t (hr)	^oC	t (hr)
0.4	51.42	13.52	59.3	12.58
0.5	52.88	14.16	52.4	14.06
0.6	55.08	15.24	57.1	15.23

5.1.1 Results

When cement particles in contact with water, the hydration process begins and raises concrete temperature. Figures 5-1 to 5-6 illustrate temperature variation of concrete specimen during the early age of cement hydration with w/c ratios of 0.4, 0.5 and 0.6. Temperature development of concrete specimens were monitored for 70 hours immediately after concrete placement. In these figures, dashed curves are the temperature results measured by thermocouple sensor (reference sensor); continuous curves are the temperature profiles measured by FP fiber optic temperature sensor.

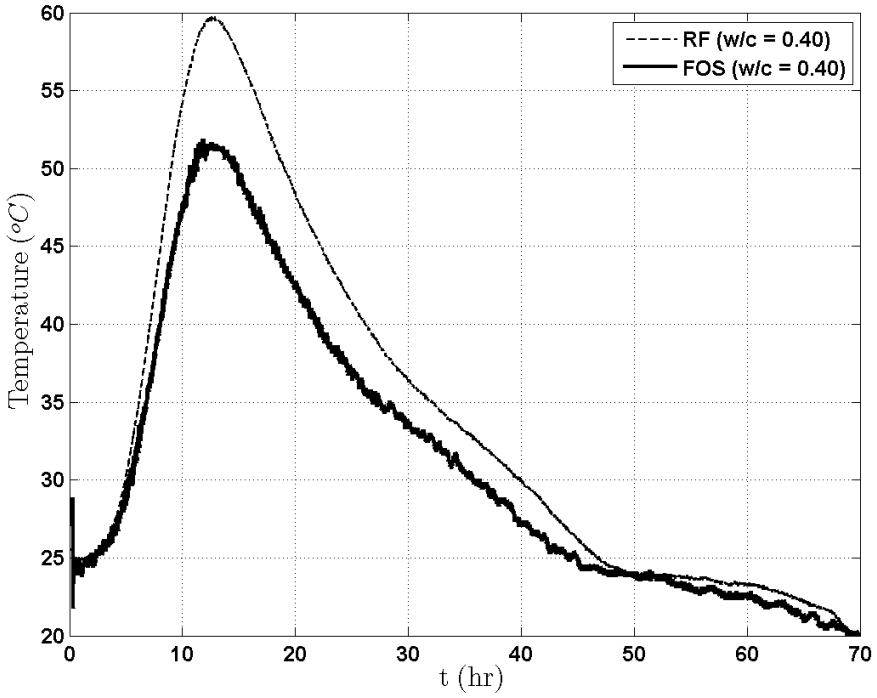

Figure 5-1: Concrete temperature at w/c = 0.4

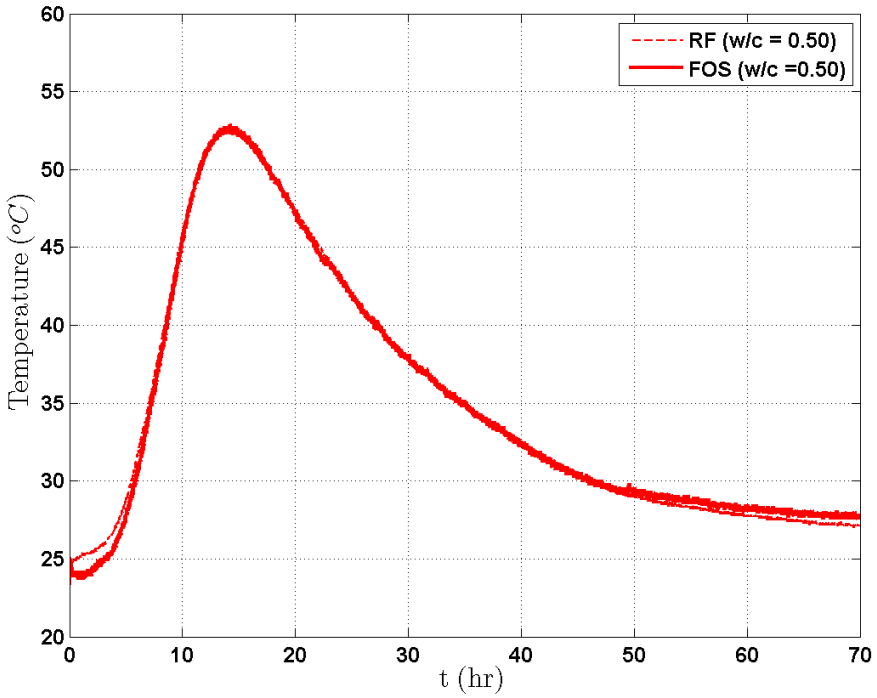

Figure 5-2: Concrete temperature at w/c = 0.5

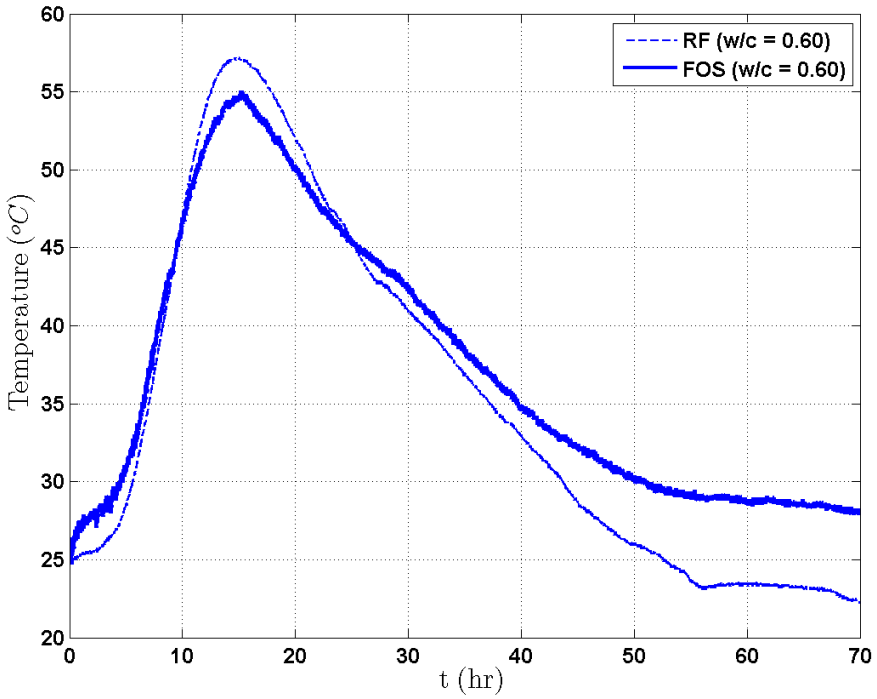

Figure 5-3: Concrete temperature at w/c = 0.6

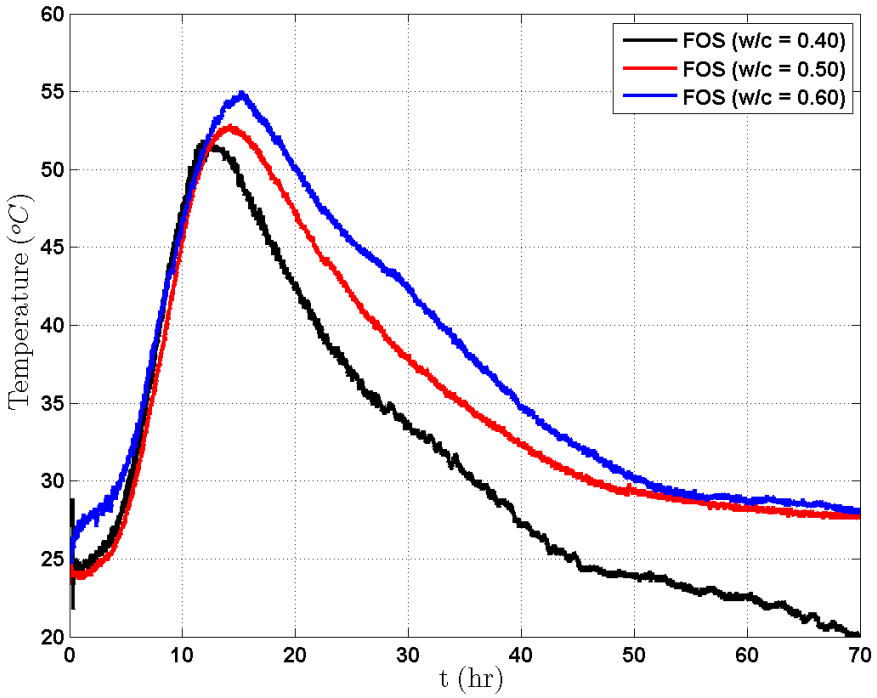

Figure 5-4: Concrete temperature with varying w/c by fiber optic temperature sensor

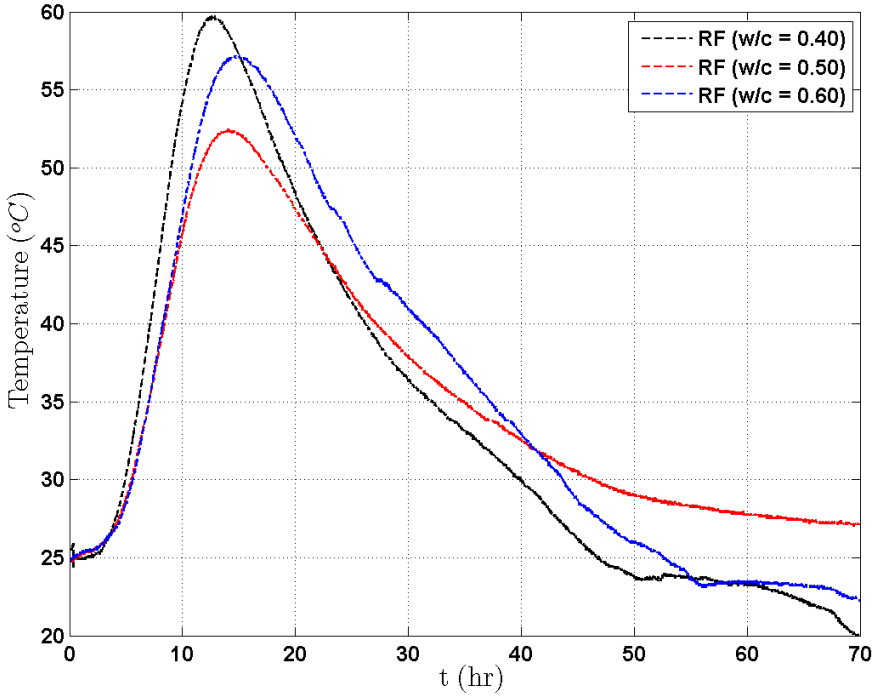

Figure 5-5: Concrete temperature with varying w/c by thermocouple sensor

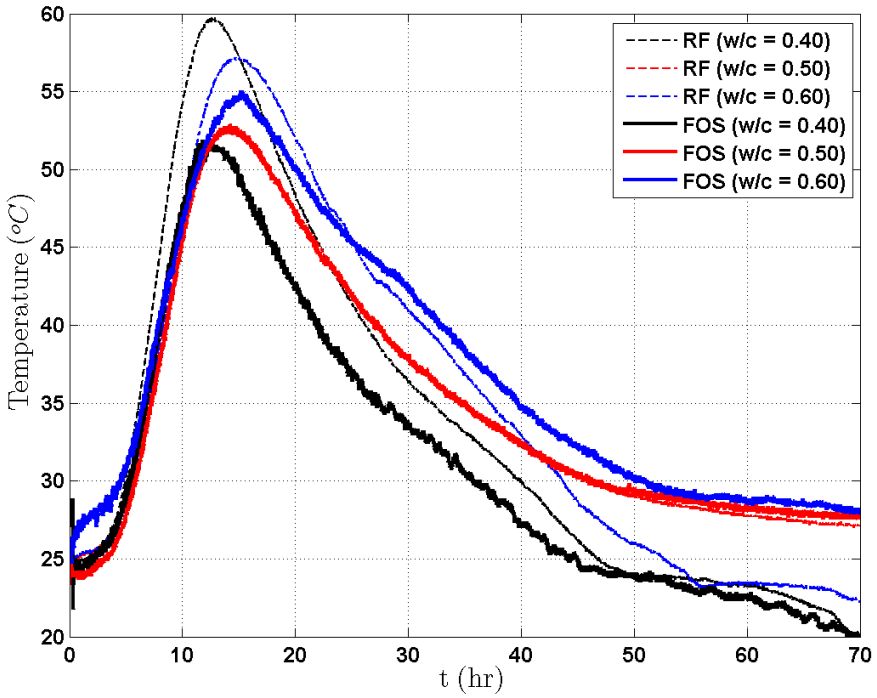

Figure 5-6: Concrete temperature with varying w/c by thermocouple and fiber optic temperature sensors

5.1.2 Discussion

In Figures 5-4 and 5-5, the temperature in each concrete specimen (with varying w/c ratios) increases at a higher rate during initial hydration until reaching its peak, then it decreases moderately for the last 30 hours and cools down slowly to reach steady state.

Temperature variation of concrete specimens measured by the FP fiber optic temperature sensor is shown in Figure 5-4. The measured peak temperature of concrete specimens with w/c ratios of 0.4, 0.5 and 0.6 were 51.42^oC, 52.88^oC, and 55.08^oC, corresponding to the final setting time of 13.52 hr, 14.16 hr and 15.2 hr after casting respectively. It should be noticed that, for concrete with equal mass of cement and sand but different water to cement ratios, the higher the ratio the faster the rate of cement hydration and higher potential temperature concrete can achieve. This is well agreed

with the finding in [19]. In addition, since the amount of cement, sand and gravel were kept fixed, each temperature curve behaved in a similar trend in term of temperature rising and decreasing. This was proven with theoretical result found in [15]. It was noticed that the specimen with a w/c ratio of 0.4 behaved differently during steady state compared to others (because its curve was much lower). This result mainly caused by environmental conditions. According to the thermometer, the average ambient temperatures during steady state of concrete experiments were 19.2 ^oC, 25.1 ^oC and 24.1 ^oC, corresponding to specimen with w/c ratios of 0.4, 0.5 and 0.6, respectively.

Temperature of concrete specimens measured by the thermocouple sensor is illustrated in Figure 5-5. The maximum temperature of concrete specimens with w/c ratios of 0.4, 0.5 and 0.6 were 59.3 ^oC, 52.4 ^oC and 57.1 ^oC, corresponding to final rising times of 12.58 hr, 14.06 hr and 15.23 hr after concrete placement respectively. Temperature profiles of specimens with w/c ratios of 0.5 and 0.6 generally followed same pattern, except that the w/c = 0.6 curve generated higher temperature values than the w/c = 0.5 curve. However, the temperature profile of w/c ratio 0.4 specimen is completely different. Theoretically, it should generate a lower temperature curve than w/c ratios of 0.5 and 0.6 when the amount of cement and sand were fixed, but it reached a much higher maximum temperature than others. This undesired result was caused by the sensing characteristic of thermocouple within concrete specimen which was observed to be easily interfered by the environment conditions.

Based on the analysis of temperature variation of the individual concrete specimen from Figures 5-1 to 5-3, the following findings are obtained:

1. In Figure 5-1 (w/c = 0.4), concrete temperature profiles measured by the FP sensor and the thermocouple sensor are not in a good agreement. Thermocouple has shown a higher temperature curve than the FP sensor. However, both sensors stayed at about the same condition during steady state. This is probably due to the thermocouple sensor experienced a high interference compared to FP sensor.

2. In Figure 5-2, both sensors produced a almost-perfect match with only a slight variation during the initial reading.

3. In Figure 5-3, the temperature curves of concrete specimen generated by FP and thermocouple sensors demonstrate a similar trend during the first 12 hours; later, the reference sensor generated a higher peak temperature and dropped at a faster rate than FP sensor. Again, this is possibly due to the same reason mentioned above.

5.2 Second Experimental Set

The temperature variation of 3”×6” concrete specimens during early-age will be presented and analyzed in the following subsections. A summary of peak temperature vs. time of concrete specimens measured by two FP fiber optic temperature sensors (where FP1 and FP2 were positioned at centroid and surface of concrete specimens respectively) with w/c ratios of 0.40, 0.45, 0.50, 0.55 and 0.60 are shown in Table 5.2. The measured concrete temperature will be used for parametric studies of concrete hydration heat (H(t)) and apparent activation energy (E_a); which will help us to develop a

better understanding of cement hydration behavior (refer to Chapter 6).

Table 5.2: Peak temperature of 3”×6” concrete specimens at surface and centroid

water-cement ratio		0.40	0.45	0.50	0.55	0.60
Surface (FP2)	^oC	35.51	36.11	36.74	37.44	37.82
	Time (hr)	14.60	13.68	13.66	14.83	14.30
Core (FP1)	^oC	37.89	39.19	40.37	41.08	43.49
	Time (hr)	14.18	13.55	12.96	14.68	13.92

Table 5.3: Maximum temperature difference between centroid and surface of 3”×6” concrete specimens

w/c	0.40	0.45	0.50	0.55	0.60
$\Delta T_{cs}(^oC)$	2.6	3.0	3.70	4.40	5.68

5.2.1 Results

The results of 3”×6” concrete tests consist of the following:

- Figures 5-7 to 5-11 show the temperature development of each concrete specimen measured at core (continuous curve) and surface (dash curve). Ambient temperature (dot curve) within the glass chamber was also measured.

- Figures 5-12 and 5-13 show surface temperature and core temperature profiles of concrete specimen with varying w/c ratios (0.40 - 0.60 with 0.05 increment), respectively.

- Figure 5-14 illustrates the temperature difference between the temperature measured at core and surface of concrete specimens.

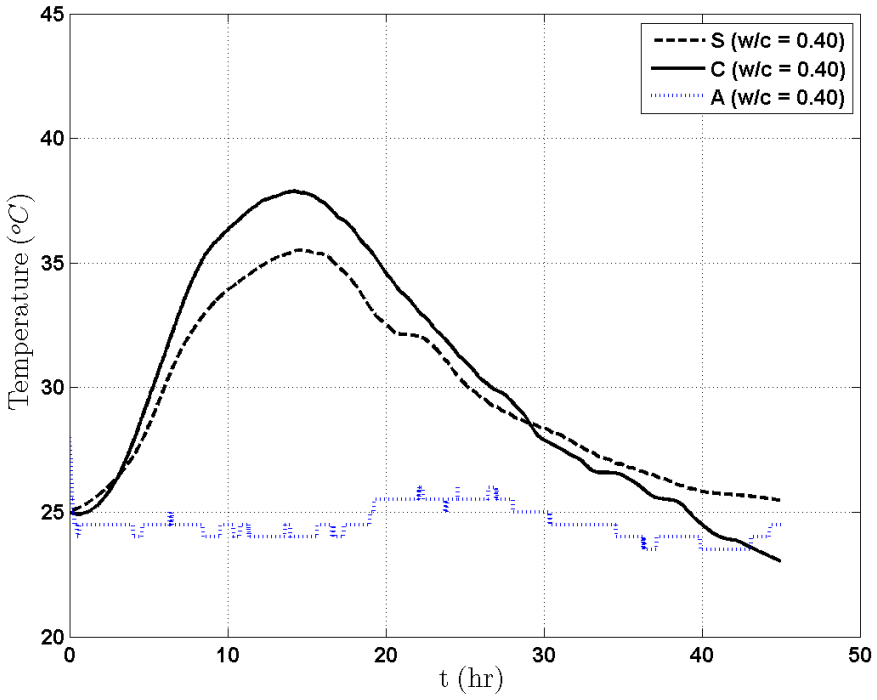

Figure 5-7: Surface and core temperature profiles of 3”×6” concrete specimen (w/c = 0.40)

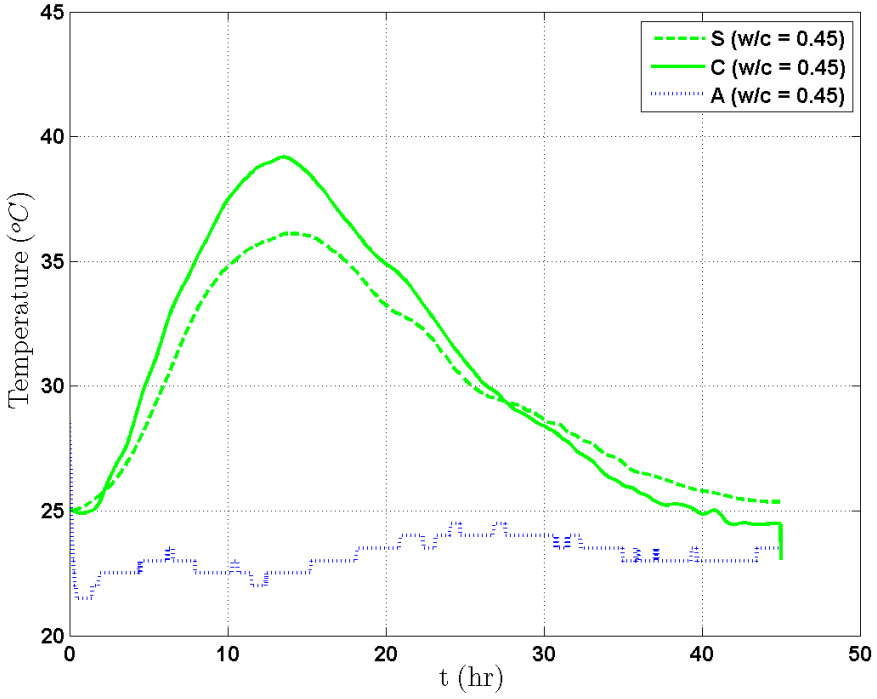

Figure 5-8: Surface and core temperature profiles of 3”×6” concrete specimen (w/c = 0.45)

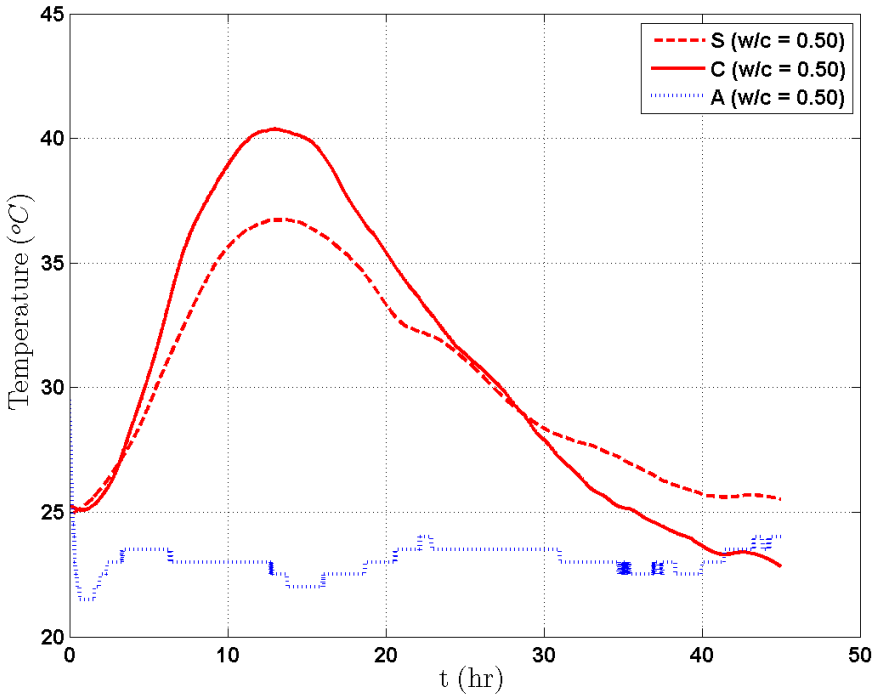

Figure 5-9: Surface and core temperature profiles of 3”×6” concrete specimen (w/c = 0.50)

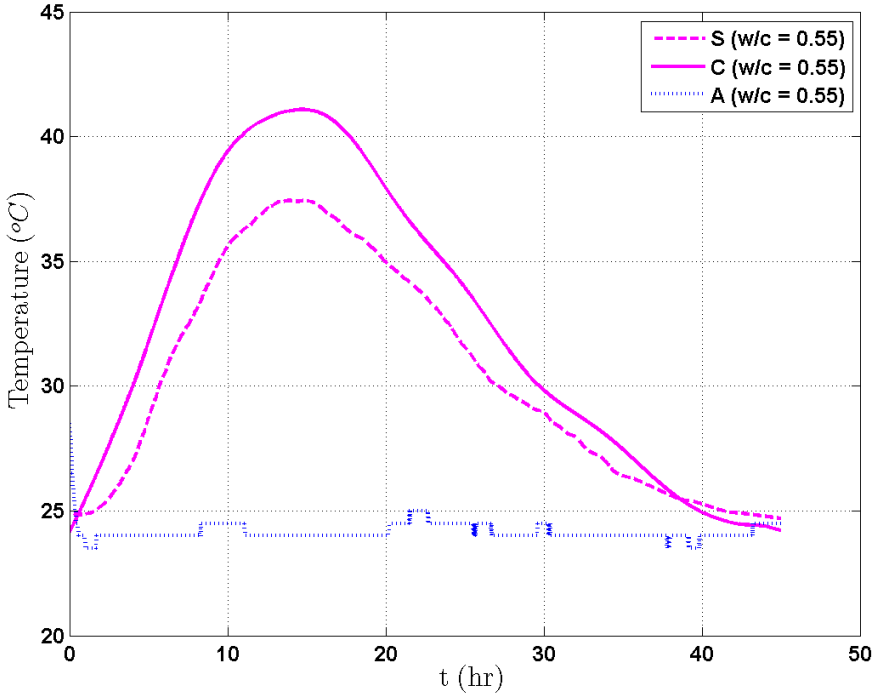

Figure 5-10: Surface and core temperature profiles of 3”×6” concrete specimen (w/c = 0.55)

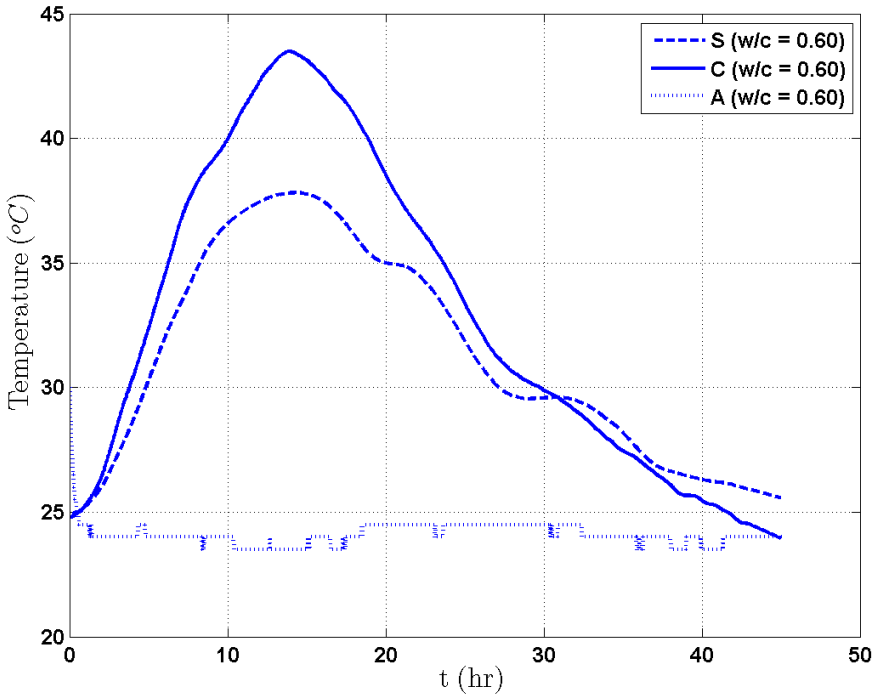

Figure 5-11: Surface and core temperature profiles of 3”×6” concrete specimen (w/c = 0.60)

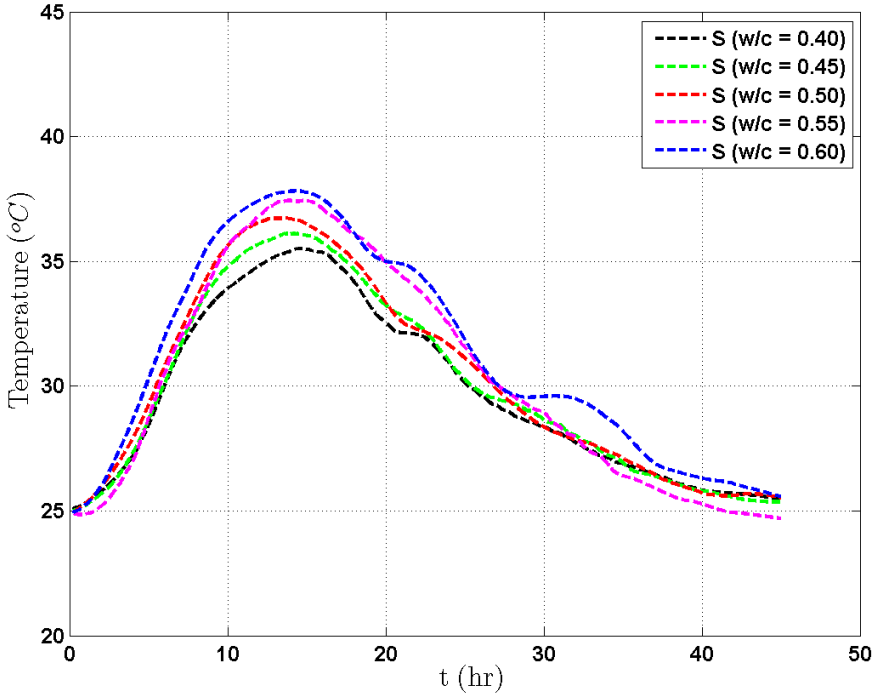

Figure 5-12: Surface temperature profiles of 3”×6” concrete specimen (w/c = 0.40 - 0.6)

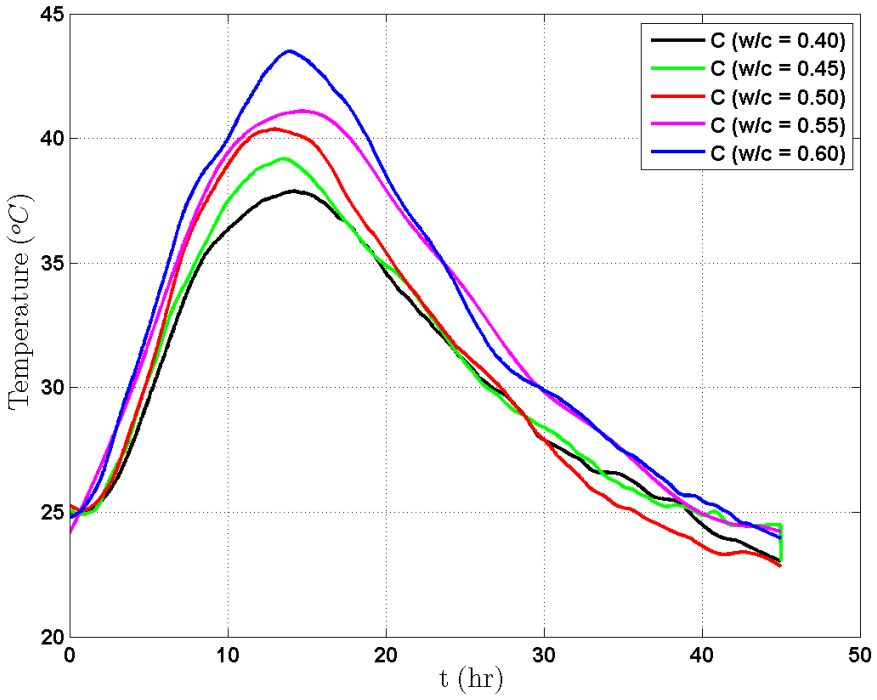

Figure 5-13: Core temperature profiles of 3”×6” concrete specimen (w/c = 0.40 - 0.6)

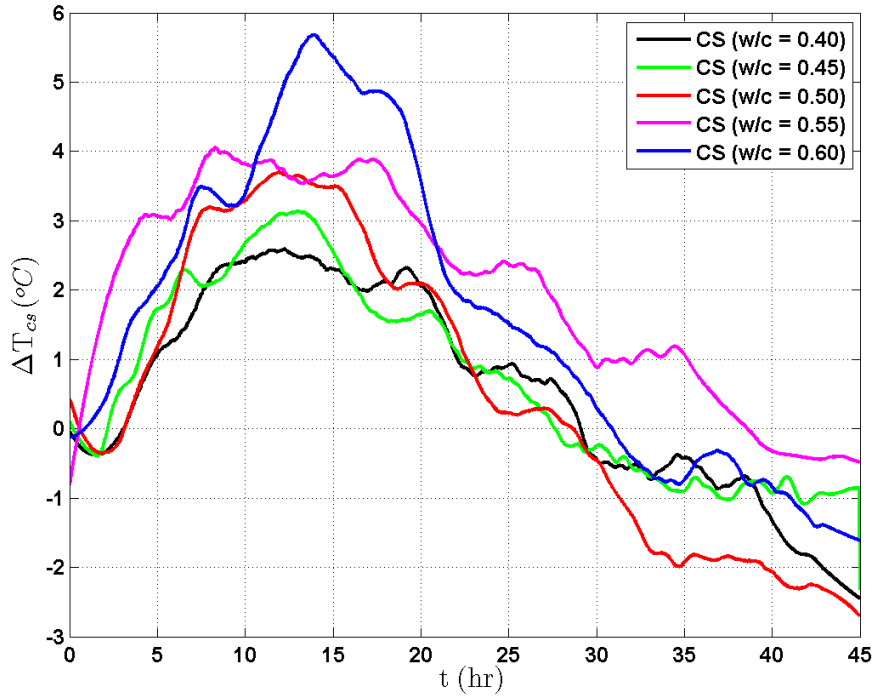

Figure 5-14: Temperature difference between surface and core temperature (w/c = 0.40 - 0.60)

5.2.2 Discussion

Temperature development for concrete specimens with w/c ratios of 0.40, 0.45, 0.50, 0.55 and 0.60 is discussed in the following:

- The peak temperatures of concrete specimens measured at surface are 35.51 (w/c = 0.40), 36.11 (w/c = 0.45), 36.74 (w/c = 0.50), 37.44 (w/c = 0.55) and 37.82 (w/c = 0.60), respectively. And the peak temperatures measured at the center of each concrete specimen are 37.89 (w/c = 0.40), 39.19 (w/c = 0.45), 40.37 (w/c = 0.50), 41.78 (w/c = 0.55) and 43.49 (w/c = 0.60), respectively.

- The amount of cement, sand, and gravel were kept constant but different w/c ratios were used. It should be noticed that each specimen consisted of equal mass of dry materials. The use of higher w/c leads to higher maximum temperatures for both temperatures measured at the surface and the core of a concrete specimen (refer to Figures 5-12 and 5-13).

- In Figure 5-12, each surface temperature profile behaves very similar during the first 20 hours. Concrete specimen consists of higher w/c ratios most likely produced an overall higher temperature curve than the specimen with lower w/c ratios. In the initial stage of concrete hydration, each concrete specimen generated a rapid temperature development with a steep positive slope. The maximum temperatures achieved between 13.6th and 14.6th hours after concrete placement. When the first 20 hours passed, surface temperature did not decrease smoothly. Each temperature curve showed a few hills during the cooling period. This fluctuation was mainly affected by ambient conditions within the glass chamber which

prevented the temperature to gradually decrease during the deceleration period of hydration . Finally, all surface temperature curves approached the ambient temperature.

- In Figure 5-13, temperature profiles measured at the core show a higher temperature rising rate immediately after concrete placement. This rapid temperature development was primarily due to the heat of hydration. The potential temperature occurred the earliest approximately at 13.5th hours and the latest at 14.7th hours. After each temperature curve reaching its maximum, the temperature started decreasing at a moderate rate during the cooling period.

- By comparing individual surface temperature curve with ambient temperature, the following relationship were observed:

  - In Figures 5-7 to 5-11, after 20 hours the behavior of surface temperatures were dominated by ambient temperature. Few constant slopes (which look like a flat hill) were observed. If look closely, we can see that the ambient temperature stayed constant for several hours during the constant slope period. The constant slope of surface temperature was induced by ambient temperature. The reason that the slope of surface temperature did not stay constant for the entire period after 20 hours because the hydration process continuously occurs at a decreasing rate which against the effect of ambient temperature.

- Looking closely at the results of surface and core temperature profiles for each

concrete specimen from Figures 5-7 to 5-11, the following observations were obtained:

- Core and surface temperatures generated very similar profile before the presence of crossover effect, except the core temperature produced a higher temperature curve than the surface temperature. This is because the concrete surface was exposed to the environment. As a result, the heat at the surface can easily escape to the environment than the heat at the core. It should be noticed that, after reaching peak temperature, both surface and core temperatures started approaching each other which lead to the intersection between two curves. This break-even-point represents the equilibrium temperature between the surface and the core.
- Later, the core temperature dropped at a faster rate than the surface temperature during the deceleration period.
- During the last few hours before the end of the experiment, the core temperature went lower than the ambient temperature. This bizarre outcome is not yet completely understood. In general, concrete temperature should cool down to the ambient temperature, but it should not go lower than the ambient temperature. Possible explanations are provided in the following.
    * The copper tube installed at the center of the cylinder mold and was fixed at the bottom. In addition, the fixed end was installed against a 2 inch thick styrofoam (Figure 3-7). As a result, there was only one opening for the heat of hydration to flow in or out of the concrete spec-

imen. When the hydration heat dissipated from a concrete specimen into the environment during the hydration acceleration stages, the generator sucks the air from both inside and outside of the glass chamber to maintain a uniform temperature distribution within the glass chamber. When the air was circulating inside the chamber, the air flow hit some boundaries such as the top horizontal and vertical surfaces of the styrofoam chamber at an angle (Figure 5-15). Therefore, the core temperature was less likely affected by the ambient temperature.

  - It is possible that the atmospheric pressure within the glass chamber was higher than the pressure at the core of the concrete specimen. Therefore, core temperature becomes lower than ambient temperature.
  - Another possibility is that the concrete specimen acted like a refrigerator where the inside was cold and the outside was warm. This means that the core of concrete stores heat instead of releasing heat. More experiments are needed to confirm this possibility.

- In Figure 5-14, a series of curves show the temperature difference between the core and surface temperatures from 0 to 45 hours. When the curve is above x-axis, the core temperature is higher than the surface temperature, but when the curve is below x-axis, the surface temperature is higher than the core temperature. The maximum temperature difference increases with higher w/c ratios (Table 5.3).

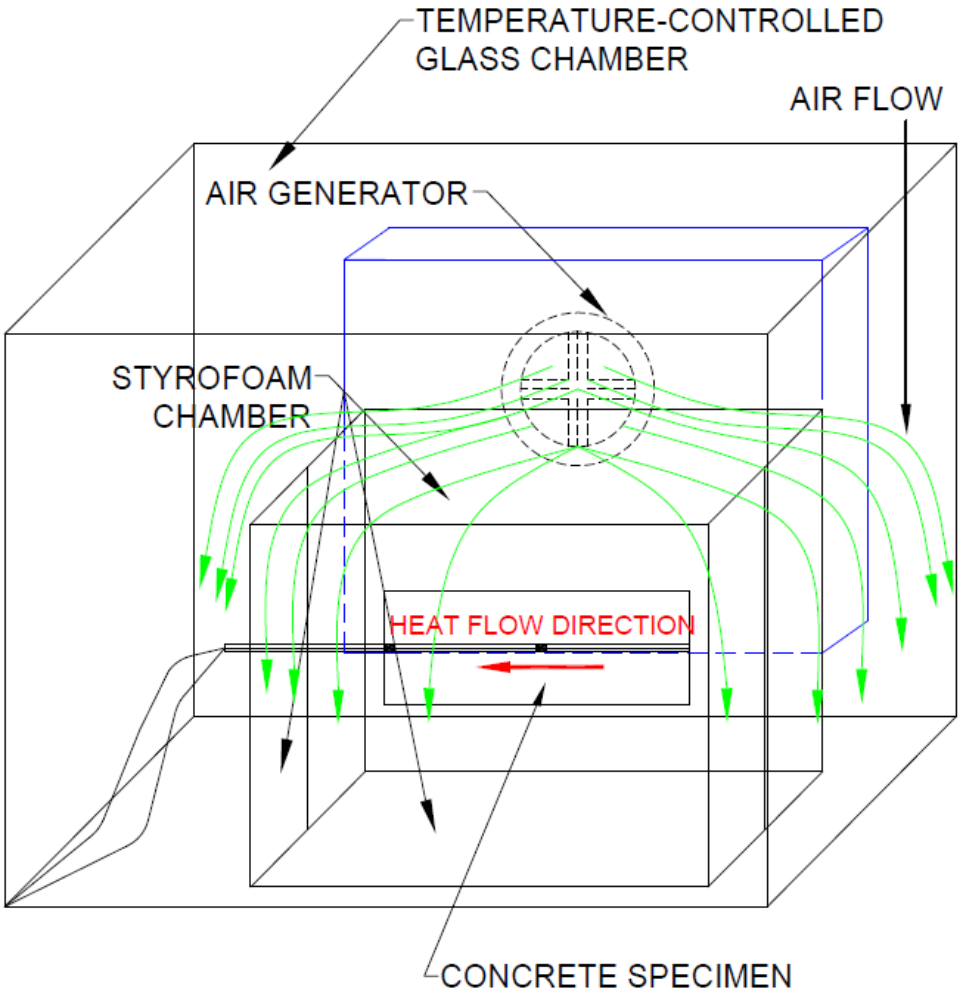

Figure 5-15: Air directions inside the glass chamber

5.3 Summary

- When equal mass of cement, sand, and gravel were used, the maximum temperature increase with the increased of water-to-cement ratios. This was found in both experimental sets.

- In experimental set No.1, the thermocouple sensor produced inaccurate temperature measurement. The Fabry-Perot fiber optic temperature sensor generated reliable data. The temperature development within concrete cylinders was increased primarily due to the heat of hydration and decreased due to ambient conditions

during the cooling period.

- In experimental set No.2, after 20 hours of concrete placement, the development of surface temperature was mostly dominated by the ambient temperature inside the glass chamber. However, the core temperature was less effected by the ambient temperature. The crossover effect occurred between the surface and core temperature curves since both temperatures are trying to reach a point of equilibrium.

- The fact that the core temperature went lower than the ambient temperature is not yet completely understood. More research is needed in the future.

Chapter 6

Theoretical Models for the Prediction of Hydration Heat

Two approaches were used to perform a parametric study on the temperature data obtained from both experimental sets: (a) the first approach is used for calculating apparent activation energy and heat of hydration. The apparent activation energy is a function of degree of hydration (α) and concrete temperature (T_c). The heat of hydration depends on concrete specific heat (C_p) and concrete temperature (T_c). (b) the second approach is used for the calculation of heat of hydration (H(t)). This approach is based on time equivalent, apparent activation energy (assumed to be 29,000 J/mol and 33,500 J/mol), hydration parameters (calculated) and concrete temperature (obtained from experiments). Two values of E_a are selected in order to obtain a range of heat evolution within concrete structure. E_a equals to 29,000 J/mol is chosen because the minimum value of E_a determined in the first approach is around 29,000 J/mol. Refer to Chapter 2 for the selection of E_a equals to 33,500 J/mol. A summary of parametric

studies in this chapter is illustrated in Figure 6-1.

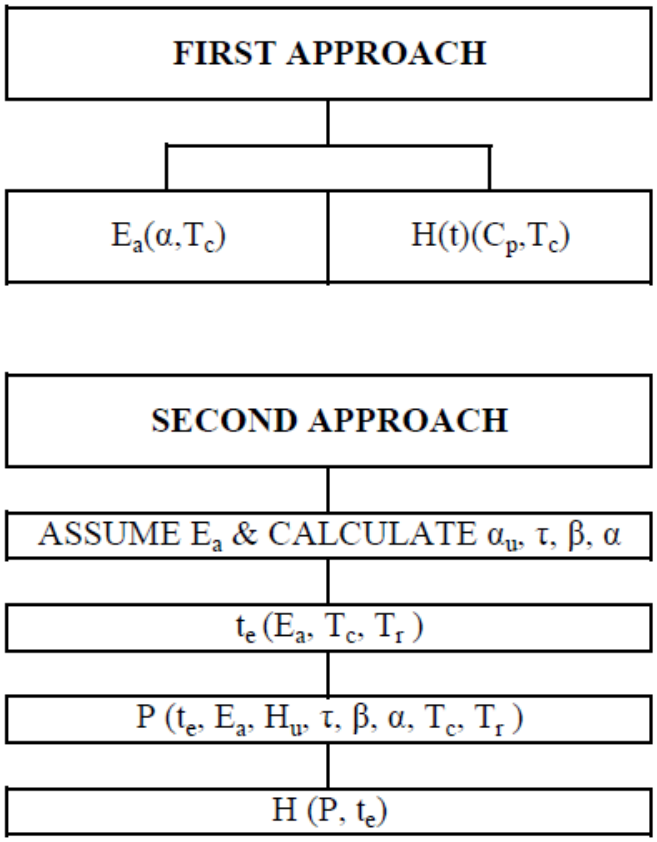

Figure 6-1: Parametric studies of apparent activation energy and heat of hydration.

6.1 Apparent Activation Energy and Heat of Hydration Models - First Approach

Activation energy is known as an energy required to overcome the hydration reaction between water and cement particles. Activation energy can also be considered as the most common parameter in the prediction of temperature sensitivity for hydrated products [20]. Since concrete is heterogeneous and composed of many different chemical components, the activation energy of concrete should be called as the apparent activa-

tion energy (E_a) [39]. E_a can be calculated as shown in Eq. 6.1 [39]:

$$E_a = (44.92 - 0.043T_c)\, exp\,(-0.00017T_c - \alpha) \tag{6.1}$$

where, E_a: Apparent activation energy (kJ/mol),

T_c: Concrete temperature at instant time (^oK),

α: Degree of hydration (DOH) at instant time (dimension less)

DOH equals to the ratio of heat of hydration H(t) to ultimate heat H_u as follow:

$$\alpha = \frac{H(t)}{H_u} \tag{6.2}$$

The ultimate heat H_u depends on cement chemical composition, the amount and type of supplementary cementing materials($SCMs$). H_u can be determined from Eq. 6.3 [40].

$$H_u = H_{cem} \cdot P_{cem} + 461P_{slag} + 1800P_{FA-CaO} \cdot P_{FA} \tag{6.3}$$

where, H_{cem}: cement hydration heat (kJ/kg)

P_{cem}: the mass ratio of cement over total cementitious content

P_{slag}: the mass ratio of slag over total cementitious content,

P_{FA-CaO}: the mass ratio of fly ash CaO to cementitious content.

The cement hydration heat (H_{cem}) is a function of cement chemical composition and can be calculated by Eq. 6.5 [40]:

$$H_{cem} = 500P_{C_3S} + 260P_{C_2S} + 866P_{C_3A} + 420P_{C_4AF} + 624P_{SO_3} + \tag{6.4}$$

$$1186P_{FreeCa} + 850P_{MgO}$$

where P_n: the mass ratio of ”n” component over the total cement content.

The heat of hydration H(t) depends on concrete specific heat and concrete temperature development and can be determined from Eq. 6.5 [27]:

$$H(t) = C_p \times T_c \tag{6.5}$$

where, H(t): heat of hydration at time t (kJ/kg)

C_p: average concrete specific heat ($0.96 kJ/kg/^oC$)

T_c: concrete temperature (^oC)

When taking the first derivative of Eq.6.1 and Eq.6.5 with respect to concrete temperature, the following equations can be obtained:

$$\frac{dE_a}{dT_c} = \left[-0.043 + (44.92 - 0.043T_c)\left(-0.00017 - \frac{C_p}{H_u}\right)\right] \times exp\left(-0.00017T_c - \frac{C_p}{H_u}\right) \tag{6.6}$$

$$\frac{dH}{dT_c} = C_p \tag{6.7}$$

By taking the ratio between the first derivative of E_a and H(t), a constant value is obtained as shown in Eq. 6.8.

$$\left(\frac{dE_a}{dT_c}\right)\left(\frac{dH}{dT_c}\right)^{-1} = -0.0448 \tag{6.8}$$

According to Eq. 6.8, the relationship between hydration heat and apparent activation energy is linear (with a negative slope). This indicates that E_a decreases with the increase of hydration heat.

6.2 Heat of Hydration Models - Second Approach

The hydration heat plays a crucial role in both short-term and long-term performance of concrete structures. Therefore, it is very important to have a good understanding of concrete hydration behavior. The hydration heat parameters, τ, β, and α_u can be determined in Eq. 6.10 to 6.11 [28].

$$\tau = 66.78 \cdot P_{C_3A}{}^{-0.154} \cdot P_{C_3S}{}^{-0.401} \cdot Blaine^{-0.804} \cdot P_{SO_3}{}^{-0.758} \cdot \exp(2.187 \cdot P_{SLAG} + 9.50 \cdot P_{FA} \cdot P_{FA-CaO}) \tag{6.9}$$

$$\beta = 181.4 \cdot P_{C_3A}{}^{0.146} \cdot P_{C_3S}{}^{0.227} \cdot Blaine^{-0.535} \cdot P_{SO_3}{}^{0.558} \cdot \exp(-0.647 \cdot P_{SLAG}) \tag{6.10}$$

$$\alpha_u = \frac{1.031 \cdot w/cm}{0.194 + w/cm} + 0.5 \cdot P_{FA} + 0.3 \cdot P_{SLAG} \leq 1.0 \tag{6.11}$$

With the assumed values of E_a and calculated hydration parameters, rate of concrete hydration heat can be determined from the widely known Arrhenius method which is based on maturity concept and exponential degree of hydration as determined by Eq. 6.12 [24]:

$$P(t) = H_u \times \left(\frac{\tau}{t_e}\right)^{\beta} \times \alpha_u \times exp\left[-\frac{\tau}{t_e}\right]^{\beta} \times exp\left[\frac{E_a}{R}\left(\frac{1}{T_r} - \frac{1}{T_c}\right)\right] \tag{6.12}$$

where, P(t): rate of concrete hydration heat ($J/g/hr$)

T_r: reference temperature (294.25 ^oK)

T_c: concrete temperature (^oK)

t_e: as defined in Eq. 6.13

$$t_e = \sum exp\left(\frac{-E_a}{R}\right)\left(\frac{1}{T_c} - \frac{1}{T_r}\right) \cdot \Delta t \tag{6.13}$$

where, t_e is equivalent age (hr)

T_c is concrete temperature (^oK)

T_r is reference temperature (294.25^oK)

E_a is the apparent activation energy (J/mol)

R is the universal gas constant (8.3144J/mol/^oK)

The ultimate heat H_u and the cement hydration heat H_{cem} can be determined from Eqs. 6.3 and 6.5 [40].

With the calculated value of P(t), concrete hydration heat H(t) (kJ/kg) can be obtained by:

$$H(t) = P(t) \times \Delta t_e \tag{6.14}$$

6.3 Results and Discussion for 4inch-by-8inch Concrete Specimens - First Approach

6.3.1 Calculated Apparent Activation Energy (4inch-by-8inch)

Calculated apparent activation energy (E_a) is illustrated in Figure 6-2. The curves were calculated based on the temperature measured by the FP fiber optic sensor. The temperature measured by the thermocouple sensor is neglected in the calculation of E_a since the data is not reliable. A list of maximum and minimum E_a values of concrete specimens are summarized in Table 6.1.

Table 6.1: Calculated apparent activation energy for 4"×8" concrete specimens

	water-cement ratio		
E_a (kJ/mol)	0.40	0.50	0.60
Min	29.274	29.230	29.129
Max	30.751	30.590	30.60

Based on the results shown in Table 6.1:

1. All specimens have similar values of $(E_a)_{min}$ and $(E_a)_{max}$. Average minimum and maximum values of E_a for each specimen are to 29.21 kJ/mol and 30.65 kJ/mol, respectively.

2. The above values is in an acceptable range compared to the values reported by other researchers [39, 26].

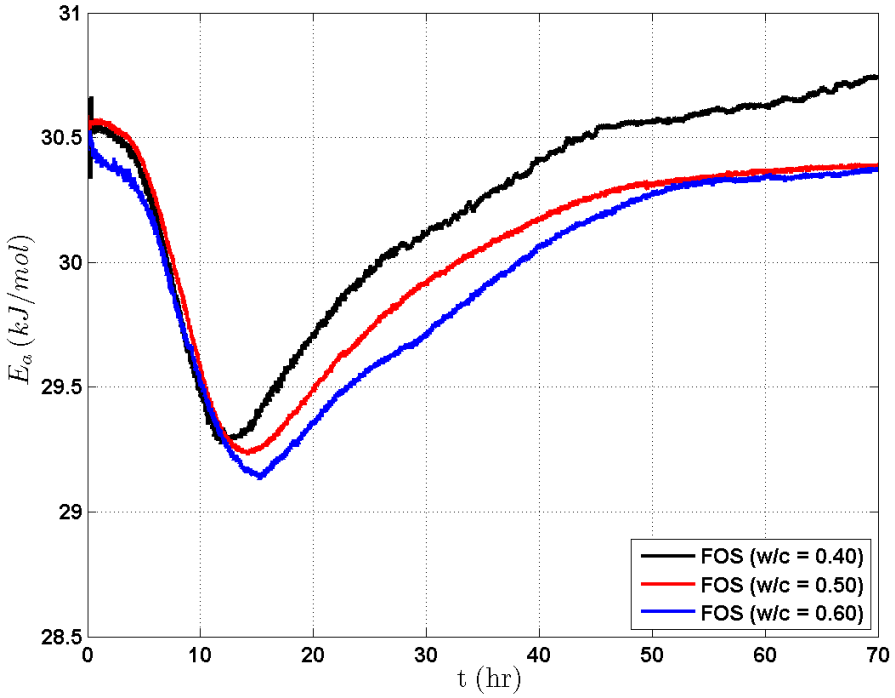

Figure 6-2: Apparent activation energy of 4"×8" concrete cylinders for w/c of 0.4, 0.5 and 0.6 (FP sensor)

In Figure 6-2, E_a have profiles like the reflection of temperature curves. The apparent activation energy started with a high value, decreased until it reached its minimum, started increasing with a moderate rate, and gradually approached steady state. It is observed that with w/c ratios increasing from low to high, more energy is required to give up in order to overcome the reaction between water and cement (1.1182 kJ/mol (w/c = 0.40), 1.129 kJ/mol (w/c = 0.50) and 1.471 kJ/mol (w/c = 0.60)). Also, the energy curve for specimen with w/c = 0.40 went up much higher than the other curves after it passed its minimum (refer to Chapter 5 for detailed explanation). In addition, the minimum and maximum values of E_a for each concrete specimen are slightly different

from each other as shown in Table 6.1.

6.3.2 Calculated Heat of Hydration (4inch-by-8inch)

In this section, the calculated heat of hydration for concrete specimens with w/c ratios of 0.40, 0.50 and 0.60 are illustrated in Figure 6-3. The curves were calculated based on temperature measured by the FP fiber optic temperature sensor (where curves in black, red and blue are for specimen with w/c of 0.40, 0.50, and 0.60, respectively). Again, temperature data obtained from the thermocouple sensor is neglected in this analysis. A summary of maximum values of hydration heat for concrete specimens are presented in Table 6.2.

Table 6.2: Calculated heat of hydration for 4"×8" concrete specimens

	water-cement ratio		
Heat (kJ/kg)	0.40	0.50	0.60
H_{max}	49.832	50.769	52.887

According to Table 6.2, hydration heat values for specimens have a range from 49.83 kJ/kg to 52.887 kJ/kg. This indicates that higher w/c ratios can generate higher hydration heat (Figure 6-3).

6.3.3 Relationship between Heat of Hydration and Apparent Activation Energy (4inch-by-8inch)

In Figure 6-4, linear lines demonstrate the relation between hydration heat and E_a of concrete cylinders with respect to the temperature measured by the FP fiber optic tem-

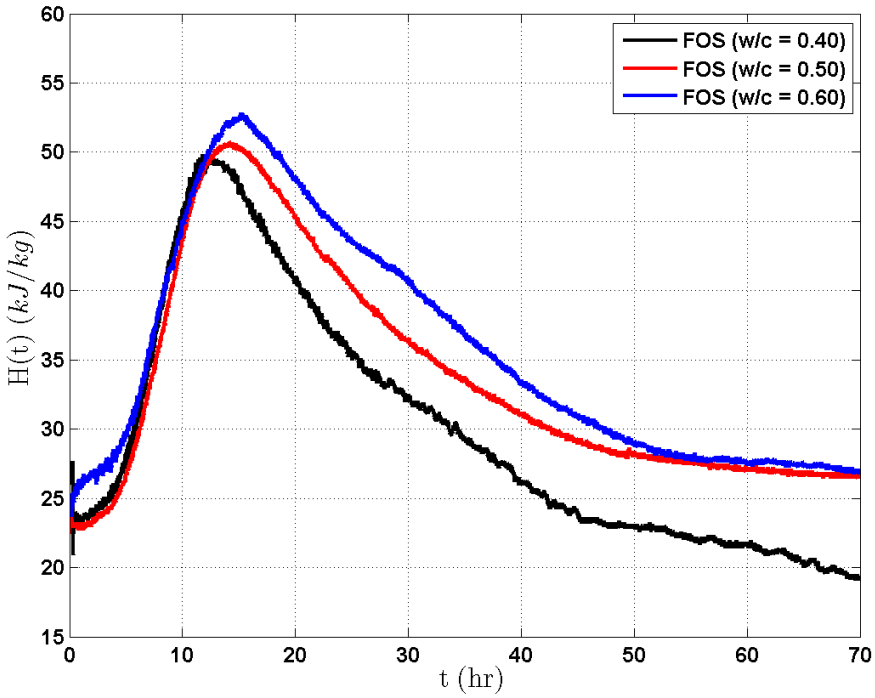

Figure 6-3: Heat of hydration of 4”×8” concrete cylinders for w/c of 0.4, 0.5 and 0.6 (FP sensor)

perature sensor. It is interesting to see that the curve with lower w/c ratios start earlier than specimens with higher w/c ratios. This is because higher energy is required, leading to the delayed of concrete hydration [40]. The result also shows that each specimen exhibits identical relationship between E_a and H(t). This result agrees with Eq. 6.8 and reference [39].

6.4 Results and Discussion for 4inch-by-8inch Concrete Specimens - Second Approach

In this section, the calculated heat of hydration of 4”×8” concrete cylinders based on E_a equals to 29,000 J/mol and 33,500 J/mol and the temperature data obtained from the

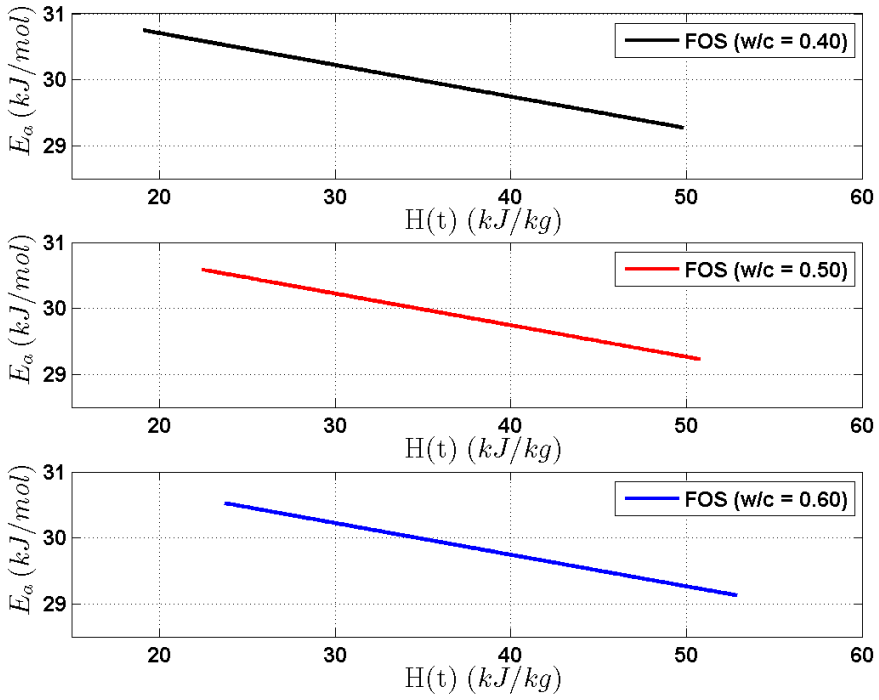

Figure 6-4: H(t) vs. E_a of 4"×8" concrete cylinders for w/c of 0.40, 0.50 and 0.60 (FP sensor)

FP fiber optic temperature sensor is presented and discussed in detail.

6.4.1 Concrete Equivalent Age (t_e) (4inch-by-8inch)

Calculated concrete equivalent age (t_e) based on E_a equals to 29,000 J/mol and 33,500 J/mol are shown in Figure 6-5 and 6-6, respectively. Both figures indicate that t_e of concrete specimen increases when w/c increases. In addition, values of t_e are primarily affected by E_a and concrete temperature (T_c). Higher values of t_e for each specimen can be obtained when the value of E_a increases, given that the same temperature data is used in calculation.

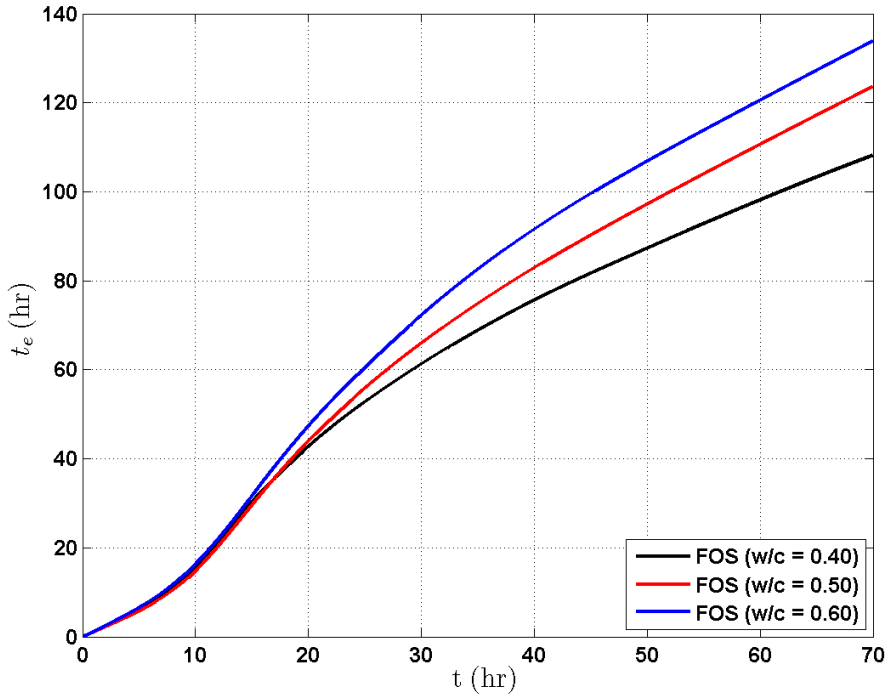

Figure 6-5: Time equivalent vs. real time of 4"×8" concrete cylinders with E_a = 29,000 J/mol (w/c = 0.40 - 0.60)

6.4.2 Calculated Heat of Hydration (4inch-by-8inch)

Heat of hydration profiles of 4"×8" concrete cylinders are presented in Figures 6-7 (E_a = 29,000 J/mol) and 6-8 (E_a = 33,500 J/mol). Heat of hydration generated rapidly and fluctuation was found in all heat of hydration curves. This is due to the large amount of C_3S (56.9%) presents in the typical Type I cement [29]. After reaching the peak heat of hydration, the heat within concrete specimens started decreasing rapidly for a duration of approximately 30 hours ($E_a = 29,000 J/mol$) and 35 hours ($E_a = 33,500 J/mol$) (Figures 6-7 and 6-8). It approached steady state at slower rate during the remaining period. As seen in Figures 6-7 and 6-8 heat of hydration generated by each specimen increases from lower to higher w/c ratios. The average maximum heat of hydration generated by all specimens is approximately 55 kJ/kg ($E_a = 29,000 J/mol$) and 70.4

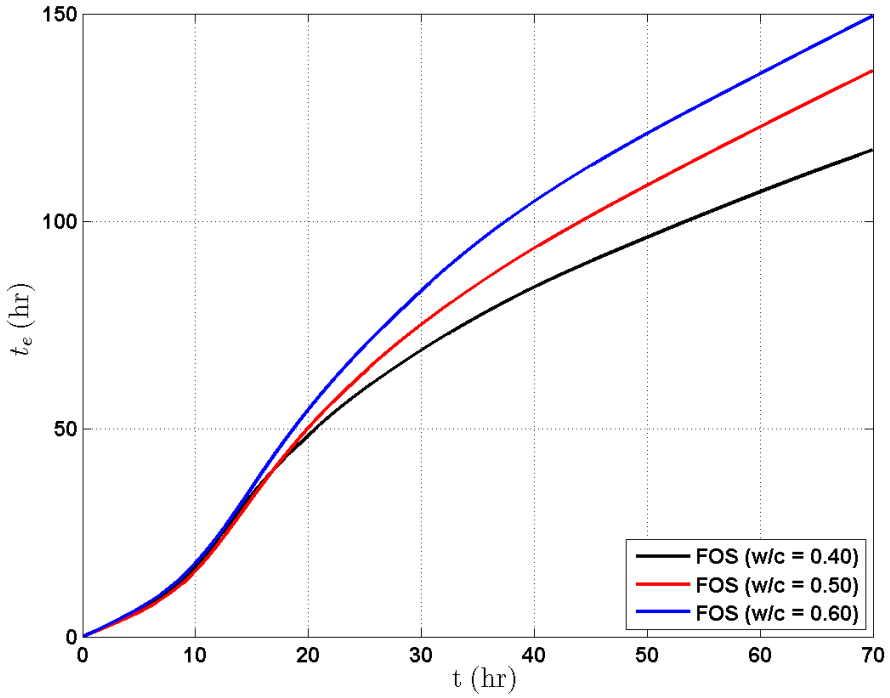

Figure 6-6: Time equivalent vs. real time of 4”×8” concrete cylinders with E_a = 33,500 J/mol (w/c = 0.40 - 0.60)

kJ/kg ($E_a = 33,500 J/mol$).

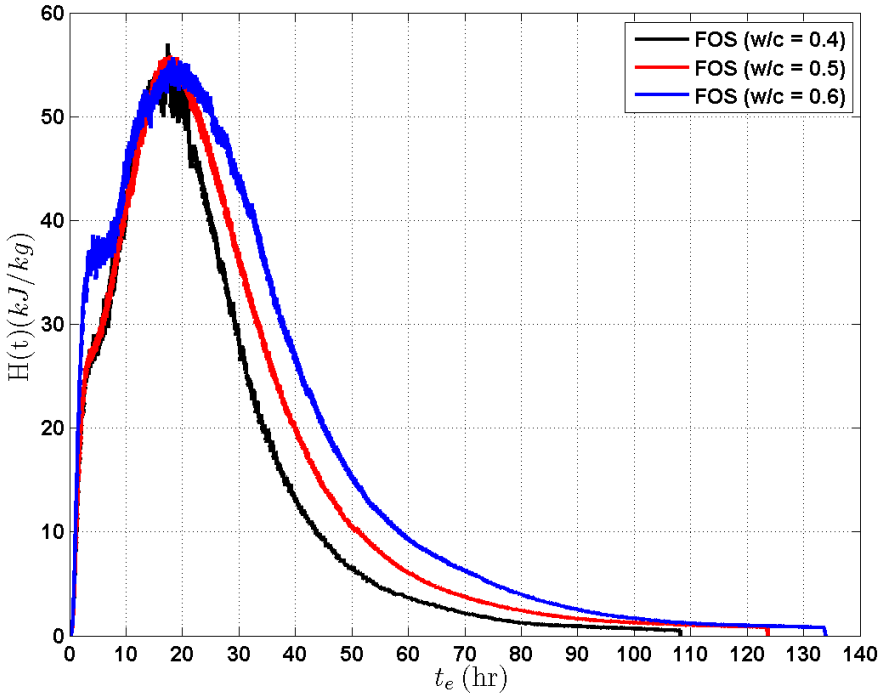

Figure 6-7: Heat of hydration of 4"×8" concrete specimen with E_a = 29,000 J/mol (w/c = 0.40 - 0.60)

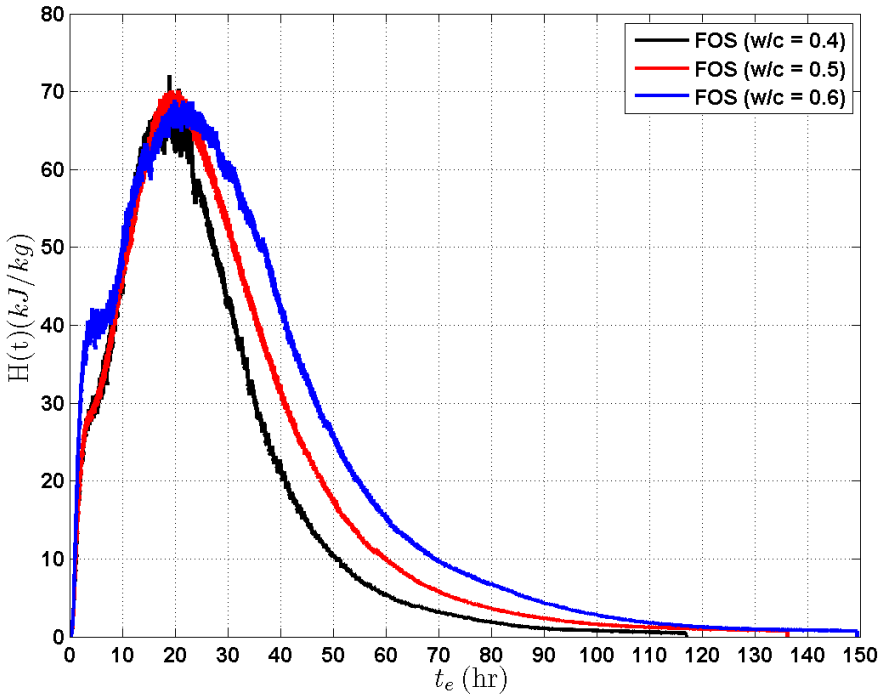

Figure 6-8: Heat of hydration of 4"×8" concrete cylinders with E_a = 33,500 J/mol (w/c = 0.40 - 0.60)

6.5 Results and Discussion for 3inch-by-6inch Concrete Specimens - First Approach

6.5.1 Calculated Apparent Activation Energy (3inch-by-6inch)

Values of minimum and maximum E_a for five concrete specimens are summarized in Tables 6.3 and 6.4. According to the results in Tables 6.3 and 6.4 the following results are found.

1. Minimum and maximum values of E_a calculated based on surface temperature for each specimen are approximately 29.97 kJ/mol and 30.52 kJ/mol.

2. Minimum and maximum values of E_a calculated based on core temperature for each specimen are approximately 29.8 kJ/mol and 30.63 kJ/mol.

3. The above values are in good agreements with other findings [26, 39].

4. Values of $(E_a)_{min}$ at surface and at core of each concrete specimen can be considered to be identical. Similarly, $(E_a)_{max}$ for all five specimens calculated based on surface and core temperatures are very close.

Table 6.3: Calculated apparent activation energy for 3"×6" concrete specimens (at surface)

	water-cement ratio				
E_a (kJ/mol)	0.40	0.45	0.50	0.55	0.60
Min	30.027	30	29.97	29.94	29.92
Max	30.51	30.52	30.52	30.53	30.51

Table 6.4: Calculated apparent activation energy for 3”×6” concrete specimens (at core)

	water-cement ratio				
E_a (kJ/mol)	0.40	0.45	0.50	0.55	0.60
Min	29.92	29.87	29.81	29.74	29.66
Max	30.61	30.61	30.62	30.60	30.60

Apparent activation energy for 3”×6” concrete cylinders are presented in Figures 6-9 to 6-16. Each figure is briefly described as follow:

- Figures 6-9 to 6-13 show the comparison between the E_a at surface and core of concrete for each concrete specimen with w/c range from 0.40 to 0.60 with a 0.05 increment. Dashed curve indicates E_a at concrete surface and continuous curve represents E_a at the core of concrete.

- Figure 6-14 illustrates profiles of calculated E_a at the surface of five concrete specimens (w/c = 0.40 to 0.60 with 0.05 increment).

- Figure 6-15 shows the characteristic of calculated E_a at the core of five concrete specimens (w/c = 0.40 to 0.60 with 0.05 increment).

- Figure 6-16 shows E_a profiles at surface and core of all concrete specimens.

Profiles of E_a are analyzed and discussed in detail as follows:

- In Figures 6-9 to 6-13, E_a curve at the core has a deeper and narrower concave up profile than at the surface. However, after both curve comes across each other, the E_a at the surface is lower than at the core. This reason due to concrete temperature and the environmental condition as explained in Chapter 5.

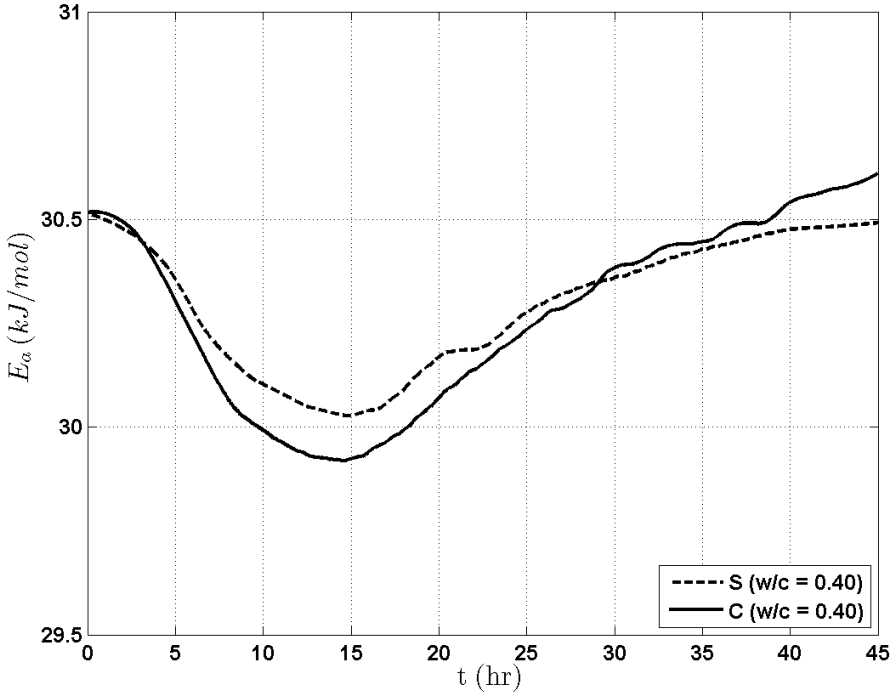

Figure 6-9: Apparent activation energy at surface and core of 3"×6" concrete cylinders (w/c = 0.4)

- In Figure 6-14, E_a profiles at the surface of five specimens have a similar trend. They look like an onion's layers which the curves with higher w/c ratios cover the ones with lower w/c ratios. Some curves generate a few bent profiles before reaching steady state. This is due to the interaction between concrete temperature and ambient conditions.

- In Figure 6-15, E_a profiles at the core of five specimens also generate the pattern of onion's layers. However, they do not have any bent. This is due to concrete temperature and ambient conditions, which is discussed in Chapter 5.

- Each specimen is required to give up some energy in order to overcome the minimum critical point of curvature:

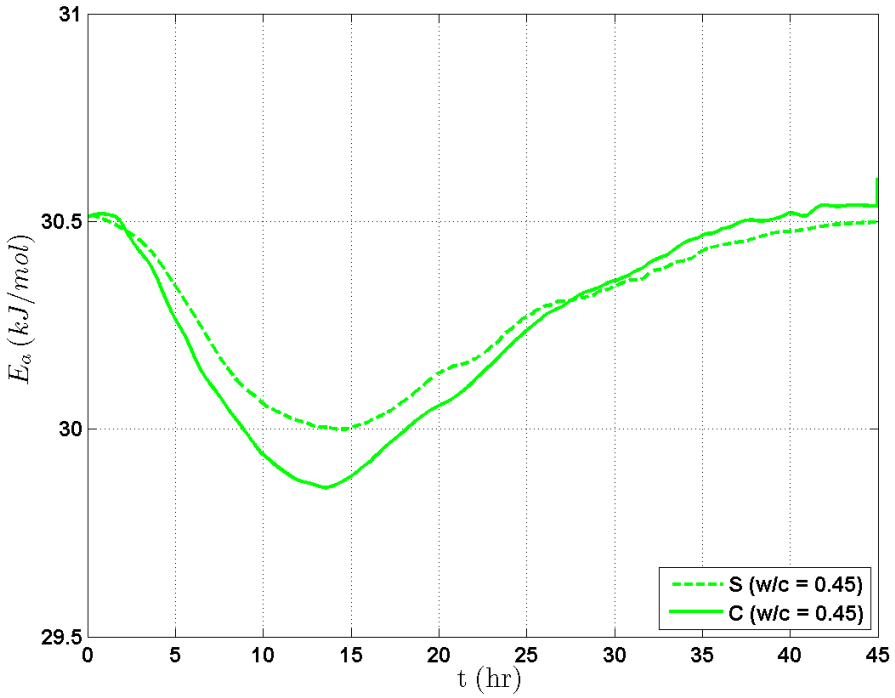

Figure 6-10: Apparent activation energy at surface and core of 3"×6" concrete cylinders (w/c = 0.45)

1. At surface: 0.487 kJ/mol (w/c = 0.40), 0.517 kJ/mol (w/c = 0.45), 0.545 kJ/mol (w/c = 0.50), 0.581 kJ/mol (w/c = 0.55) and 0.589 kJ/mol (w/c = 0.60).

2. At core: 0.598 kJ/mol (w/c = 0.40), 0.651 kJ/mol (w/c = 0.45), 0.74 kJ/mol (w/c = 0.50), 0.86 kJ/mol (w/c = 0.55) and 0.94 kJ/mol (w/c = 0.60).

3. It should be noticed that when w/c ratio increases, more energy is needed.

6.5.2 Calculated Heat of Hydration (3inch-by-6inch)

Values of maximum H(t) for five concrete specimens are summarized in Table 6.5. According to the results in Table 6.5, (a) $(H(t))_{max}$ increases when the w/c ratio increases. (b) $(H(t))_{max}$ at the core is higher than the one at the surface for all concrete specimens.

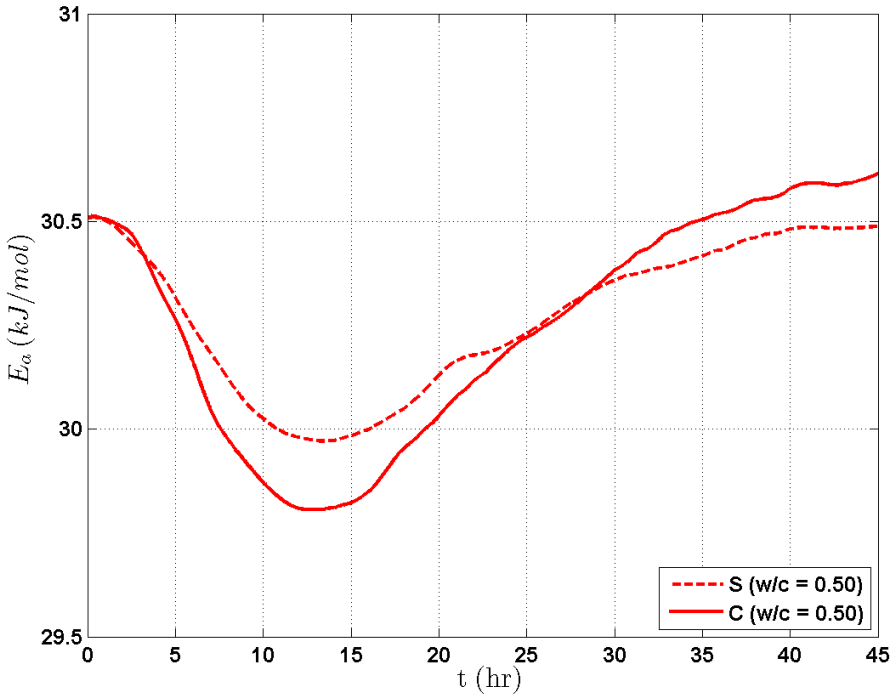

Figure 6-11: Apparent activation energy at surface and core of 3"×6" concrete cylinders (w/c = 0.50)

(c) $(H(t))_{max}$ at the surface of concrete ranges from 34.11 to 36.30 kJ/kg. (d) $(H(t))_{max}$ at the core of concrete ranges from 36.37 to 41.73 kJ/kg.

Table 6.5: Calculated heat of hydration for 3"×6" concrete specimens

	water-cement ratio				
$(H(t))_{max}$ (kJ/kg)	0.40	0.45	0.50	0.55	0.60
Surface	34.11	34.7	35.28	35.98	36.30
Core	36.37	37.62	38.72	39.45	41.73

Profiles of calculated heat of hydration for concrete specimens with w/c ratios of 0.40, 0.45, 0.50, 0.55 and 0.60 are presented in Figures 6-17 to 6-24.

- Figures 6-17 to 6-21 show the comparison between H(t) at top surface and core of concrete for each concrete specimen with w/c ratios ranging from 0.40 to 0.60

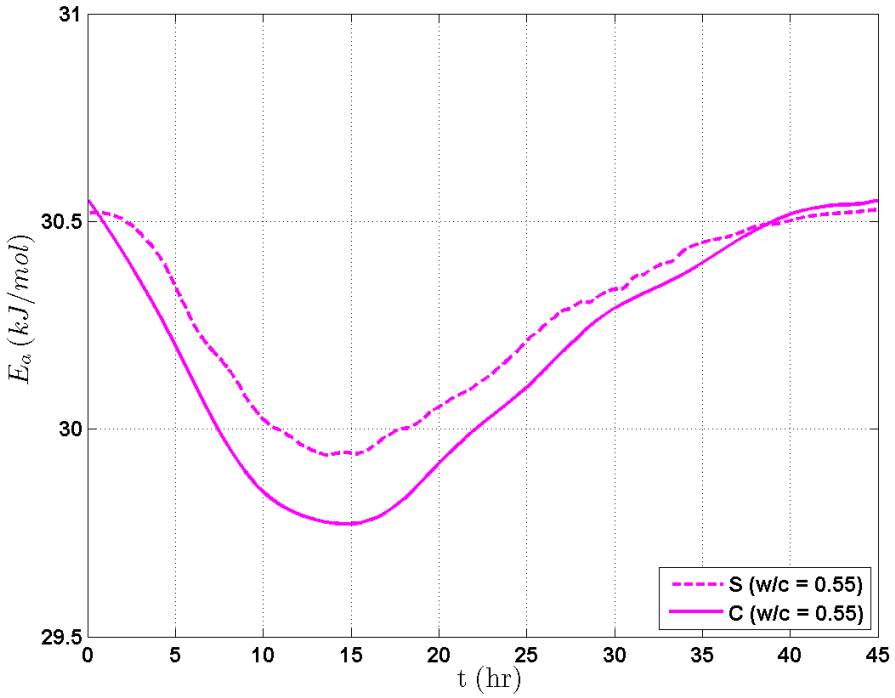

Figure 6-12: Apparent activation energy at surface and core of 3"×6" concrete cylinders (w/c = 0.55)

(with a 0.05 increment). Dashed curve and continuous curve represent H(t) at the surface and the core of concrete, respectively.

- Figure 6-22 illustrates profiles of calculated H(t) at the surface of five concrete specimens (w/c = 0.40 - 0.60 with 0.05 increment).

- Figure 6-23 shows development of H(t) at the core of five concrete specimens (w/c = 0.40 - 0.60 with 0.05 increment).

- Figure 6-24 demonstrates behavior of H(t) of all specimens at both surface and core.

Profiles of H(t) based on the first approach are analyzed and discussed in following:

- In Figures 6-17 to 6-21, H(t) curves at the core and the surface generate similar

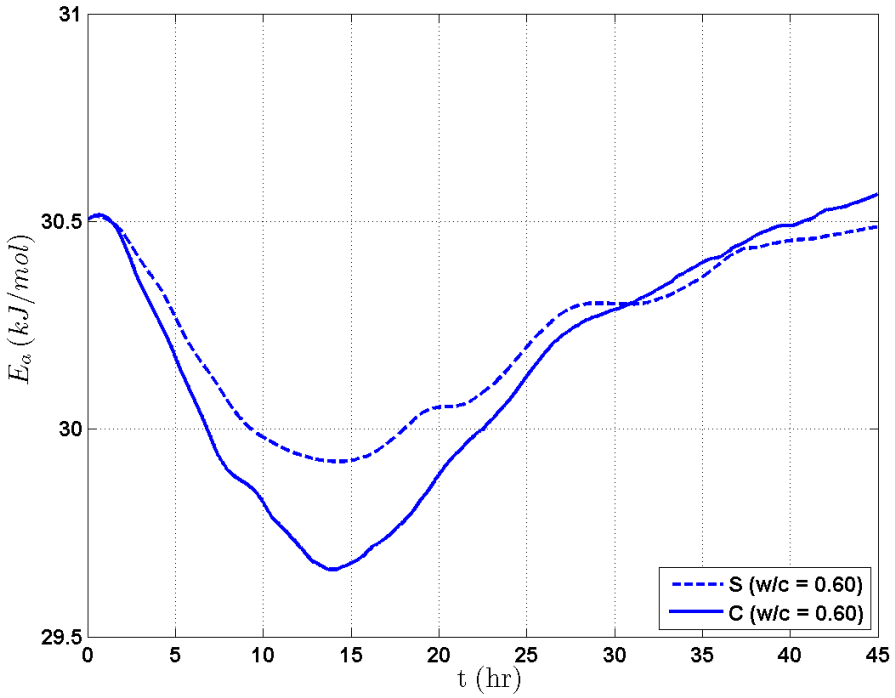

Figure 6-13: Apparent activation energy at surface and core of 3"×6" concrete cylinders (w/c = 0.60)

trend before reaching a break-even point, where the heat at core of concrete produces higher value than the one at surface of concrete. After passing intersection the point, concrete core generates less heat than the heat at the surface (refer to Chapter 5 for detailed explanation).

- According to Figure 6-22, H(t) profiles at the surface of five specimens are very similar. In Figure 6-23, heat development at the core of concrete specimens exhibits similar profile. Additionally, specimens with higher w/c ratios produce more heat than the specimens with lower w/c ratios. This is due to equal mass of cement, sand and gravel used.

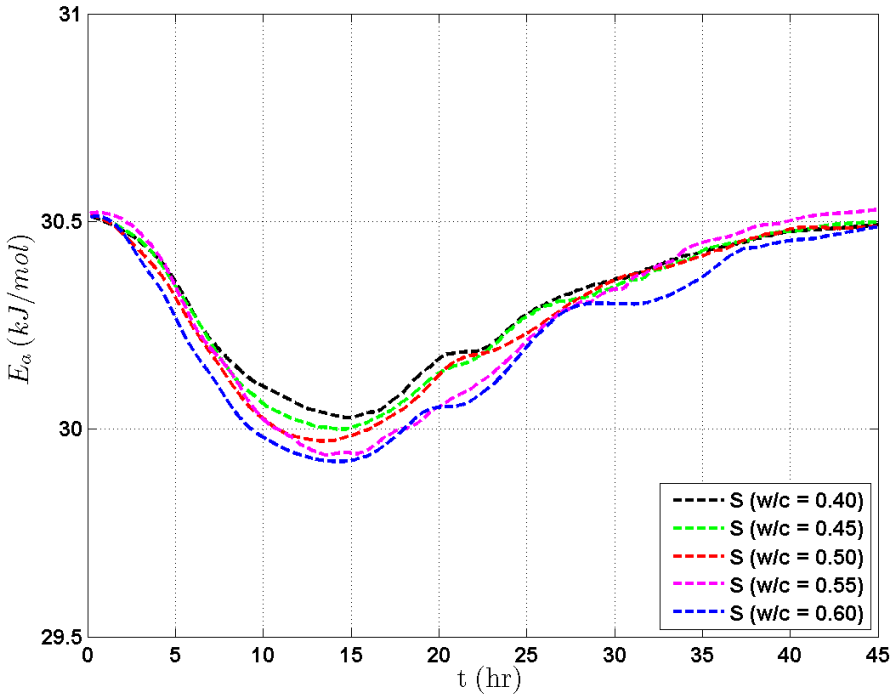

Figure 6-14: Apparent activation energy at surface of 3"×6" concrete cylinders (w/c = 0.4 - 0.6)

6.5.3 Relationship between Heat of Hydration and Apparent Activation Energy (3inch-by-6inch)

In Figures 6-25 to 6-34, linear dashed and solid lines demonstrate the relation between hydration heat and E_a at the surface and the core of concrete cylinders, respectively. In Figures 6-25 to 6-34, each curve indicates that apparent activation energy is inversely linear to the heat of hydration. This result is in good agreement with Eq.6.8 and reference [39].

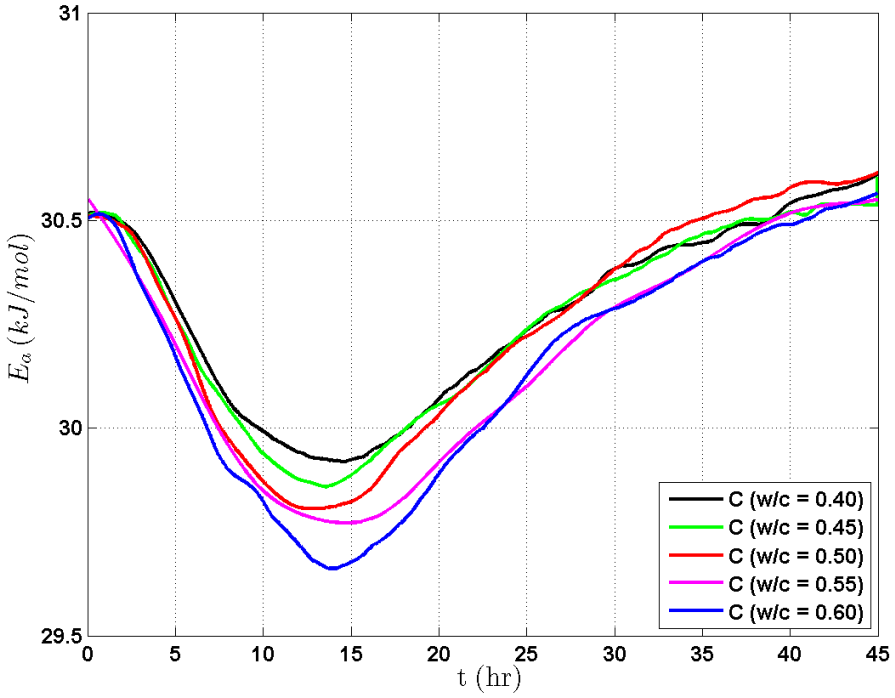

Figure 6-15: Apparent activation energy at core of 3"×6" concrete cylinders (w/c = 0.4 - 0.6)

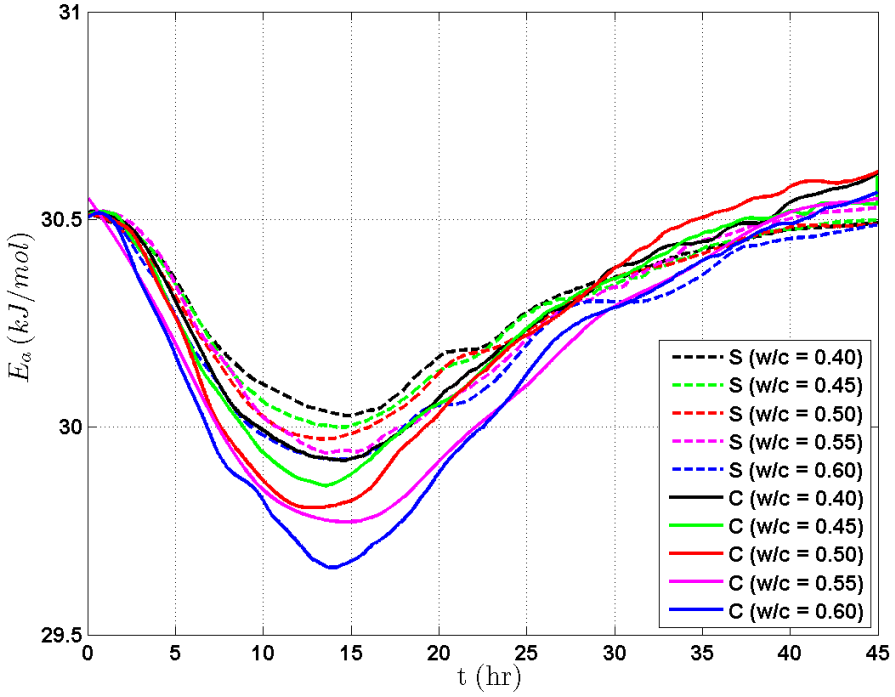

Figure 6-16: Apparent activation energy at surface and core of 3"×6" concrete cylinders (w/c = 0.4 - 0.6)

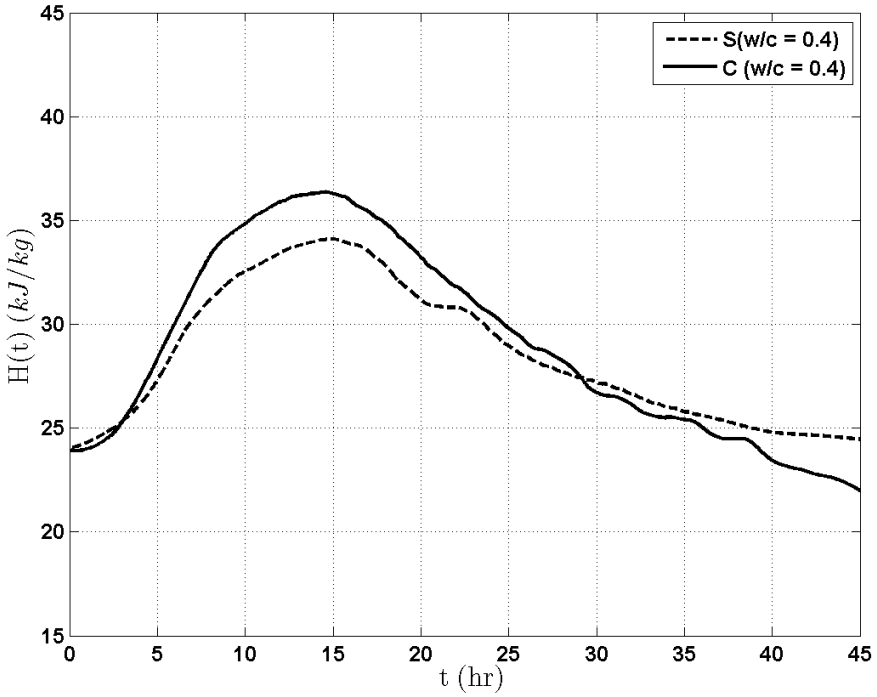

Figure 6-17: Heat of hydration at the surface and the core of 3"×6" concrete cylinders (w/c = 0.40)

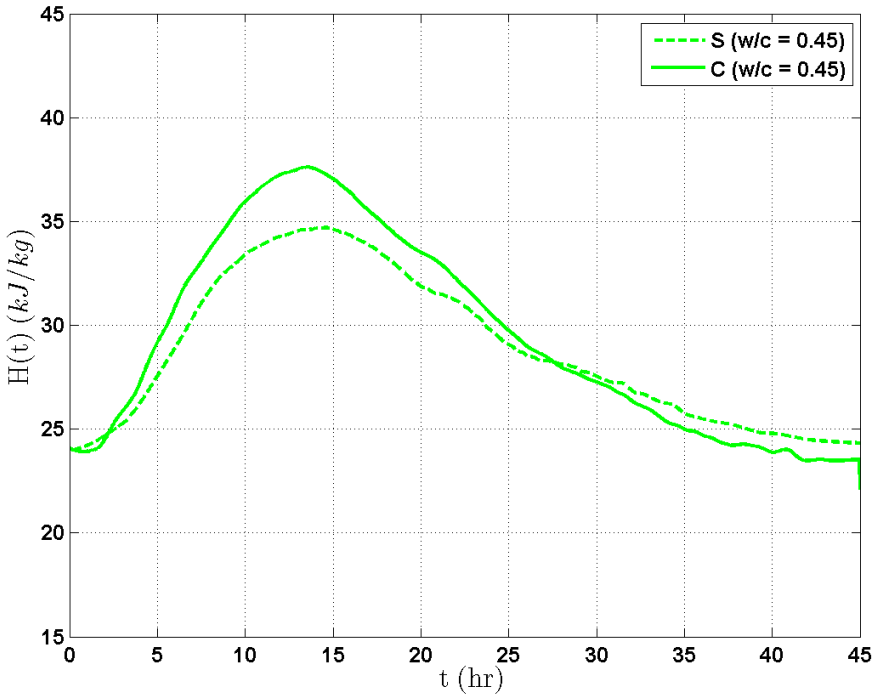

Figure 6-18: Heat of hydration at the surface and the core of 3"×6" concrete cylinders (w/c = 0.45)

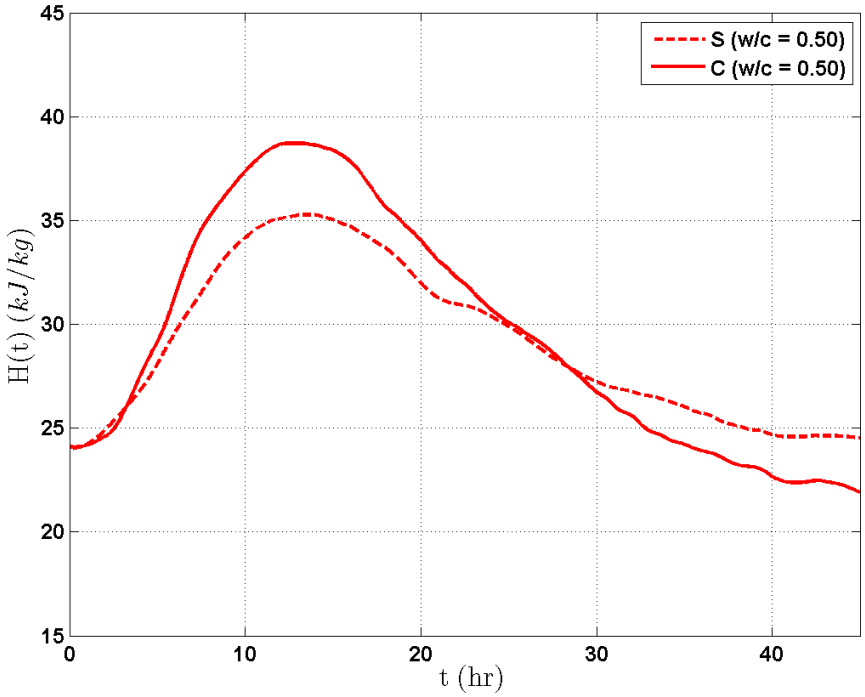

Figure 6-19: Heat of hydration at the surface and the core of 3”×6” concrete cylinders (w/c = 0.50)

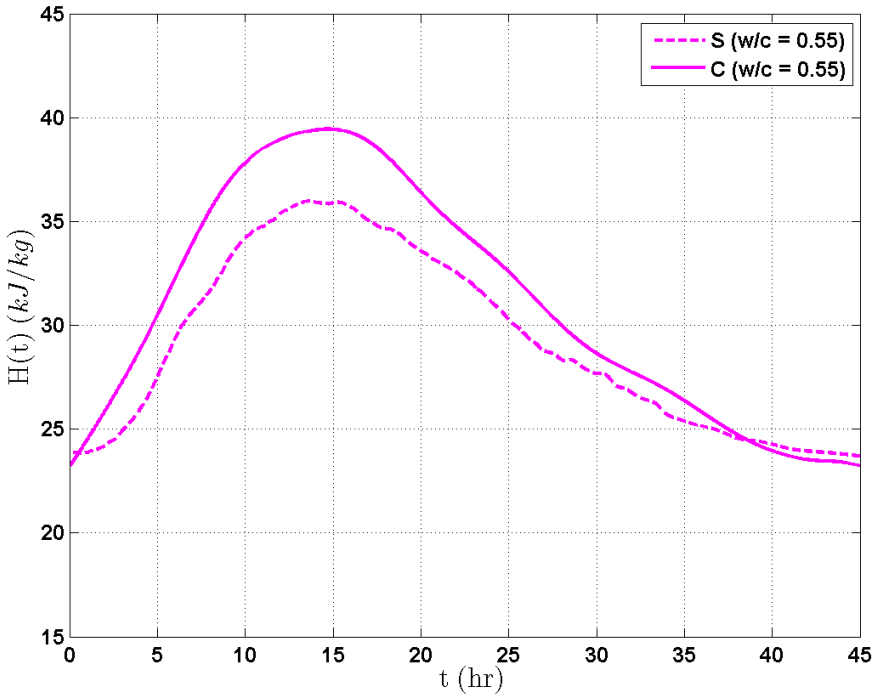

Figure 6-20: Heat of hydration at the surface and the core of 3”×6” concrete cylinders (w/c = 0.55)

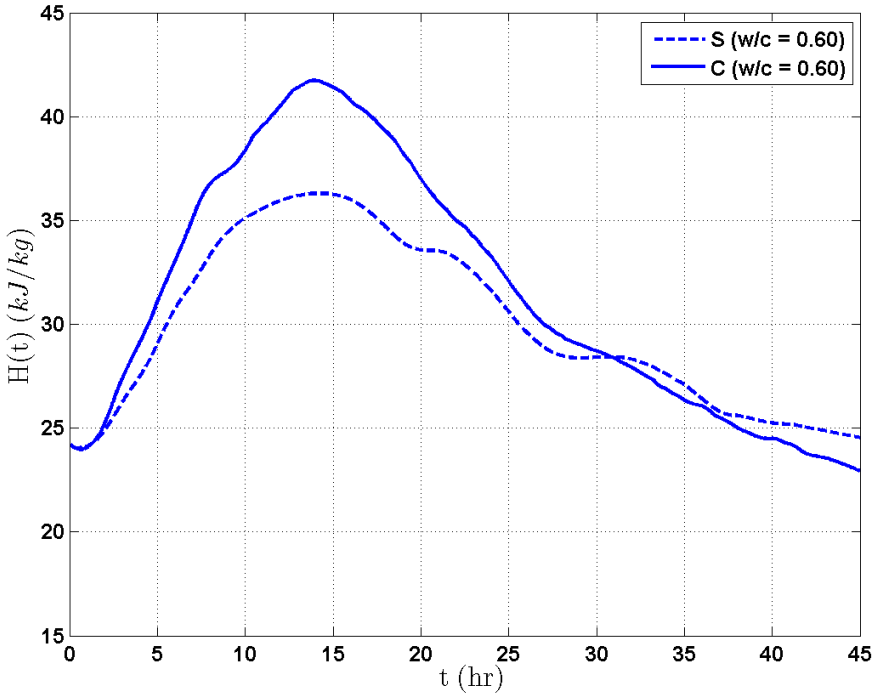

Figure 6-21: Heat of hydration at the surface and the core of 3”×6” concrete cylinders (w/c = 0.60)

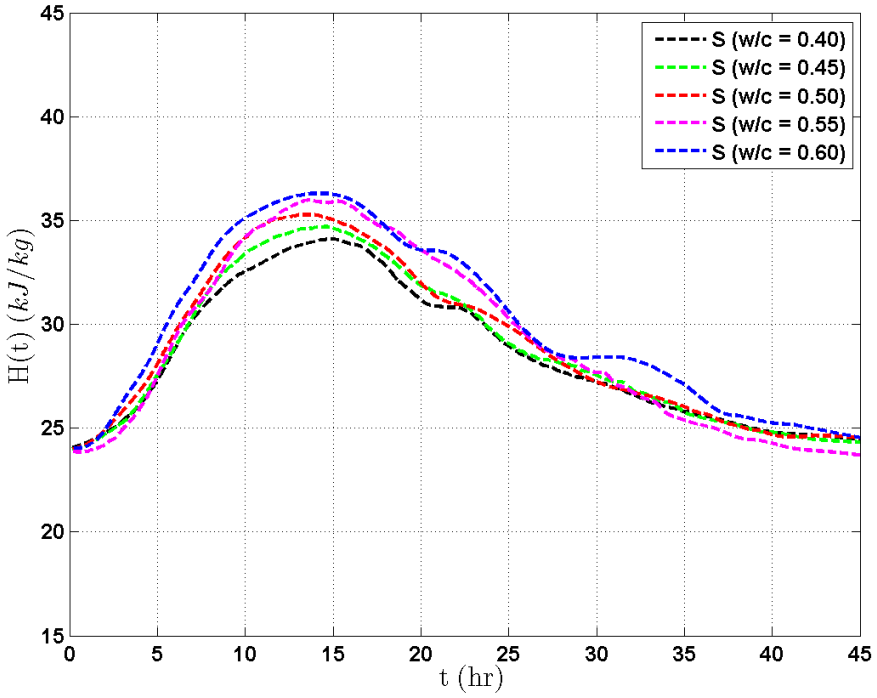

Figure 6-22: Heat of hydration at the surface of 3”×6” concrete cylinders (w/c = 0.40 - 0.60)

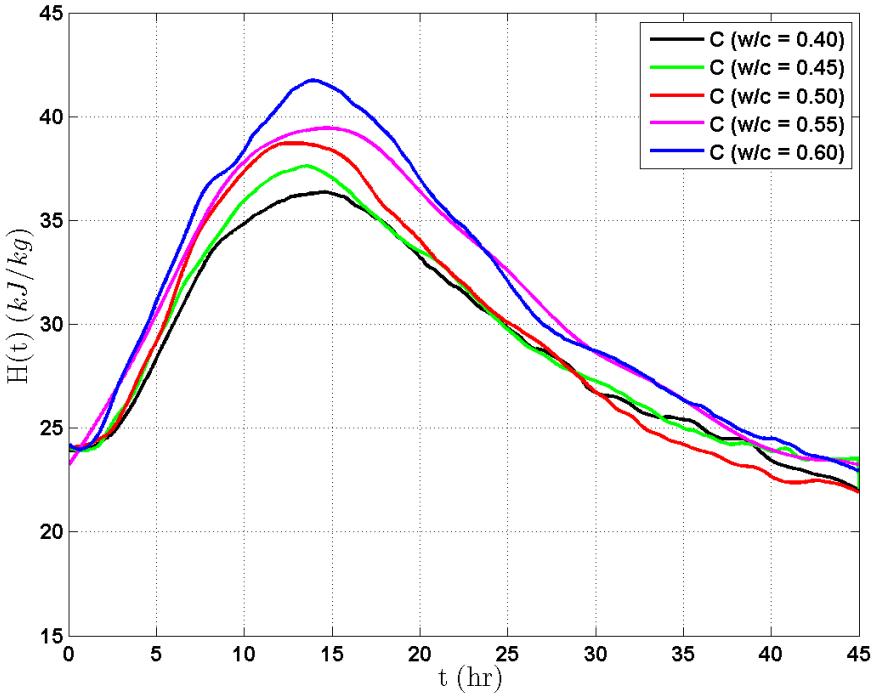

Figure 6-23: Heat of hydration at the core of 3”×6” concrete cylinders (w/c = 0.40 - 0.60)

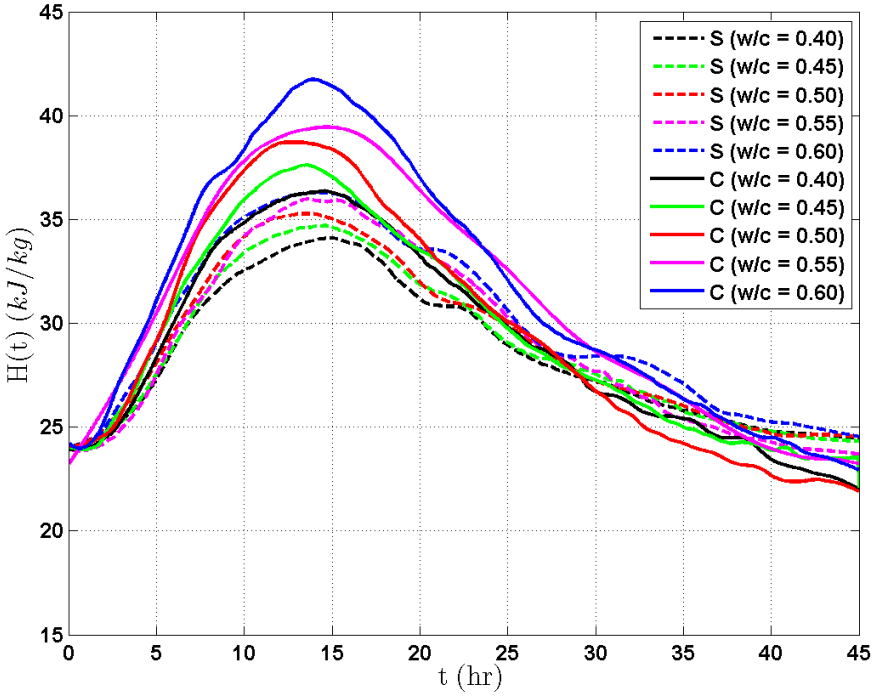

Figure 6-24: Heat of hydration at the surface and the core of 3”×6” concrete cylinders (w/c = 0.40 - 0.60)

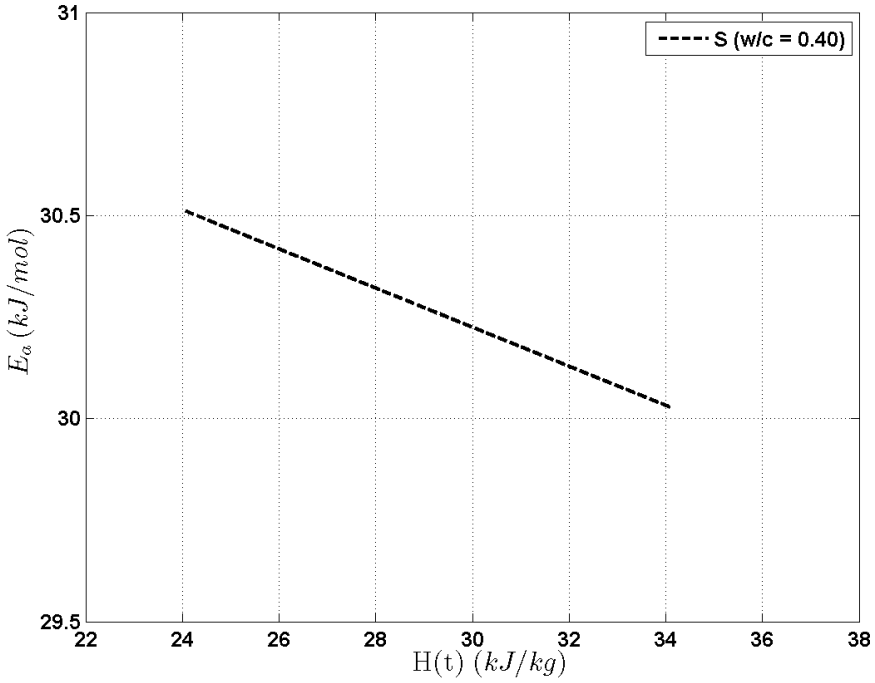

Figure 6-25: H(t) vs. E_a at the surface of 3"×6" concrete cylinder for w/c = 0.40

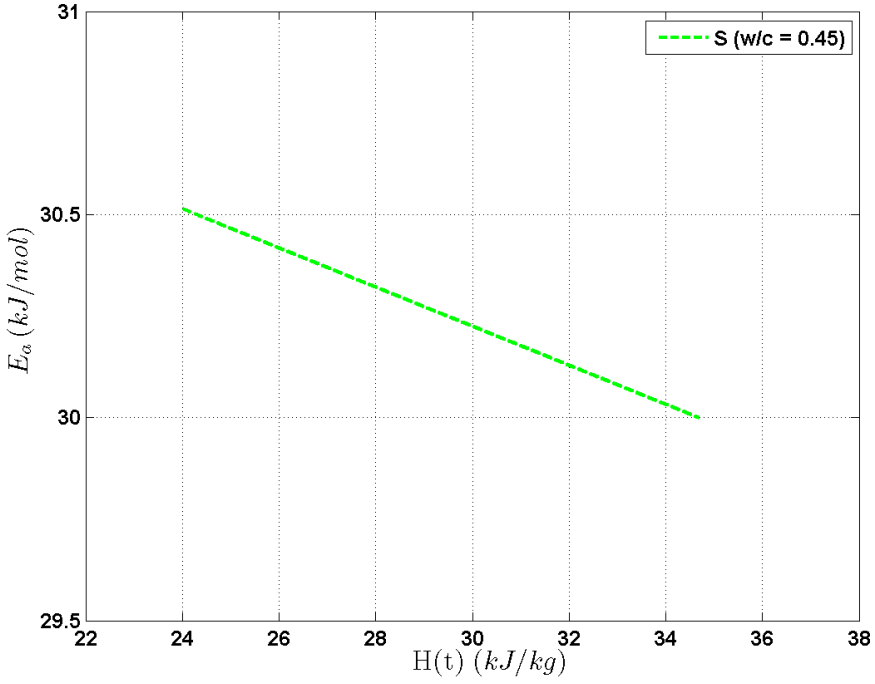

Figure 6-26: H(t) vs. E_a at the surface of 3"×6" concrete cylinder for w/c = 0.45

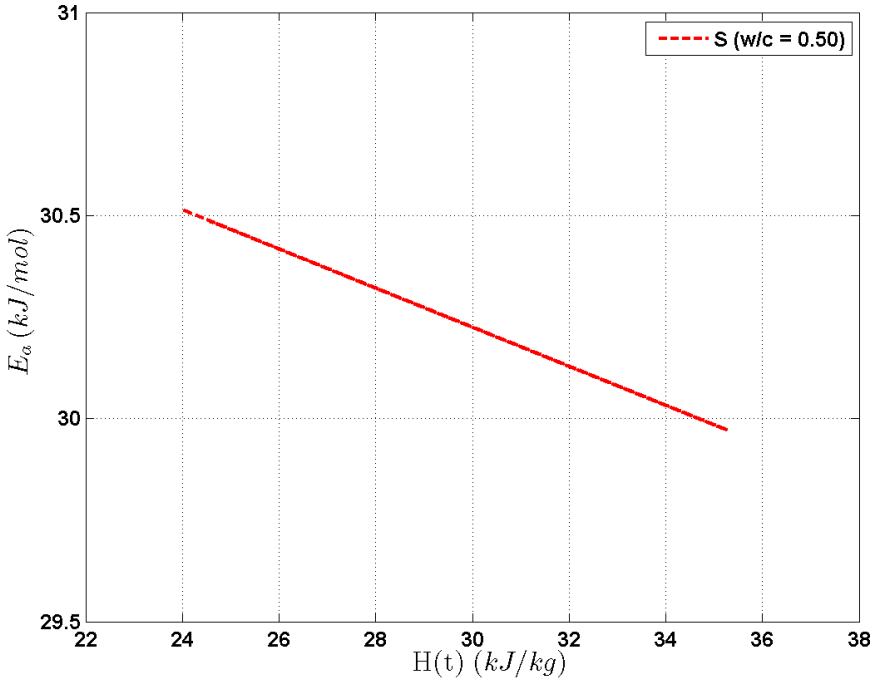

Figure 6-27: H(t) vs. E_a at the surface of 3"×6" concrete cylinder for w/c = 0.50

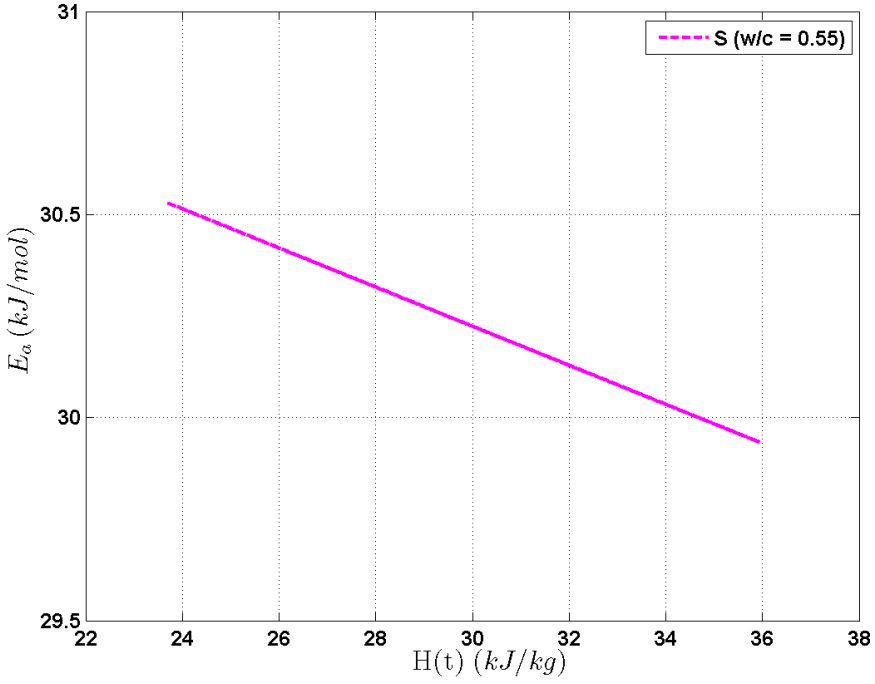

Figure 6-28: H(t) vs. E_a at the surface of 3"×6" concrete cylinder for w/c = 0.55

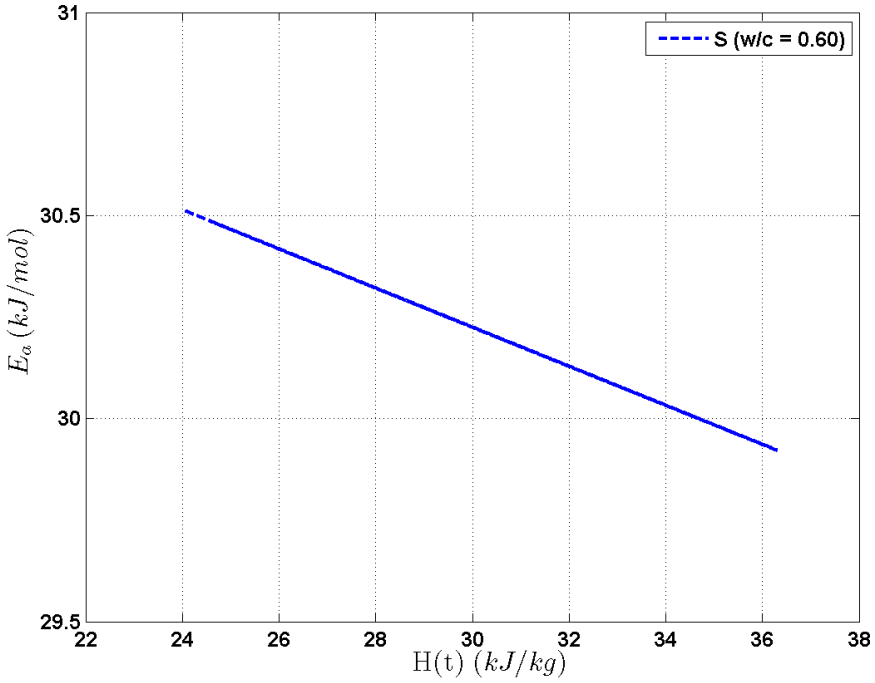

Figure 6-29: H(t) vs. E_a at the surface of 3"×6" concrete cylinder for w/c = 0.60

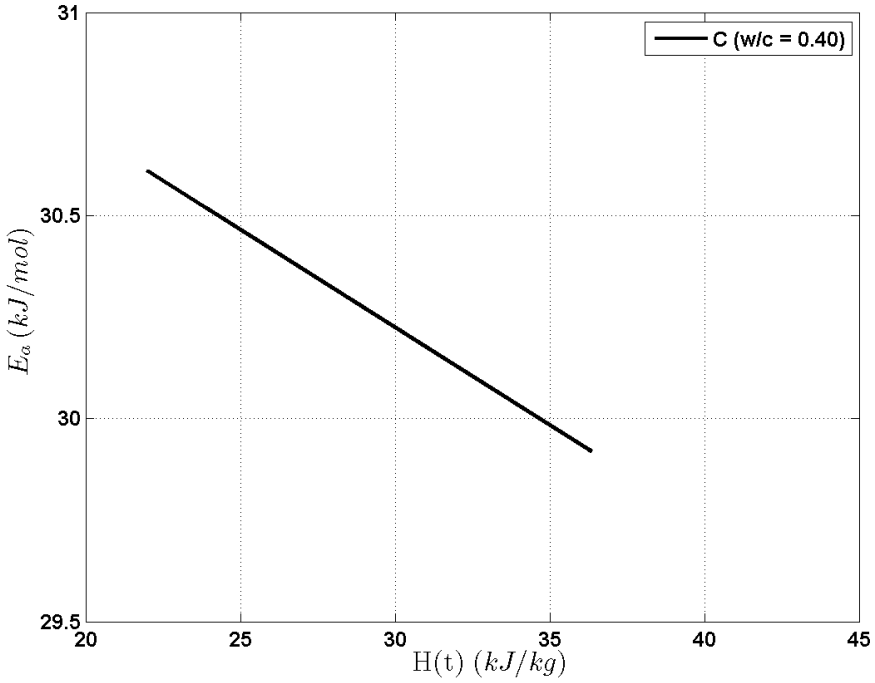

Figure 6-30: H(t) vs. E_a at the core of 3"×6" concrete cylinder for w/c = 0.40

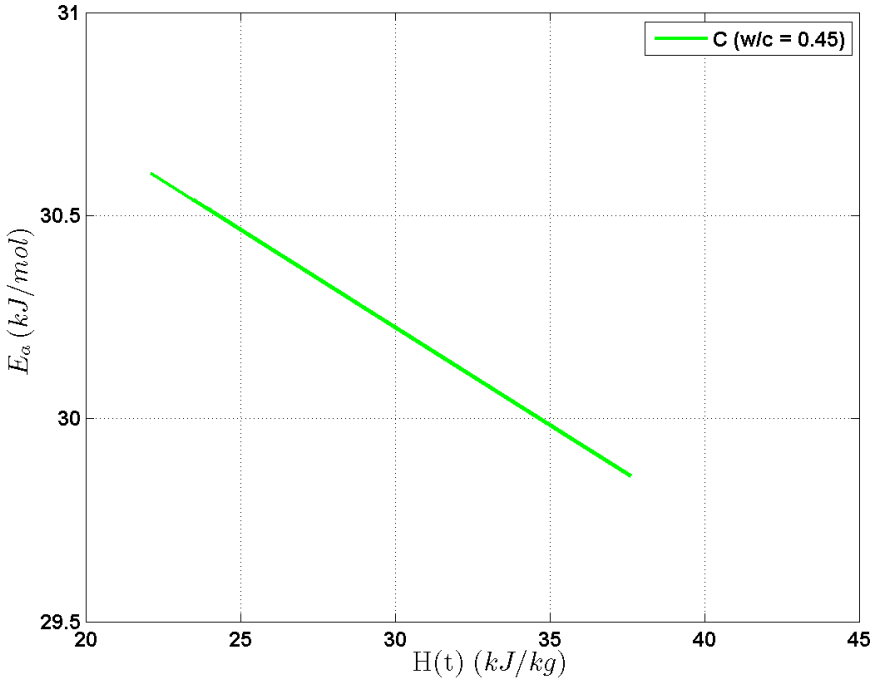

Figure 6-31: H(t) vs. E_a at the core of 3"×6" concrete cylinder for w/c = 0.45

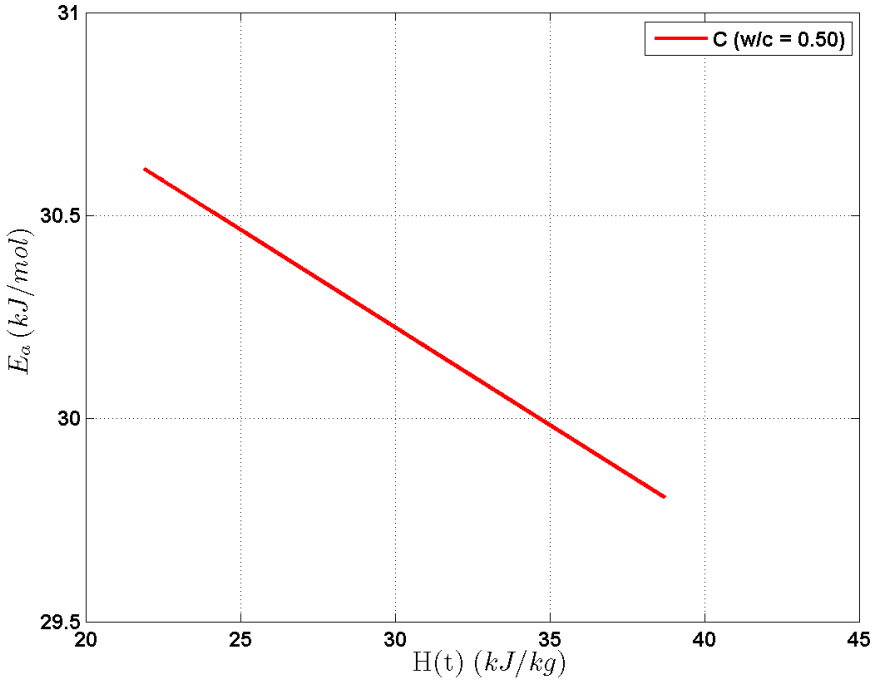

Figure 6-32: H(t) vs. E_a at the core of 3"×6" concrete cylinder for w/c = 0.50

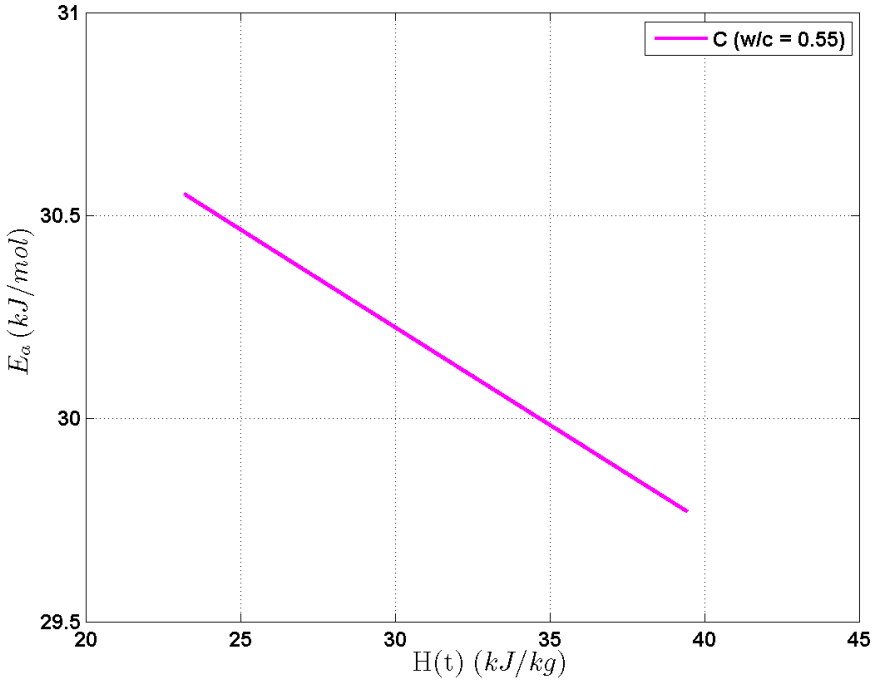

Figure 6-33: H(t) vs. E_a at the core of 3"×6" concrete cylinder for w/c = 0.55

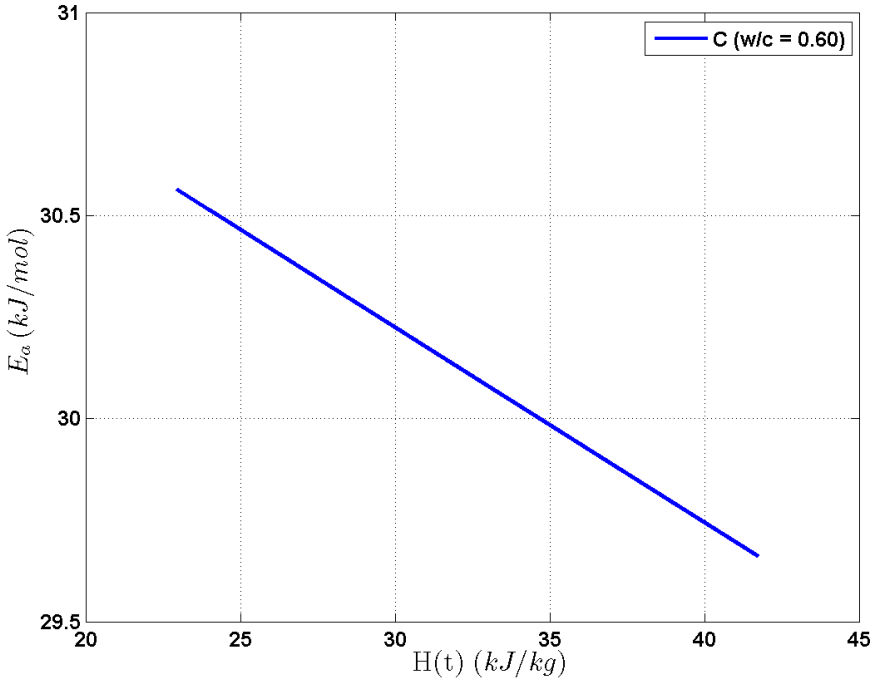

Figure 6-34: H(t) vs. E_a at the core of 3"×6" concrete cylinder for w/c = 0.60

6.6 Results and Discussion for 3inch-by-6inch Concrete Specimens - Second Approach

E_a equals to 29,000 J/mol and 33,500 J/mol were used in the calculation of heat of hydration for 3"×6" concrete specimens. The results are presented and discussed in this section.

Summary of calculated potential heat of hydration at surface and core of specimens are presented in Tables 6.6 and 6.7. $(H(t))_{max}$ is dependent on the w/c ratio. As seen in both tables, higher maximum heat of hydration can be obtained with higher w/c ratios. When E_a equals to 29,000 J/mol, maximum H(t) at surface and core of specimens ranges from 29.13 kJ/kg to 37.26 kJ/kg, and 31.87 kJ/kg to 43.47 kJ/kg, respectively. When E_a equals to 33,500 J/mol, maximum H(t) at surface and core of specimens ranges from 31.80 kJ/kg to 41.14 kJ/kg, and 35.56 kJ/kg to 50.04 kJ/kg, respectively.

Table 6.6: Calculated heat of hydration for 3"×6" concrete specimens (E_a = 29,000 J/mol)

	Water-to-cement ratio				
$(H(t))_{max}$ (kJ/kg)	0.40	0.45	0.50	0.55	0.60
Surface	29.13	30.62	32.87	33.51	37.26
Core	31.87	35.23	38.68	39.78	43.47

6.6.1 Concrete Equivalent Age (t_e) (3inch-by-6inch)

Concrete equivalent age (t_e) based on E_a of 29,000 J/mol and 33,500 J/mol are shown in Figures 6-35 to 6-50. Behavior of t_e is described as follows:

Table 6.7: Calculated heat of hydration for 3”×6” concrete specimens (E_a = 33,500 J/mol)

	water-cement ratio				
$(H(t))_{max}$ (kJ/kg)	0.40	0.45	0.50	0.55	0.60
Surface	31.80	33.07	35.82	36.85	41.14
Core	35.56	39.12	44.03	44.66	50.04

1. In all t_e profiles, dashed line and continuous line indicate the t_e curves using on surface and core temperature data, respectively.

2. Figures 6-35 to 6-39 show t_e profiles of individual concrete specimen based on E_a of 29,000 J/mol.

3. Figure 6-40 illustrates the t_e profiles at concrete surface for all specimens (E_a = 29,000 J/mol).

4. Figure 6-41 illustrates the t_e profiles at concrete core for all specimens (E_a = 29,000 J/mol).

5. Figures 6-43 to 6-47 show the t_e profiles of individual concrete specimen based on E_a of 33,500 J/mol.

6. Figure 6-48 illustrates the t_e profiles at concrete surface of all specimens (E_a = 33,500 J/mol).

7. Figure 6-49 illustrates the t_e profiles at concrete core for all specimens (E_a = 33,500 J/mol).

All t_e figures how that the t_e of concrete specimen increases with the increase of the w/c ratio. In addition, the value of t_e is a function of E_a and concrete temperature (T_c). Higher values of t_e for each specimen can be obtained when the value of E_a increases, given that the same temperature data is used in the calculation.

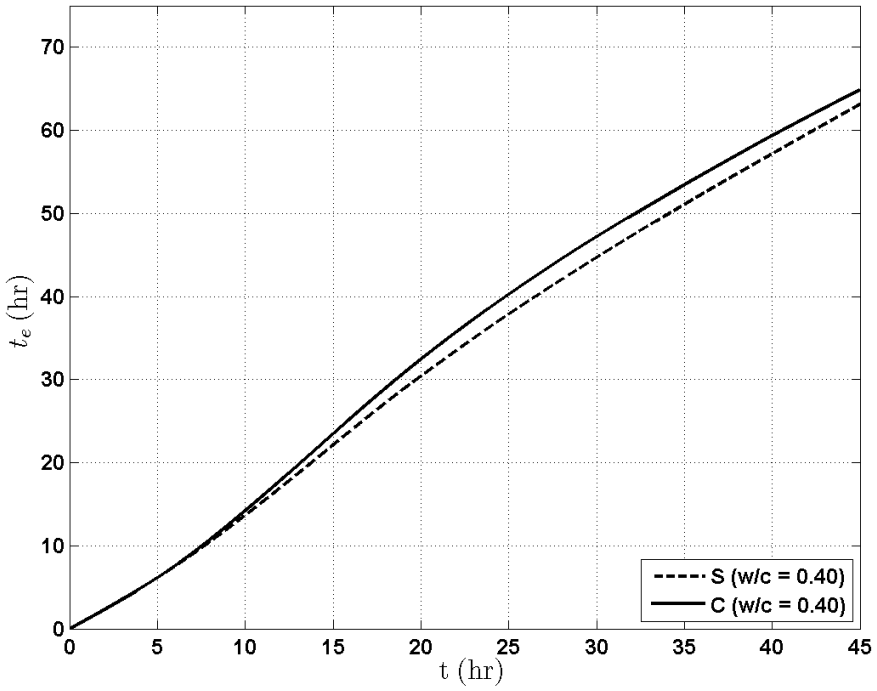

Figure 6-35: Time equivalent vs. real time of 3”×6” concrete cylinder based on surface and core temperature (w/c = 0.40) - E_a = 29,000 J/mol

6.6.2 Calculated Heat of Hydration (3inch-by-6inch)

Heat of hydration profiles of 3”×6” concrete cylinders are presented in Figures 6-51 to 6-66 and describe as follows:

1. In all H(t) profiles, dashed line and continuous line indicate the H(t) curves calculated based on the surface and core temperature data, respectively.

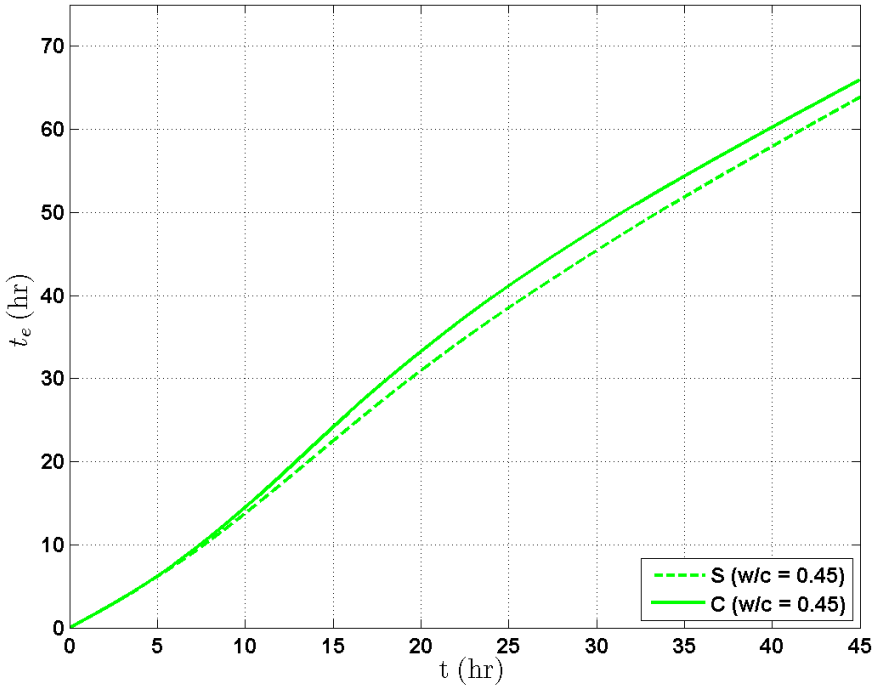

Figure 6-36: Time equivalent vs. real time of 3"×6" concrete cylinder based on surface and core temperature (w/c = 0.45) - E_a = 29,000 J/mol

2. Figures 6-51 to 6-55 show the t_e profiles of individual concrete specimen based on E_a of 29,000 J/mol.

3. Figure 6-56 illustrates H(t) profiles at the surface of all specimens (E_a = 29,000 J/mol).

4. Figure 6-57 illustrates H(t) profiles at the core of all specimens (E_a = 29,000 J/mol).

5. Figure 6-58 shows H(t) profile at the surface and the core of all specimens (E_a = 29000 J/mol).

6. Figures 6-59 to 6-63 show H(t) profiles of individual concrete specimen based on E_a of 33,500 J/mol.

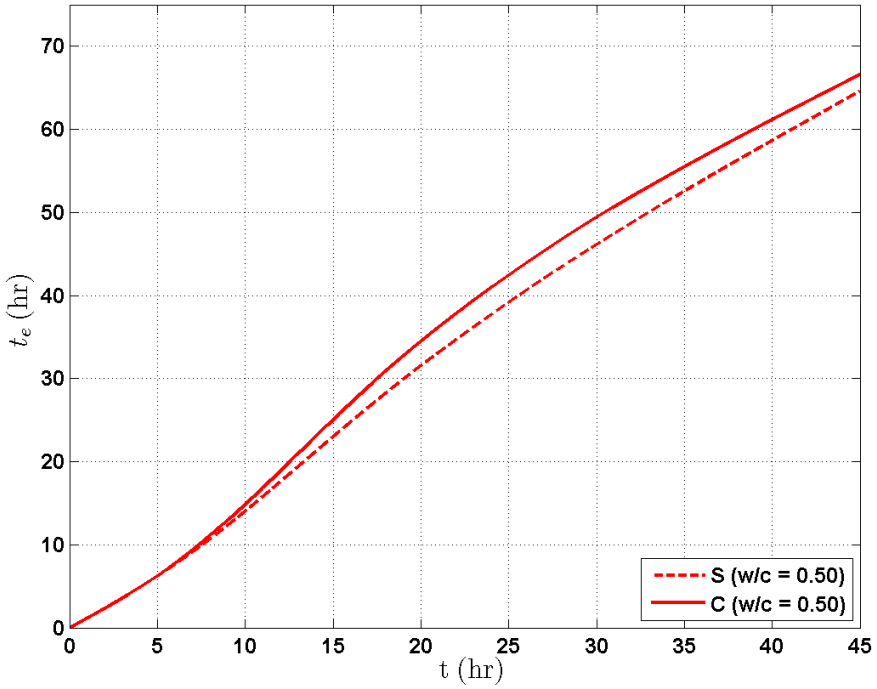

Figure 6-37: Time equivalent vs. real time of 3"×6" concrete cylinder based on surface and core temperature (w/c = 0.50) - E_a = 29,000 J/mol

7. Figure 6-64 illustrates H(t) profiles at the surface of all specimens (E_a = 33,500 J/mol).

8. Figure 6-65 illustrates H(t) profiles at the core of all specimens (E_a = 33,500 J/mol).

9. Figure 6-66 show H(t) profiles at the surface and the core of all specimens (E_a = 33,500 J/mol).

According to Figures 6-58 and 6-66, heat of hydration increased rapidly and fluctuation was observed in all curves. This is due to the large amount of C_3S (56.9%) in typical Type I cement [29]. Also, the crossover effect exists in all specimens when comparing the heat released at the surface and at the core. After reaching the peak

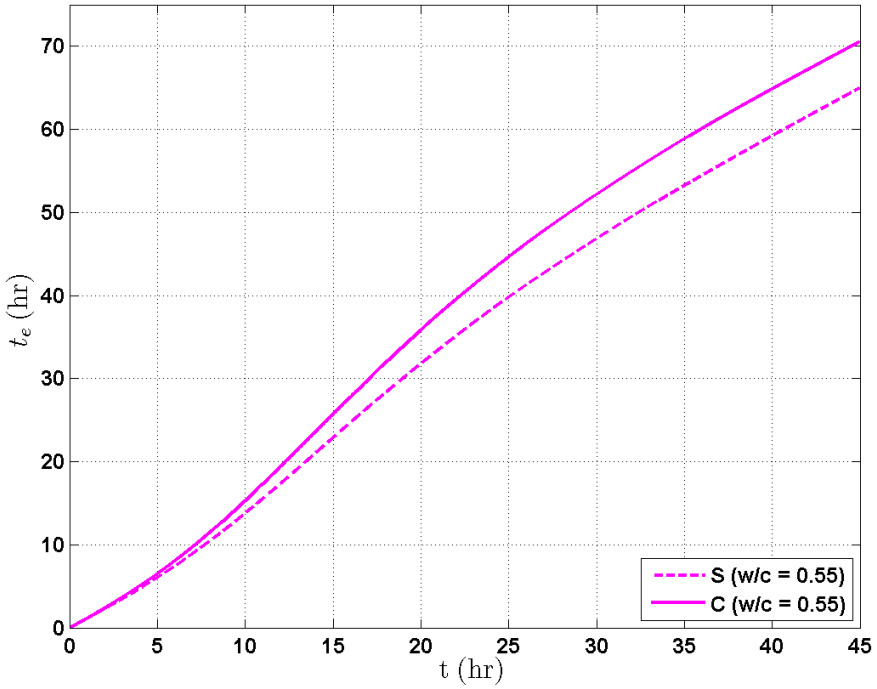

Figure 6-38: Time equivalent vs. real time of 3"×6" concrete cylinder based on surface and core temperature (w/c = 0.55) - E_a = 29,000 J/mol

heat of hydration, (a) the heat at the surface of concrete specimens decreased at a higher rate for a duration of approximately 15 hours ($E_a = 29,000 J/mol$) and 20 hours ($E_a = 33,500 J/mol$) (Figures 6-56 and 6-64), (b) the heat at the core of concrete specimens decreases at a higher rate for about 35 hours ($E_a = 29,000 J/mol$) and 40 hours ($E_a = 33,500 J/mol$), then approaching steady state at a slower rate for the remaining experiment time.

6.7 Summary

Temperature data obtained from experimental measurement is the key parameter in the study of apparent activation energy and heat of hydration.

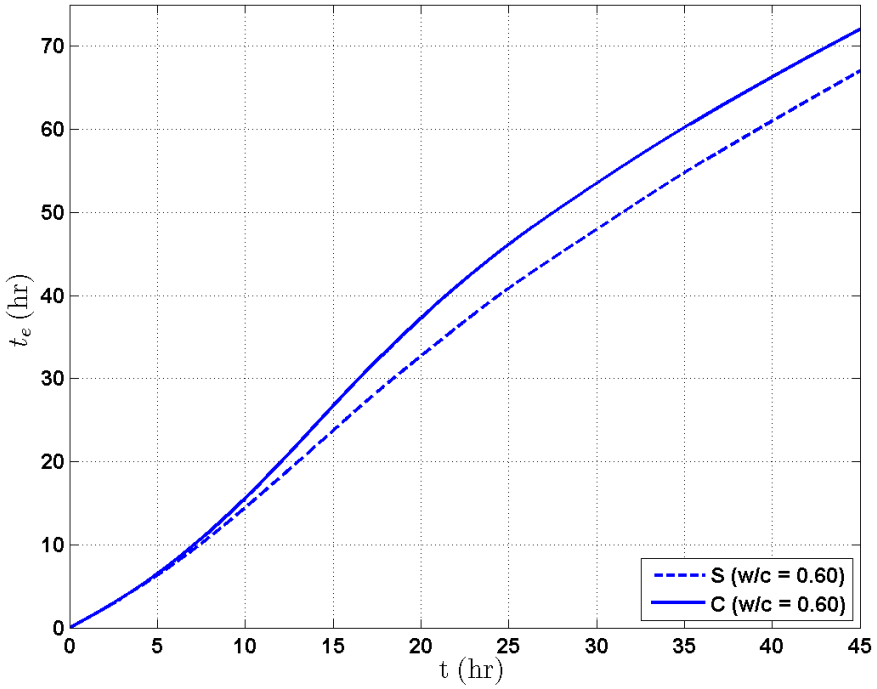

Figure 6-39: Time equivalent vs. real time of 3"×6" concrete cylinder based on surface and core temperature (w/c = 0.60) - E_a = 29,000 J/mol

In the first approach: (a) average (E_{amin}) and (E_{amax}) of 4"×8" specimens were determined to be 29.21 kJ/mol and 30.65 kJ/mol, respectively. (b) average (E_{amin}) and (E_{amax}) of 3"×6" specimens were found to be 29.97 kJ/mol and 30.52 kJ/mol (at the surface), and 29.8 kJ/mol and 30.61 kJ/mol (at the core), respectively. (c) average $H(t)_{max}$ was found to be 51.16 kJ/kg for 4"×8" specimens, 35.274 kJ/kg and 38.778 kJ/kg at the surface and the core of 3"×6" specimens, respectively. (d) heat of hydration is linearly related to apparent activation energy. (e) heat of hydration increases as the w/c ratio increases. (e) more energy is required to enable cement hydration when w/c ratios increases, given that specimens consist of equal amount of cement, sand and gravel. (f) apparent activation energy and heat of hydration both depend on concrete temperature.

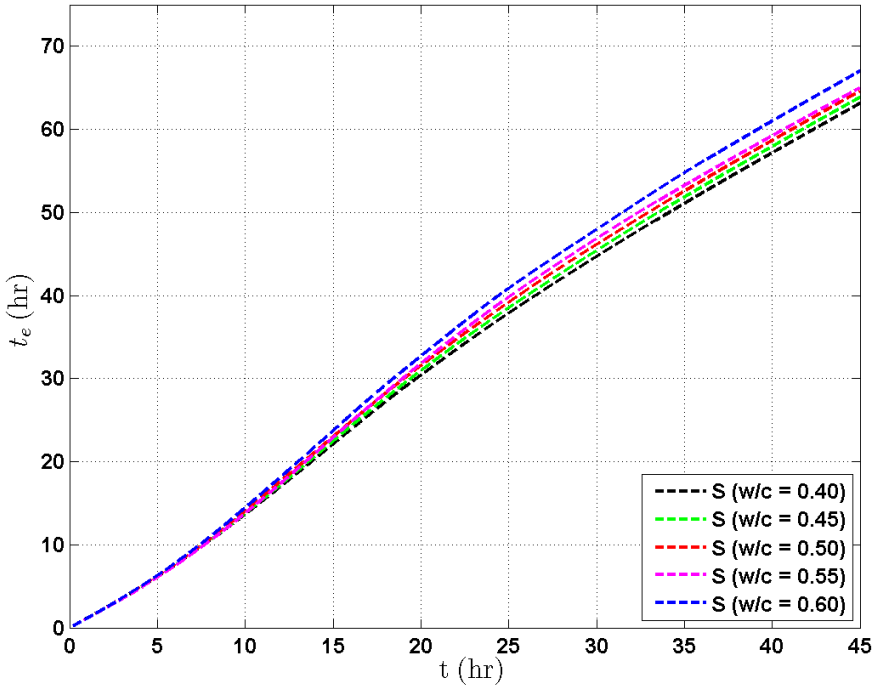

Figure 6-40: Time equivalent vs. real time of 3"×6" concrete cylinders based on surface temperature (w/c = 0.40 - 0.60) - E_a = 29,000 J/mol

In the second approach: (a) when E_a equals to 29,000 J/mol, the average values of maximum H(t) were determined to be 55 kJ/kg (for 4"×8" specimens), 32.68 kJ/kg (at the surface of 3"×6" specimens), and 37.81 kJ/kg (at the core of 3"×6" specimens). (b) when E_a equals to 33,500 J/mol, the average values of maximum H(t) were found to be 70.4 kJ/kg (for 4"×8" specimens), 35.74 kJ/kg (at the surface of 3"×6" specimens), and 42.68 kJ/kg (at the core of 3"×6" specimens). (c) most heat of hydration curves showed fluctuation, this may due to the presence of tricalcium silicate during heat of hydration acceleration period. (d) heat of hydration was calculated based on concrete temperature and apparent activation energy. (e) potential heat of hydration directly relates to water to cement ratio.

A summary of heat of hydration calculated base on both approaches can be found in

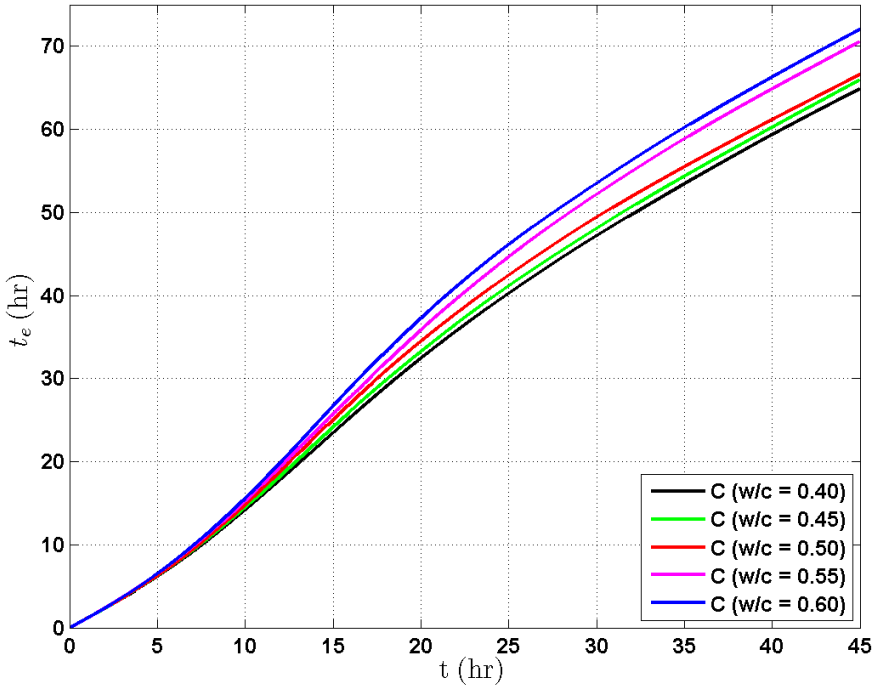

Figure 6-41: Time equivalent vs. real time of 3"×6" concrete cylinders based on core temperature (w/c = 0.40 - 0.60) - E_a = 29,000 J/mol

Table 6.8. When comparing the first approach and the second approach (with E_a equals to 29 kJ/mol), we can see that values of heat of hydration are only slightly different. This is because the value of E_a used in the second approach is about the same as value of E_a obtained in the first approach. It should be noticed that the value of E_a equals to 33.5 kJ/mol used in the second approach generates the highest hydration heat. E_a equals to 33.5 kJ/mol was used in order to obtain the upper bound value of heat liberates within concrete structure.

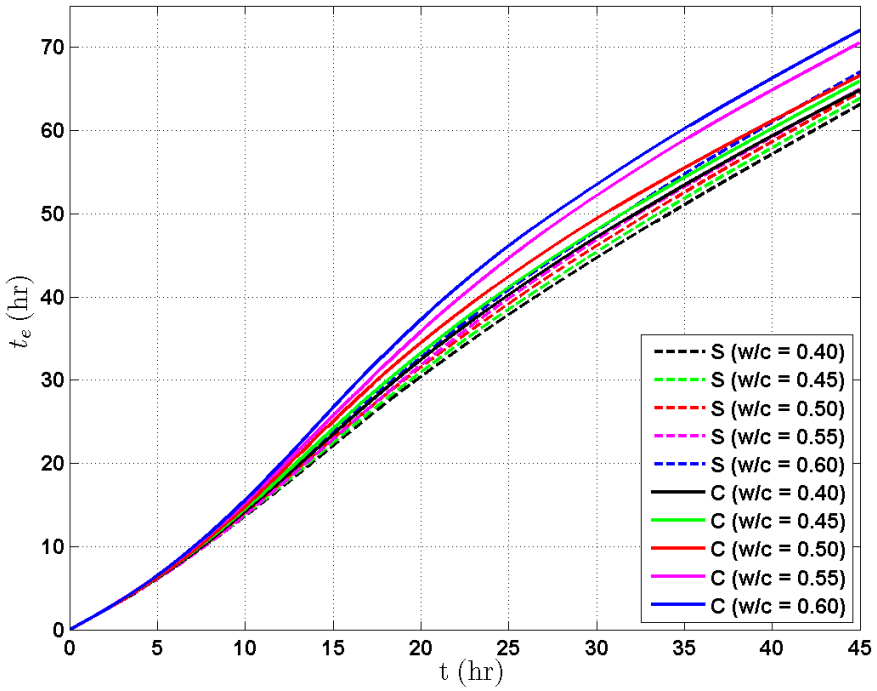

Figure 6-42: Time equivalent vs. real time of 3”×6” concrete cylinders based on surface and core temperature (w/c = 0.40 - 0.60) - E_a = 29,000 J/mol

Table 6.8: Average heat of hydration for all concrete specimens

	4”×8”	3”×6”	
E_a (kJ/mol)	H(t) (kJ/kg)	H(t)$_{surface}$ (kJ/kg)	H(t)$_{core}$ (kJ/kg)
29 to 30.5	51.16	35.27	38.78
29	55	32.70	37.81
33.5	70.4	35.74	42.68

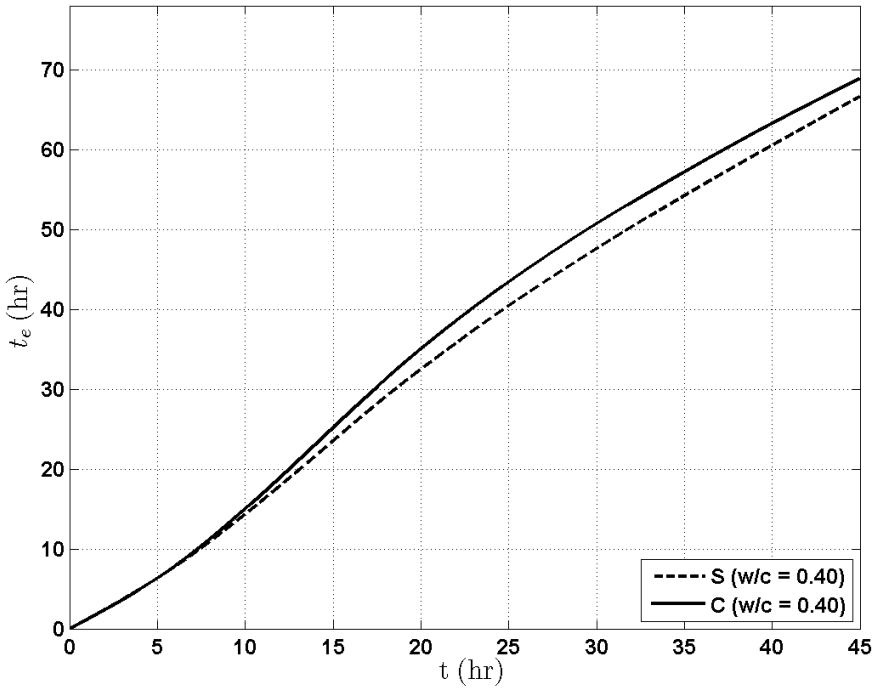

Figure 6-43: Time equivalent vs. real time of 3”×6” concrete cylinder based on surface and core temperature (w/c = 0.40) - E_a = 33,500 J/mol

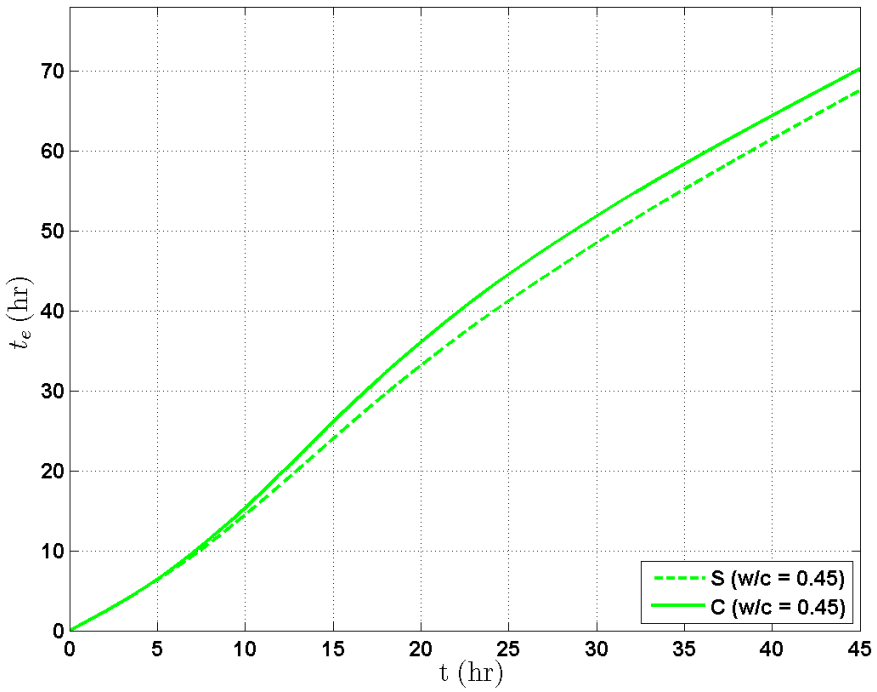

Figure 6-44: Time equivalent vs. real time of 3”×6” concrete cylinder based on surface and core temperature (w/c = 0.45) - E_a = 33,500 J/mol

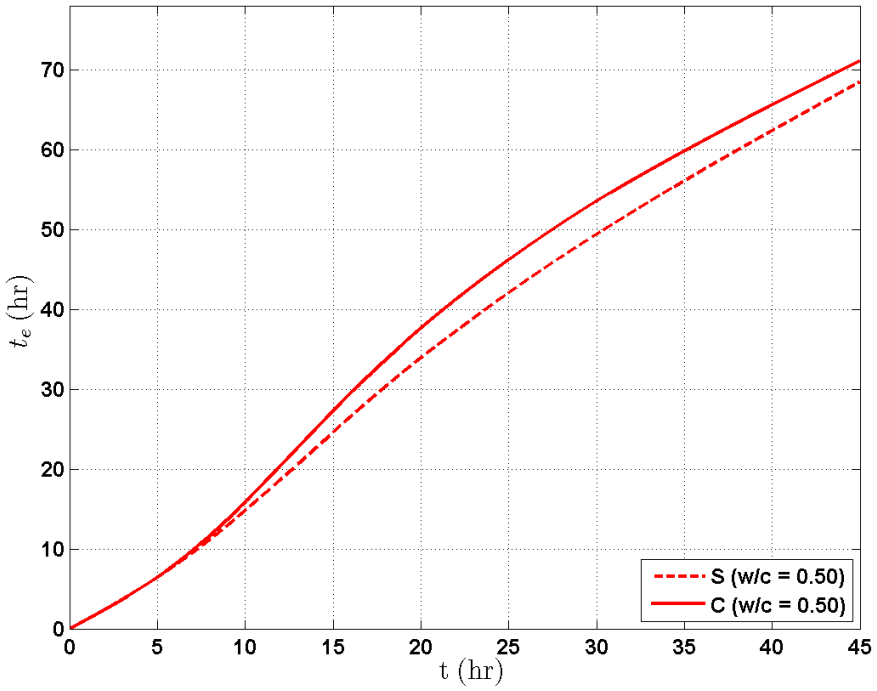

Figure 6-45: Time equivalent vs. real time of 3"×6" concrete cylinder based on surface and core temperature (w/c = 0.50) - E_a = 33,500 J/mol

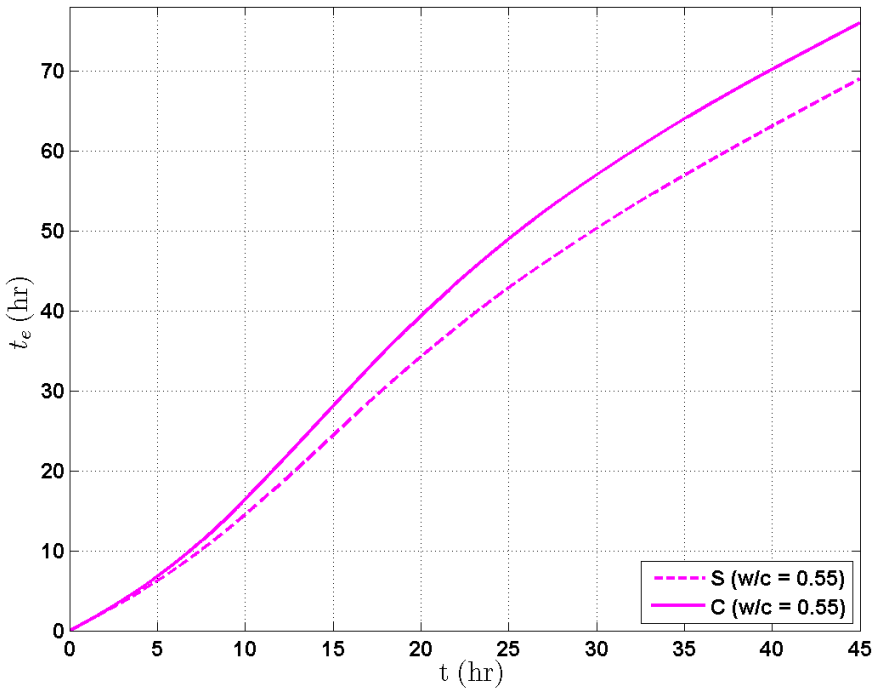

Figure 6-46: Time equivalent vs. real time of 3"×6" concrete cylinder based on surface and core temperature (w/c = 0.55) - E_a = 33,500 J/mol

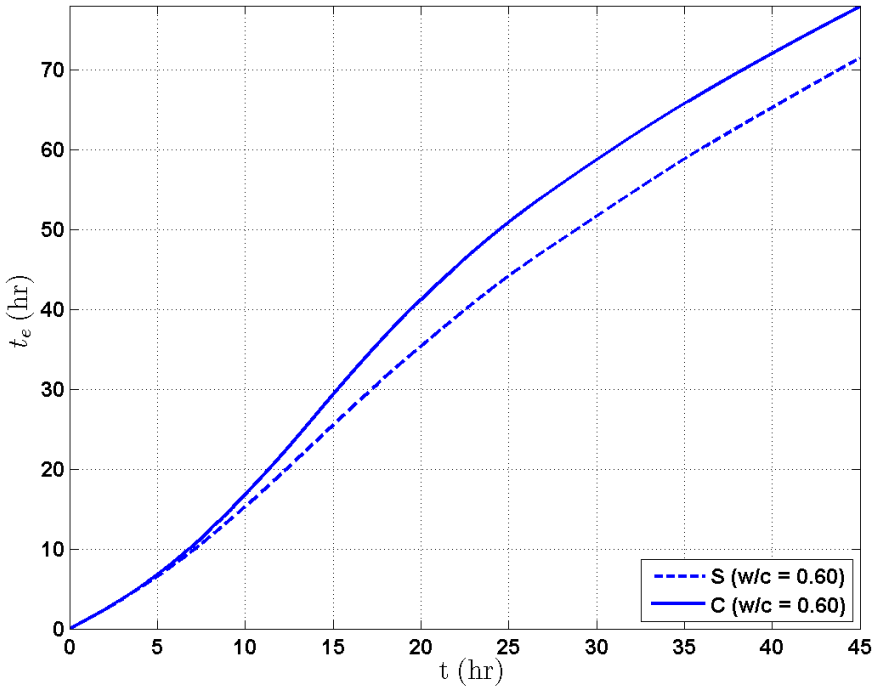

Figure 6-47: Time equivalent vs. real time of 3"×6" concrete cylinder based on surface and core temperature (w/c = 0.60) - E_a = 33,500 J/mol

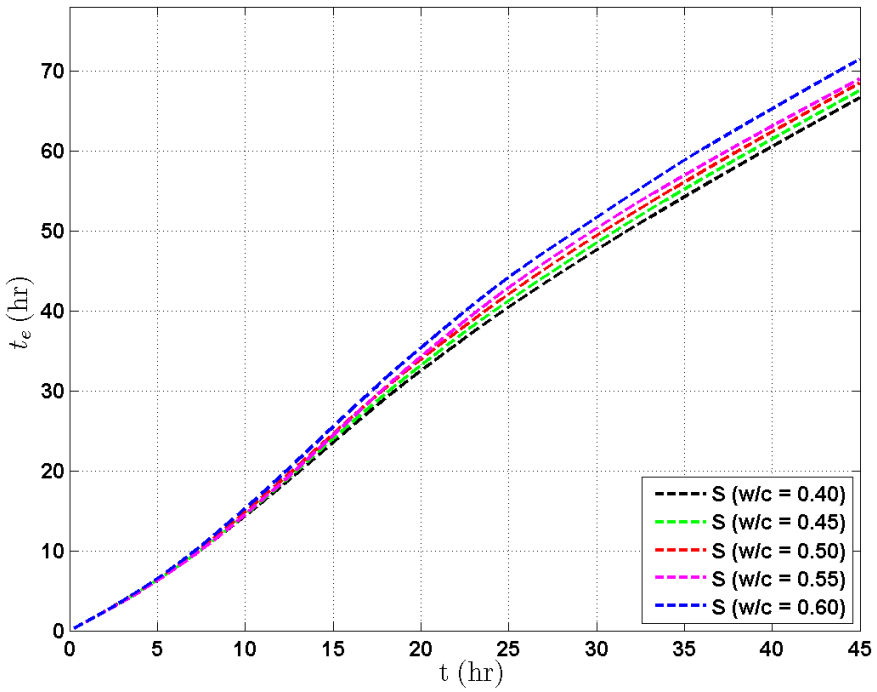

Figure 6-48: Time equivalent vs. real time of 3"×6" concrete cylinders based on surface temperature (w/c = 0.40 - 0.60) - E_a = 33,500 J/mol

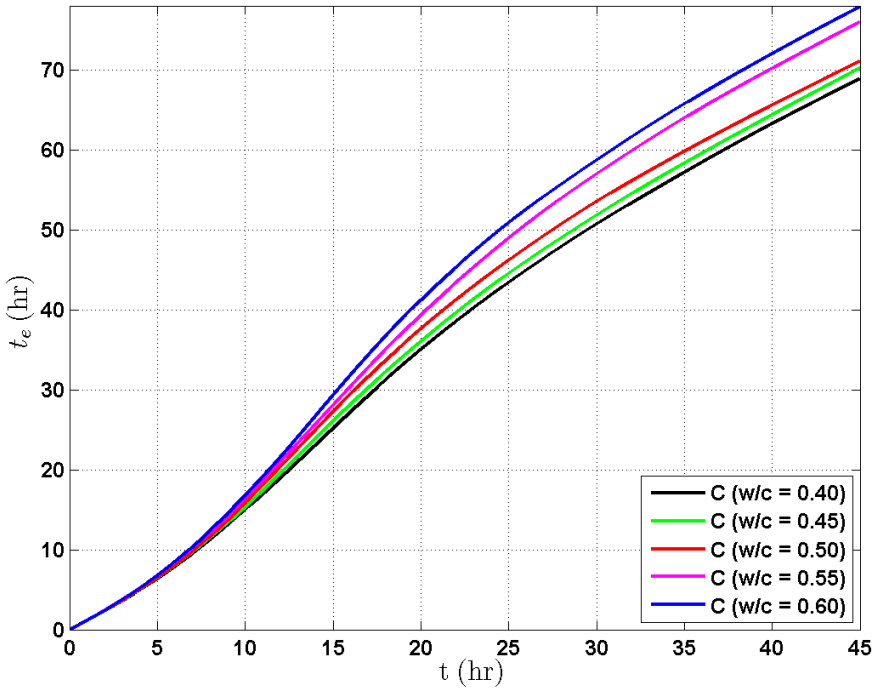

Figure 6-49: Time equivalent vs. real time of 3”×6” concrete cylinders based on core temperature (w/c = 0.40 - 0.60) - E_a = 33,500 J/mol

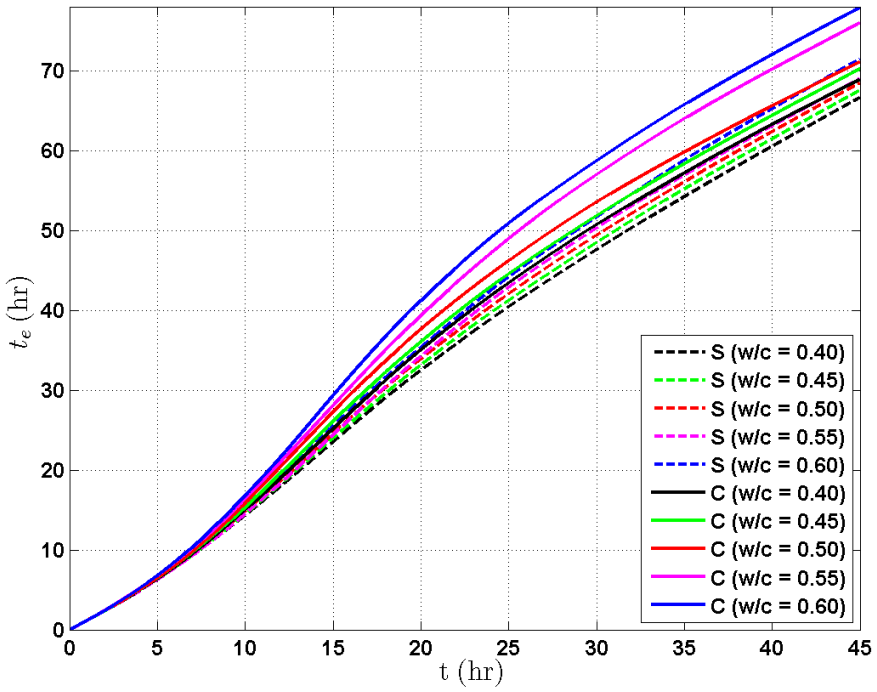

Figure 6-50: Time equivalent vs. real time of 3”×6” concrete cylinders based on surface and core temperature (w/c = 0.40 - 0.60) - E_a = 33,500 J/mol

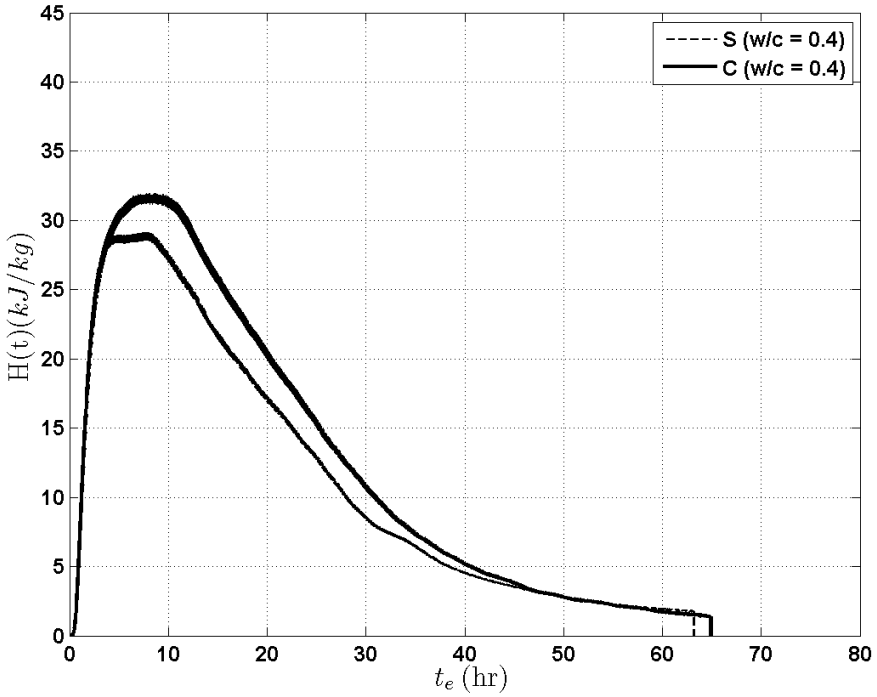

Figure 6-51: Heat of hydration of 3"×6" concrete cylinder at surface and core temperature (w/c = 0.40) - E_a = 29,000 J/mol

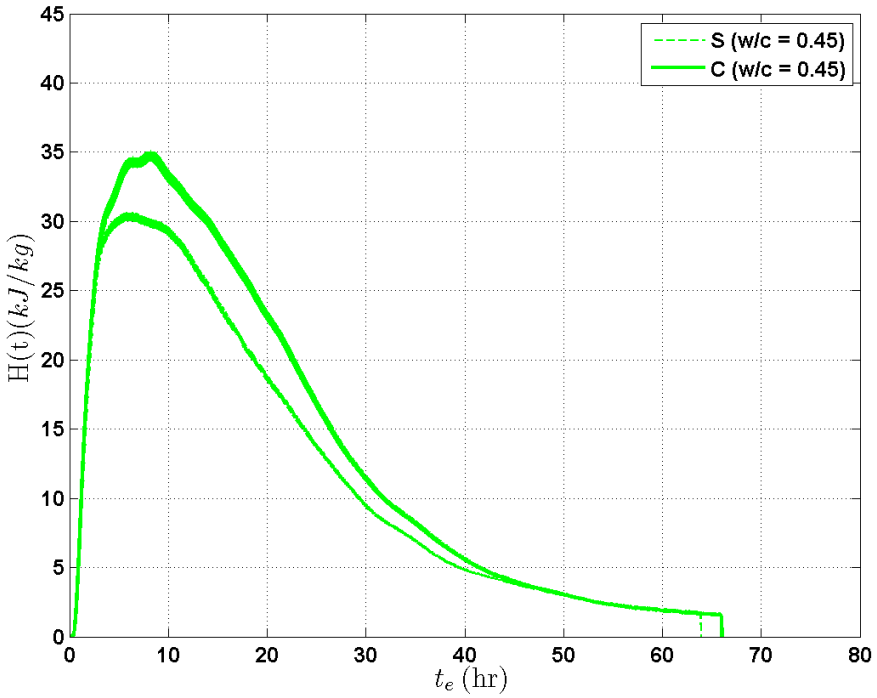

Figure 6-52: Heat of hydration of 3"×6" concrete cylinder at surface and core temperature (w/c = 0.45) - E_a = 29,000 J/mol

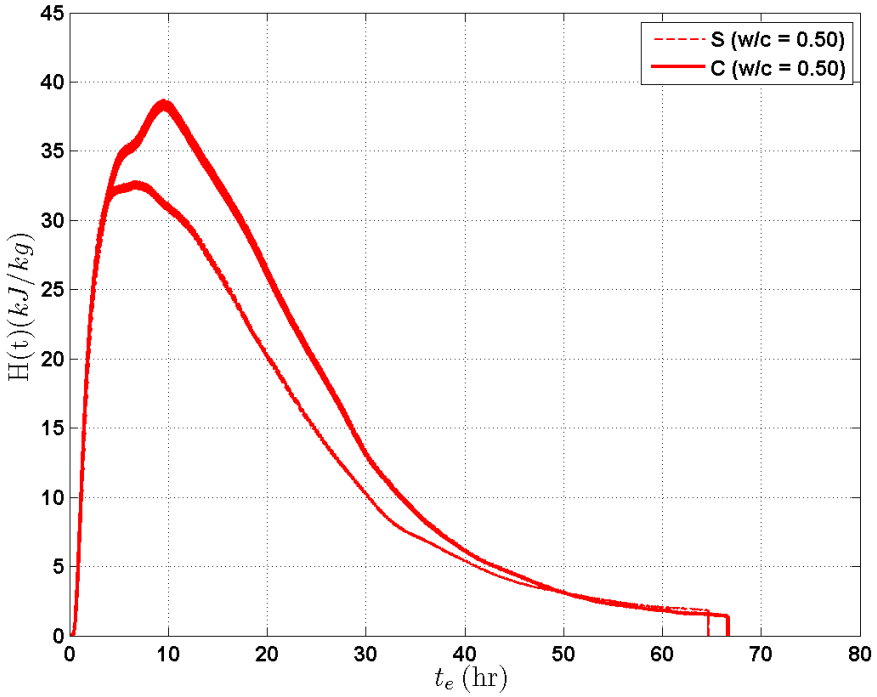

Figure 6-53: Heat of hydration of 3"×6" concrete cylinder at surface and core temperature (w/c = 0.50) - E_a = 29,000 J/mol

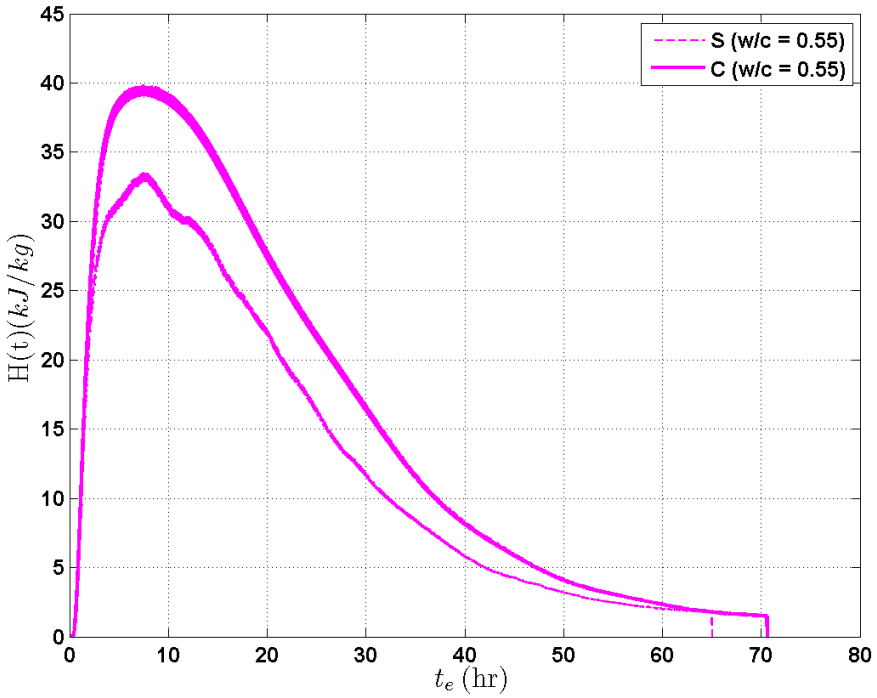

Figure 6-54: Heat of hydration of 3"×6" concrete cylinder at surface and core temperature (w/c = 0.55) - E_a = 29,000 J/mol

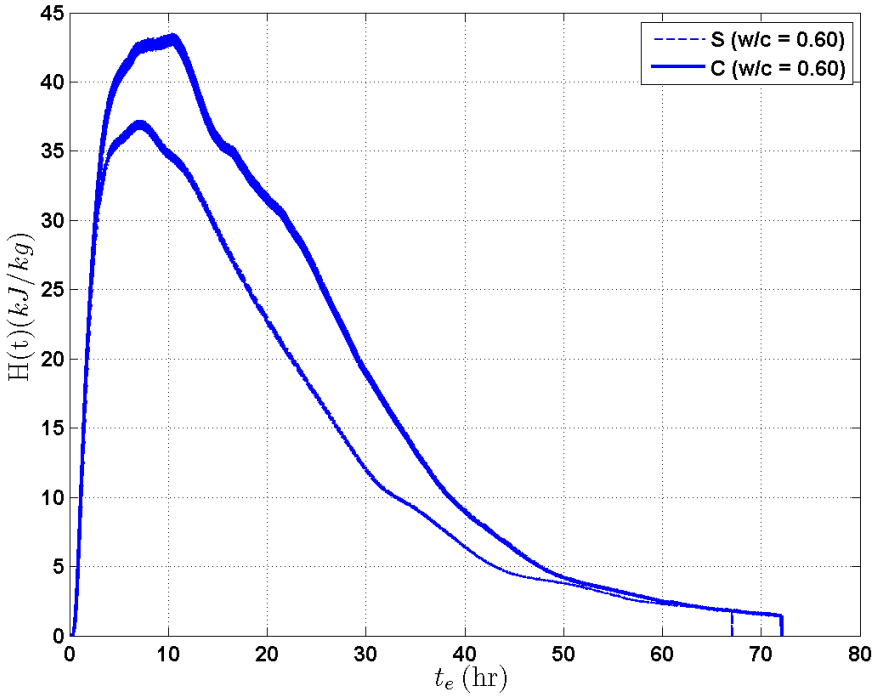

Figure 6-55: Heat of hydration of 3"×6" concrete cylinder at surface and core temperature (w/c = 0.60) - E_a = 29,000 J/mol

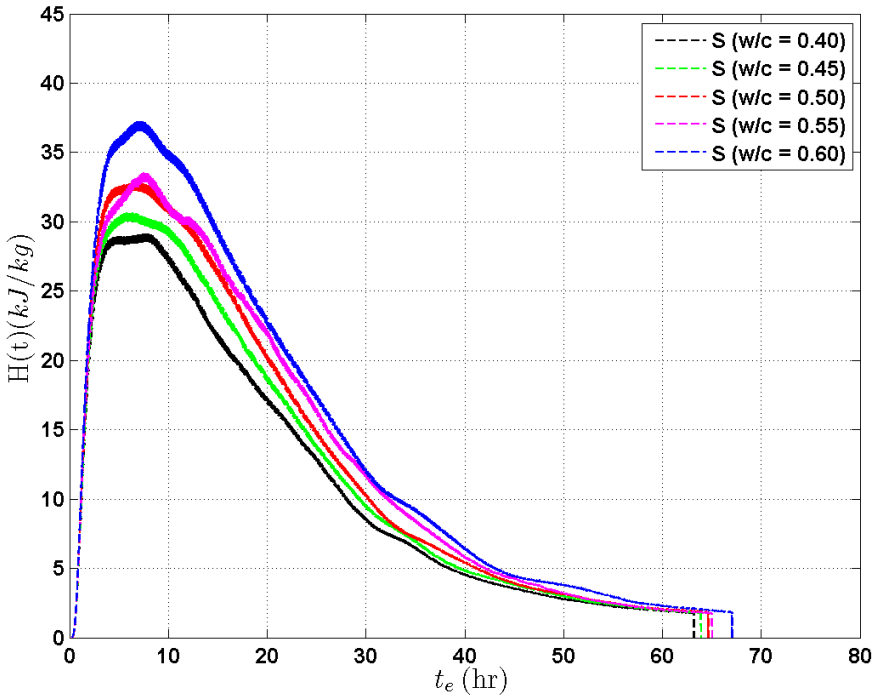

Figure 6-56: Heat of hydration of 3"×6" concrete cylinders at surface (w/c = 0.40 - 0.60) - E_a = 29,000 J/mol

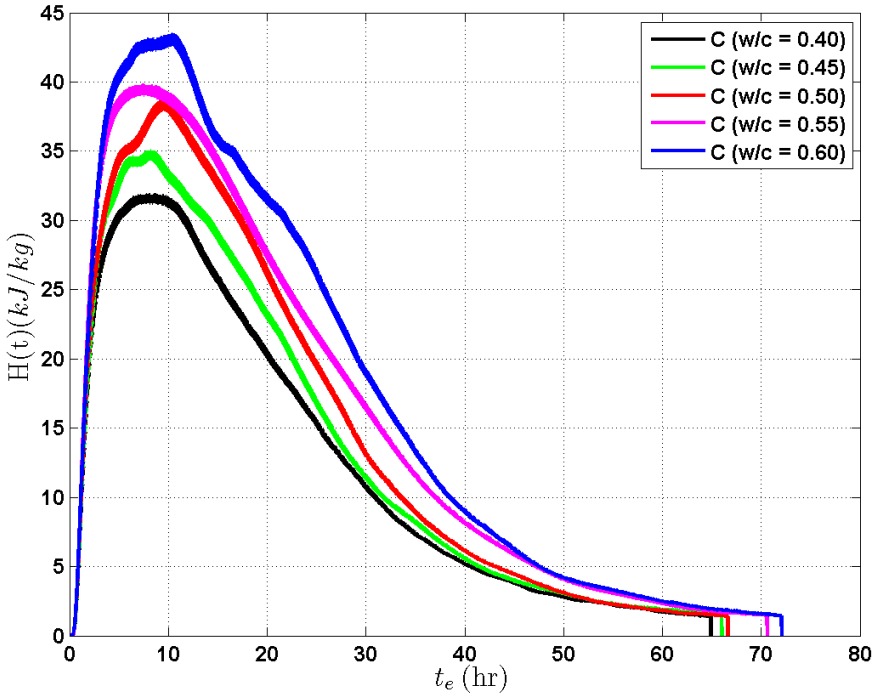

Figure 6-57: Heat of hydration of 3"×6" concrete cylinders at core (w/c = 0.40 - 0.60)- E_a = 29,000 J/mol

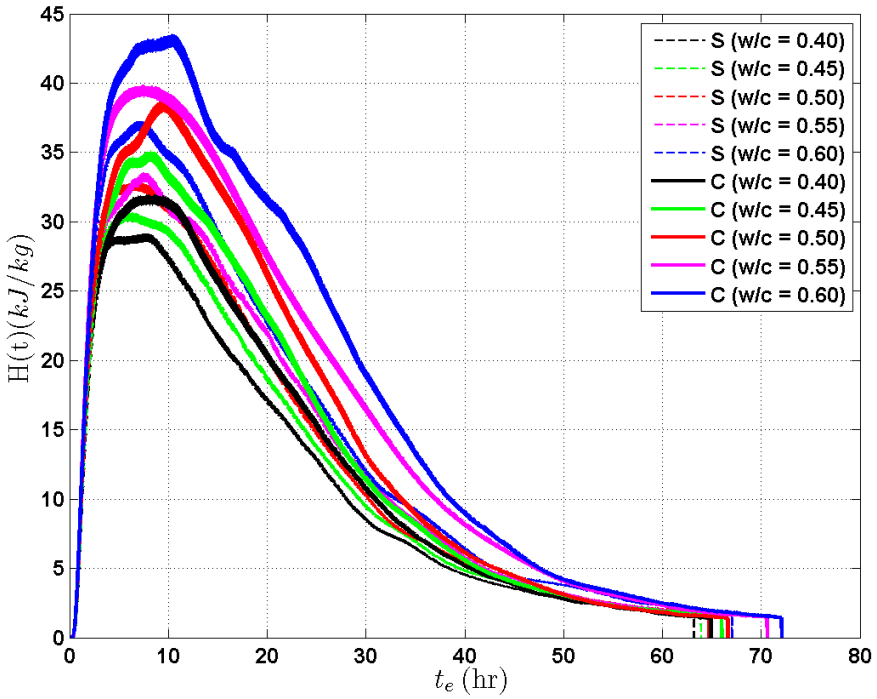

Figure 6-58: Heat of hydration of 3"×6" concrete cylinder at surface (w/c = 0.40 - 0.60)- E_a = 29,000 J/mol

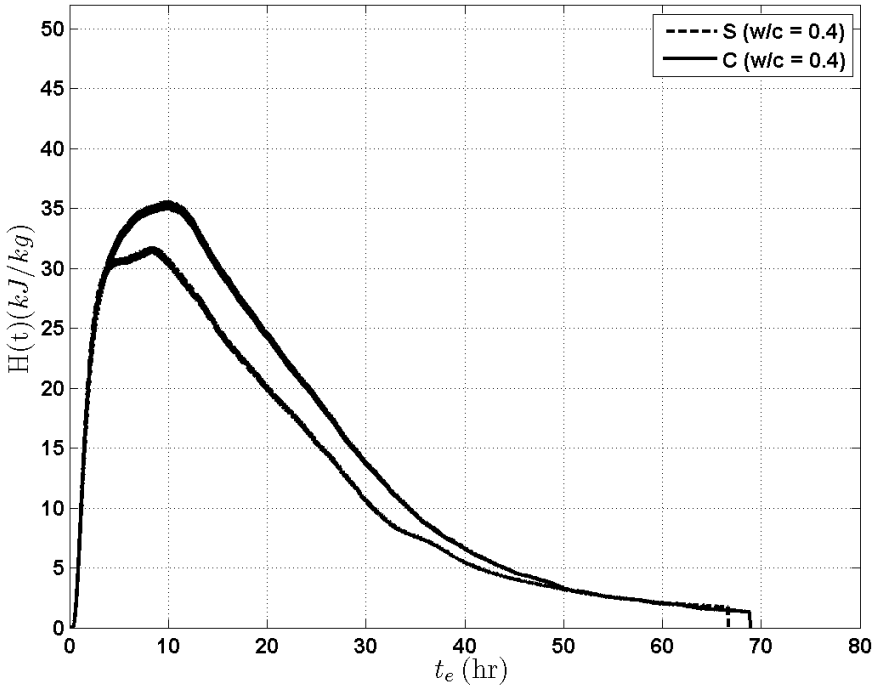

Figure 6-59: Heat of hydration of 3"×6" concrete cylinder at surface and core temperature (w/c = 0.40) - E_a = 33,500 J/mol

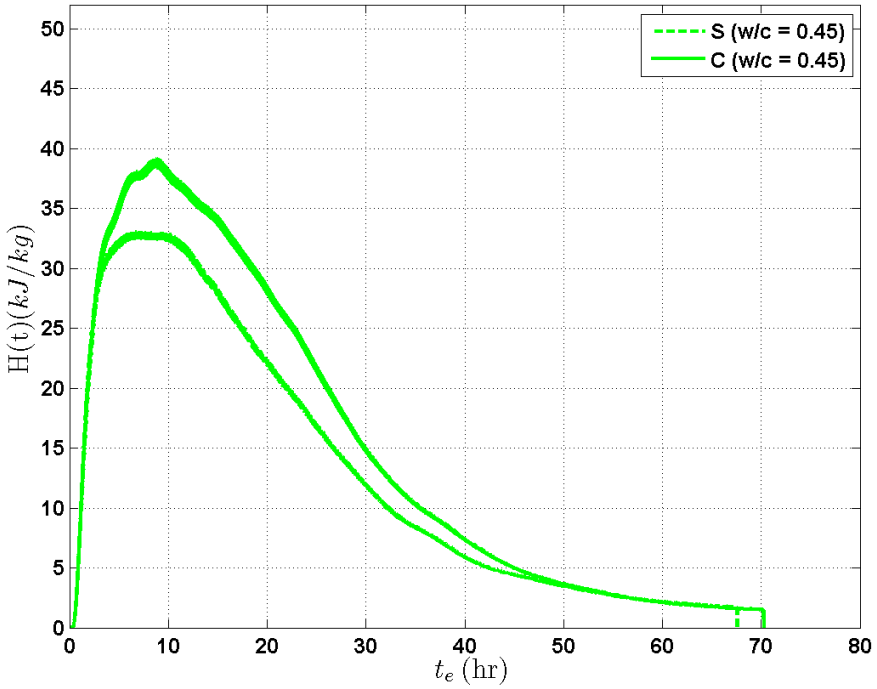

Figure 6-60: Heat of hydration of 3"×6" concrete cylinder at surface and core temperature (w/c = 0.45) - E_a = 33,500 J/mol

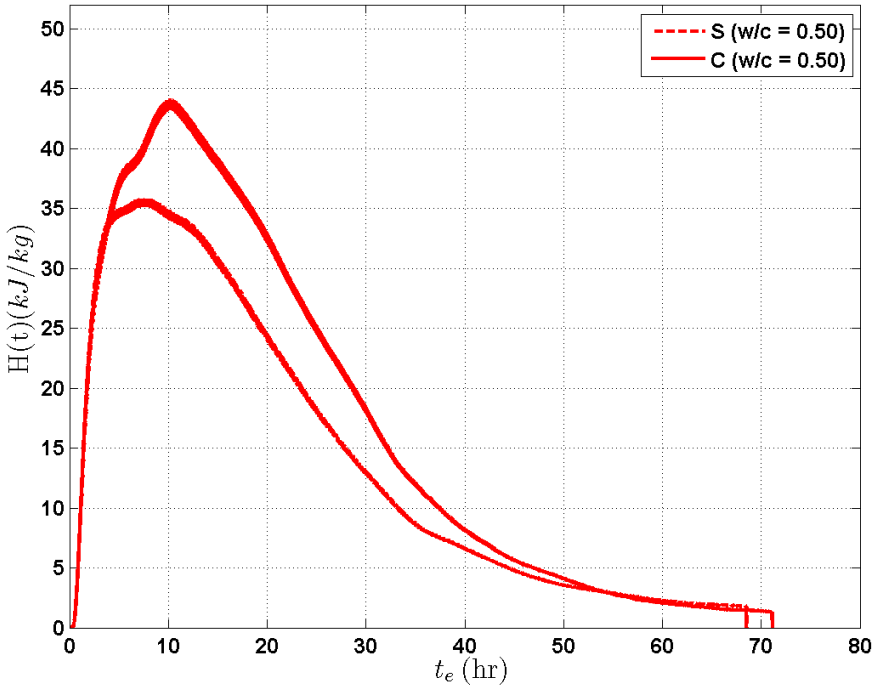

Figure 6-61: Heat of hydration of 3"×6" concrete cylinder at surface and core temperature (w/c = 0.50) - E_a = 33,500 J/mol

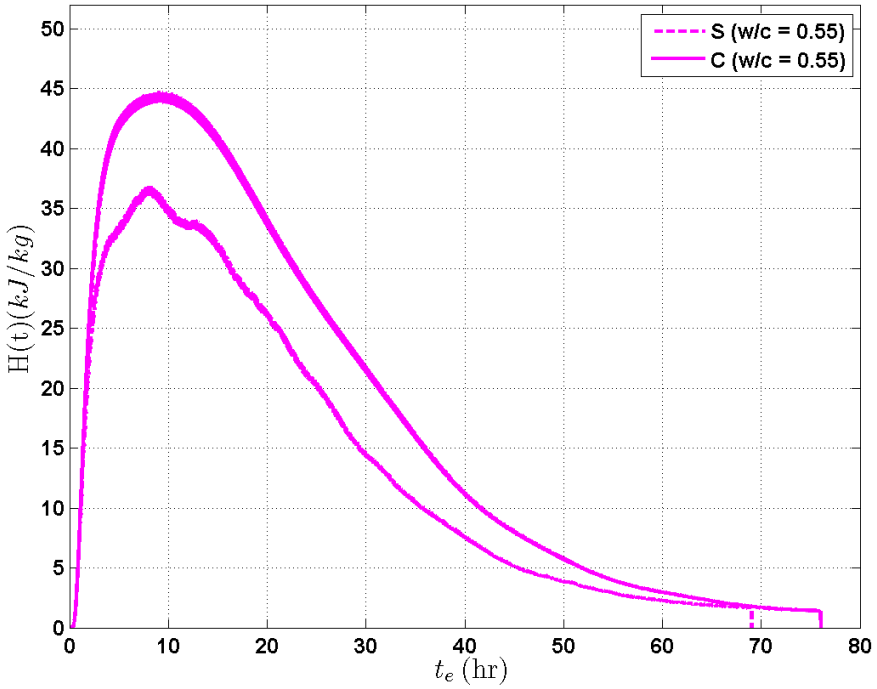

Figure 6-62: Heat of hydration of 3"×6" concrete cylinder at surface and core temperature (w/c = 0.55) - E_a = 33,500 J/mol

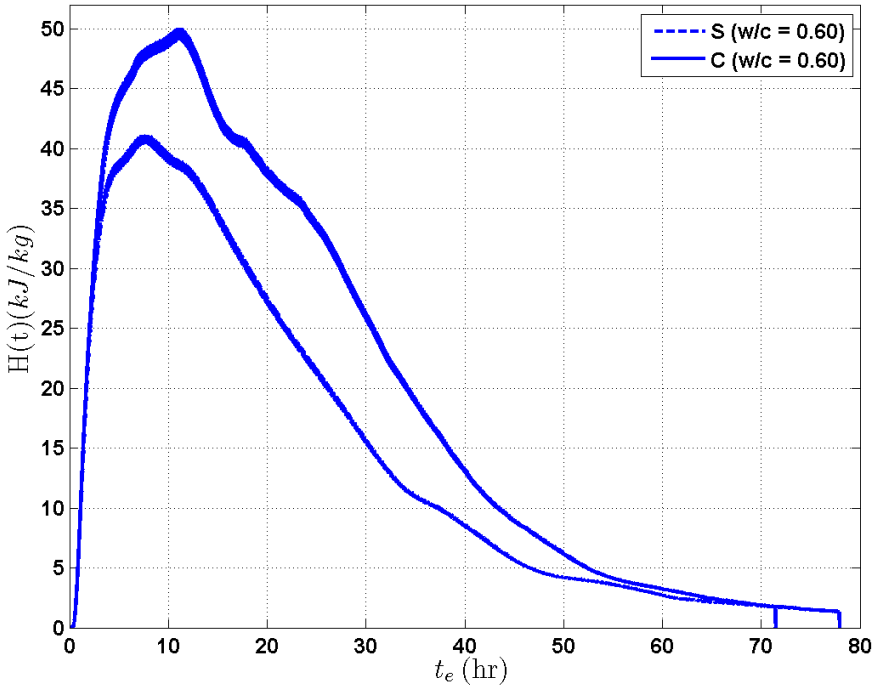

Figure 6-63: Heat of hydration of 3"×6" concrete cylinder at surface and core temperature (w/c = 0.60) - E_a = 33,500 J/mol

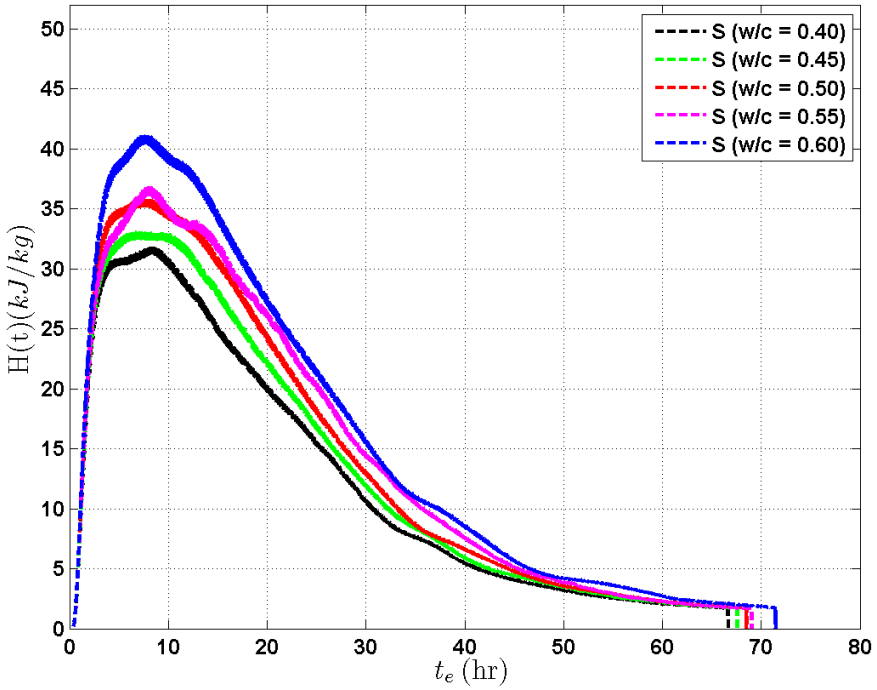

Figure 6-64: Heat of hydration of 3"×6" concrete cylinders at surface (w/c = 0.40 - 0.60) - E_a = 33,500 J/mol

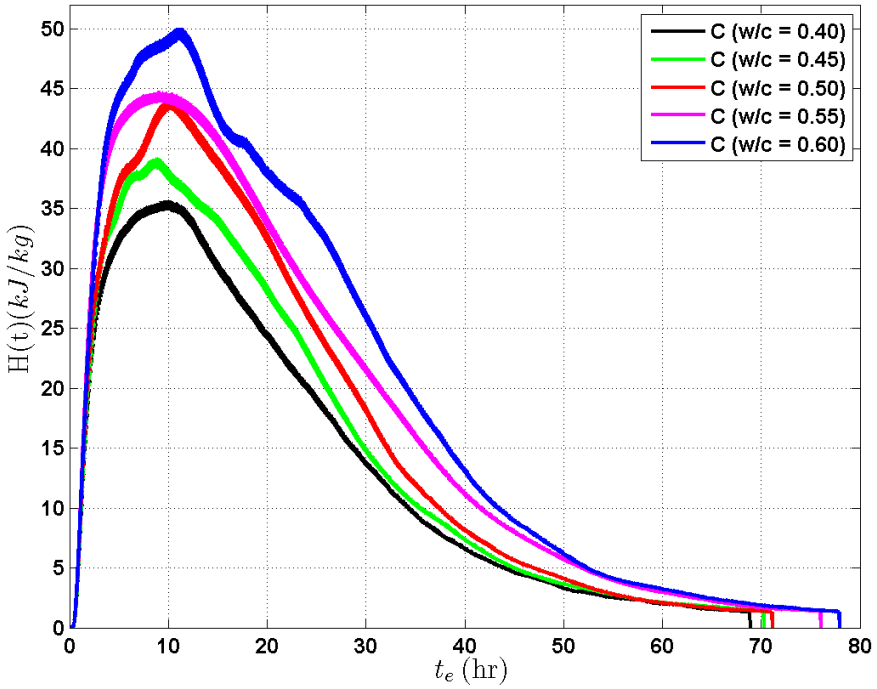

Figure 6-65: Heat of hydration of 3"×6" concrete cylinders at core (w/c = 0.40 - 0.60) - E_a = 33,500 J/mol

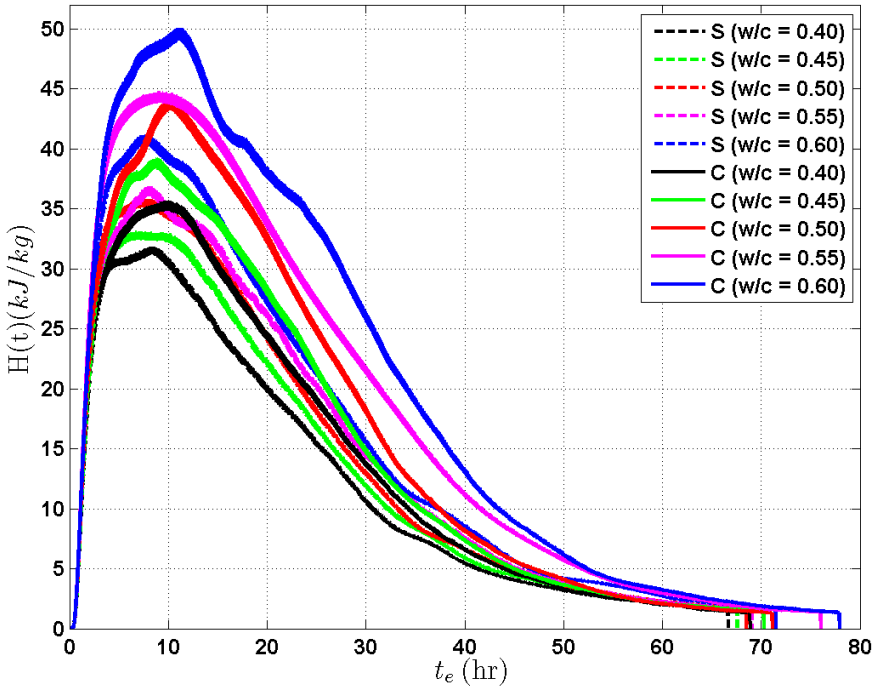

Figure 6-66: Heat of hydration of 3"×6" concrete cylinder at surface (w/c = 0.40 - 0.60) - E_a = 33,500 J/mol

Chapter 7

Conclusion

In this thesis research, concrete temperature development at its early age is studied. Two experimental setups were implemented. In the first setup, concrete specimens were insulated by a styrofoam chamber, placed in an open environment and one FP fiber optic sensor and one thermocouple sensor were embedded into the core of concrete cylinders to measure the temperature changes. In the second setup, concrete specimens were insulated by a styrofoam chamber, placed in a temperature-controlled glass chamber. Two FP fiber optic sensors were embedded in concrete cylinders to measure the temperature distribution within concrete. In all experimental measurements, Optical Sensing Analyzer si720 was used to transmit light source into FP fiber optic sensors and to receive signals from FP fiber optic sensors. In addition, all FP fiber optic sensors consist of the same structure and material property.

Three 4”×8” and five 3”×6” concrete cylinders were manufactured for the temperature measurement in the first and the second experimental setups, respectively. Each experiment was conducted based on the first and the second setup last 70 hours and 45

hours, respectively. In all experiments, the amount of cement, sand and gravel were kept constant while only water to cement ratio varied , specifically from 0.4 to 0.6.

Concrete Temperature

1. In both experimental sets, the maximum temperature increased with the increase of the water-to-cement ratio.

2. In experimental set No.1, temperature development within concrete cylinders primarily increased due to heat of hydration and decreased due to ambient conditions during the cooling period.

3. In experimental set No. 2, the surface and core temperature generated a very similar profile. These temperature curves intersected during the cooling period because the temperature distribution within concrete structure is reaching thermal equilibrium. The profile of surface temperature varied according to ambient condition during the deceleration period. However, the core temperature decreased lower than the ambient temperature, which is not completely understood.

With the temperature results collected from experimental measurements, apparent activation energy and heat of hydration are studied. Two approaches were used: (a) the first approach is based on real-time measurements, and (b) the second approach is based on concrete equivalent age. Both approaches are in good agreement and considered to be reliable for the prediction of concrete hydration heat at its early age.

FP Sensors and Thermocouple Sensor

FP sensors provided accurate temperature measurements in all experiments given that proper protection can be provided. However, thermocouple sensor appeared to be easily

interfered by ambient conditions. Type of FP fiber optic sensor used in this research is considered to be an outstanding candidate in measuring temperature in concrete structures.

Future Work

This research study is still in its preliminary stage. More work is needed in order to obtain more experimental results to better understand the concrete hydration behavior. It is recommended to:

- repeat more tests for both setups for three standard sizes of concrete cylinder, 3”×6”, 4”×8” and 6”×12”.
- perform the second setup at various ambient temperatures, 20 ^oC, 25 ^oC, 30 ^oC, and 40 ^oC to see the difference of temperature distribution for concrete specimens made of the same size and/or different sizes.

Appendix A

Mix Design Calculation

Assumptions: (a) water absorption for 3/8” gravel is 0.5%, (b) water absorption for sand is 1%.

W_{cement} = 3.15 x 1 x 62.4 = 196.56 lb

W_{water} = 0.5 x 196.56 = 98.28 lb

V_{water} = 1/62.4 = 1.575 ft^3

SSD_{cement} = 196.56/7.58 = 25.95 lb/ft^3

SSD_{sand} = 336.96/7.58 = 44.48 lb/ft^3

SSD_{gravel} = 486.72/7.58 = 64.25 lb/ft^3

SSD_{water} = 98.28/7.58 = 12.97 lb/ft^3

Water absorbed by:

Sand = 1% x 44.48 = 0.445 lb/ft^3

Gravel = 0.5% x 64.25 = 0.321 lb/ft^3

Total = 0.766 lb/ft^3

Adjusted weight of:

cement = 25.95 lb/ft^3

sand = 44.48 - 0.445 = 44.04 lb/ft^3

gravel = 64.25 - 0.321 = 63.93 lb/ft^3

water = 12.97 + 0.766 = 13.74 lb/ft^3

Cement factor = 7.45 sacks/cy

A summary of calculated result for the mixture with w/c equals 0.5 (4”x8” cylinder) can be found in Table A.1.

Table A.1: Trial mix calculation for mixture with w/c = 0.5

Material	G	Volume (ft^3)	W (lb)	SSD (lb/ft^3)	Adjusted Wt. (lb/ft^3)	$Mass_{dry}$ (lb)
Cement	3.15	1	196.56	25.95	25.95	1.510
Sand	2.7	2	336.96	44.48	44.04	2.562
Gravel	2.6	3	486.72	64.25	63.93	3.719
Water	1	1.575	98.28	12.97	13.74	0.799
Total		7.58			147.66	8.590

Bibliography

[1] D. P. Bentz and C. J. Haecker. An argument for using coarse cements in high performance concrete. *Cement and Concrete Research*, 29(2):615–618, 1999.

[2] CCAA. Hot-weather concreting. *Cement Concrete & Aggregates Australia*, 11, 2004.

[3] C. Chang. Fiber-optic smart structures for monitoring and managing the health of transportation infrastructures. *METRANS Transportation Center Project 09-13*, 4, 2010.

[4] P. Eklund and S. Rydblom. Fiber optic sensors. Technical report.

[5] P. C. Graham, Y. Ballim, and J. B. Kazirukanyo. Effectiveness of the finess of two south african portland cements for controlling early-age temperature development in concrete. *ACI Materials Journal*, 53(1):39–45, 4, 2011.

[6] D. S. Guo, E. Y. Chen, G. L. Low, and J. L. Yang. Experimental modeling of temperature rise of mass concrete by fdm method. *26th Conference on our world in concrete and structures*, 8, 2001.

[7] D. Inaudi. Application of civil structural monitoring if europe using fiber optic sensors. *Prog. Structural Engineering Material*, 2:351–358, 2000.

[8] D. Inaudi, R. Deblois, A. Phipps, and K. Western. Structural health monitoring system for the new i-35 st anthony falls bridge. *International Conference on SHM on Intelligent Infrastructure*, 7, 2009.

[9] D. Indaudi and A. D. Grosso. Fiber optic sensors for structural control. *The 14th World Conference on Earthquake Engineering*, 10, 2008.

[10] k van Breugel. *Prevention of Thermal Cracking in Concrete at Early Ages.*, pages 51–70. E & FN Spon, 11 New Fetter Lane, London EC4P 4 EE, UK, 1998.

[11] A. Klini, T. David, E. Bourillot, S. Emonin, P. Papadopoulos, J. Goudonnet, and G. Kotrotsios. Reproducible optical fiber tips for photon scanning tunneling microscopy with very small (< 5) cone angle. *J. Lightwave Technol*, 16:1220, 1998.

[12] K. G. Kuder, R. Gupta, K. Lowrie, D. Sommer, and N. Wheeler. Practical test method and use of novel temperature development index for evaluating concrete development. *Society for Experimental Mechanics*, 2010.

[13] W. Ma, D. Sample, R. Martin, and P. W. Brown. Calorimetric study of cement blends containing fly ash, silica fume, and slag at elevated temperatures. *ACI Materials Journal*, 16(2):93–99, 1994.

[14] S. Masri, M. Agbabian, A. Abdel-Ghaffar, M. Highazy, R. O. Claus, and M. J. de Vries. Experimental study of embedded fiber-optic strain gauges in concrete structures. *Journal of Engineering Mechanics*, 120(8), 8, 1994.

[15] S. Mindess, J. F. Young, and D. Darwin. *Concrete*. Pearson Education, Inc., Upper Saddle River, NJ, 2nd edition, 2003.

[16] M. Nilsson. Thermal cracking of young concrete. partial coefficient, restraint effects and influence of casting joints. Master's thesis, LuleaUniversity of Technology, 1, 2000.

[17] NRMCA. Concrete in practice. Technical report, National Ready Mixed Concrete Association, 2009.

[18] J. Ou and Z. Zhou. Applications of optical fiber sensors of shm in infrastructures. *Smart Sensor Phenomena, Technology, Networks and Systems*, 6933:10, 3, 2008.

[19] PCA. Portland cement, concrete, and heat of hydration. *Portland Cement Association*, 18(2), 1997.

[20] J. L. Poole, K. A. Riding, K. J. Folliard, M. C. G. Juenger, and A. K. Schindler. Methods for calculating activation energy for portland cement. *ACI Materials Journal*, 104(1):303–311, 1-2, 2007.

[21] Y. J. Rao, P. J. Henderson, D. A. Jackson, L. Zhang, and I. Bennion. Simultaneous strain, temperature and vibration measurement using a multiplexed in-fibre-bragg-grating/fibre-fabry-perot sensor system. *Institution of Engineering and Technology*, 33:2063 – 2064, 11, 1997.

[22] K. Ravisankar. Monitoring the health of large structures. *Structural Engineering Research Center, CSIR Campus, Taramani, Chennai*, 2002.

[23] K. A. Riding, J. L. Poole, A. K. Schindler, M. C. G. Juenger, and K. J. Folliard. Evalulation of temperature prediction methods for mass concrete members. *ACI Materials Journal*, 103(5):357–365, 9-10, 2006.

[24] K. A. Riding, J. L. Poole, A. K. Schindler, Maria, C. G. Juenger, and K. J. Folliard. Temperature boundary condition models for concrete bridge members. *ACI Materials Journal*, 104(4):379–387, 7-8, 2007.

[25] A. K. Schindler. Prediction of concrete setting. Technical report, Department of Civil Engineering, Auburn University, Alabama, USA, 2003.

[26] A. K. Schindler. Effect of temperature on hydration of cementitious materials. *ACI Materials Journal*, 101(1):72–81, 1-2, 2004.

[27] A. K. Schindler and K. J. Folliard. Heat of hydration models for cementitious materials. *ACI Materials Journal*, 102(1):24–33, 1-2, 2005.

[28] A. K. Schindler and K. J. Folliard. Heat of hydration models for cementitious materials. *ACI Materials Journal*, 102(1), 1-2, 2005.

[29] A. K. Schindler and B. F. McCullough. The importance of concrete temperature control during concrete pavement construction in hot weather conditions. *Annual meeting of the transportation research board*, 1, 2002.

[30] W. technology and services (WTEC). Optical sensor technologies. 2, 1996.

[31] Y. Tian, W. Wang, N. Wu, X. Zou, C. Guthy, and X. Wang. A miniature fiber optic refractive index sensor built in a mems-based microchannel. *Sensors*, 11:1078–1087, 2011.

[32] S. C. Tjin, Y. Wang, X. Sun, P. Moyo, and J. M. W. Brownjohn. Application of quasi-distributed fibre bragg grating sensors in reinforced concrete structures. *Institute of Physics Publishing*, 13:583589, 3, 2002.

[33] K. van Breguel. *Simulation of hydration and formation of structure in hardening cement-based materials*. PhD thesis, Delft University of Tecnology, The Netherlands, 1997.

[34] X. Y. Wang, H. K. Cho, and H. S. Lee. Prediction of temperature distribution in concrete incorporating fly ash or slag using a hydration model. *Composites*, Part B(42):27–40, 2010.

[35] Y. Wang, S. C. Tjin, X. Sun, Y. L. Tan, and S. C. Fan. Measurement of temperature profile of concrete structures using embedded fbgs and thermocouples. *International Society of Optical Engineering*, 4235:288–297, 2001.

[36] T. Wei, Y. Han, Y. Li, H.-L. Tsai, and H. Xiao. Temperature-insensitive miniaturized fiber inline fabry-perot interferometer for highly sensitive refractive index measurement. *Opt. Express*, 16:5764–5769, 2008.

[37] Y. wei Yun, I. Y. Jang, S. K. Kim, and S. M. Park. Early-age autogenous shrinkage of hcp columns by embedded fbg sensor. *Key Engineering Materials*, 419:1–4, 2010.

[38] Z. Wu, B. Xu, K. Hayashi, and A. Machida. Distributed optic fiber sensing for a full-scale pc girder strengthened with prestressed pbo sheets. *Engineering Structures*, 28(7):1049–1059, 2006.

[39] X. Xiong and K. van Breugel. Isothermal calorimetry study of blended cements and its application in numerical simulations. *Heron*, 46(3):151–159, 2001.

[40] Q. Xu, J. M. Ruiz, J. Hu, K. Wang, and R. O. Rasmussen. Modeling hydration properties and temperature developments of early-age concrete pavement using calorimetry tests. *Thermochimica Acta*, 512:76–85, 2011.

[41] X. Zeng, X. Bao, and C. Y. C. et al. Strain measurement in a concrete beam by use of the brillouin-scattering-based distributed fiber sensor with single-mode fibers embedded in glass fiber reinforced polymer rods and bonded to steel reinforcing bars. *Applied Optics*, 41(24):5105–5114, 2002.

[42] Y. Zhang, X. Chen, Y. Wang, K. Cooper, and A. Wang. Microgap multicavity fabry perot biosensor. *Lightwave Technology*, 25:1797–1804, 2007.